Development of native and contrast enhanced magnetic resonance imaging for the characterization of cardiovascular disease

Peel, Sarah

Awarding institution:
King's College London

Title: Development of native and contrast enhanced magnetic resonance imaging for the characterization of cardiovascular disease

Author: Sarah Peel

Development of native and contrast enhanced magnetic resonance imaging for the characterization of cardiovascular disease

Sarah Anne Peel

A dissertation submitted for the degree

of

Doctor of Philosophy

of the

University of London

Division of Imaging Sciences and Biomedical Engineering

School of Medicine, King's College London

Abstract

Late gadolinium enhancement (LGE) imaging is a widely used cardiovascular MRI technique. My work focused on developing new LGE MRI sequences to; identify plaque in the aortic vessel wall, to visualize areas of ventricular scar after myocardial infarction and pulmonary vein and atrial wall lesions after radiofrequency (RF) ablation for atrial fibrillation (AF).

The double inversion recovery (DIR) sequence is traditionally used for vessel wall imaging. It however requires a Look Locker scan to choose the correct inversion time (TI) to achieve post-contrast blood suppression. The quadruple inversion recovery (QIR) sequence was later developed to suppress blood before and after contrast using identical imaging parameters. ECG-triggering was not required for the carotid arteries as there is adequate blood flow during the entire cardiac cycle to achieve sufficient blood exchange for blood suppression. I designed a new ECG-triggered QIR implementation for vessel wall imaging of the aorta which has variable flow during the cardiac cycle. I found it improved blood suppression, vessel wall sharpness and image quality scores compared to the un-triggered QIR implementation.

The inversion recovery (IR) technique is the gold standard for imaging ventricular and atrial wall scar. It also requires a Look Locker scan to define the TI that suppresses normal myocardium in order to detect regions of scar. However, there is also often high IR blood signal that can hamper the detection of small sub-endocardial infarcts and scar size and transmurality measurements. I developed a novel dual-IR sequence that achieves suppression of normal myocardium and also reduces the blood signal. I found this improved blood suppression and inter-observer variability of scar size measurement and allowed imaging at an earlier time point compared to IR imaging for both ventricular and atrial wall scar. For ventricular scar, I also found improved expert confidence and inter-observer variability for transmurality assessment.

Table of Contents

List of Figures

List of Tables

List of Abbreviations

AAA	Abdominal Aortic Aneurysm
AF	Atrial Fibrillation
AFL	Atrial Flutter
ANOVA	Analysis of Variance
CNR	Contrast-to-Noise Ratio
DIR	Double Inversion Recovery
DSG	Diffusion Sensitizing Gradients
ECG	Electrocardiogram
EP	Electrophysiological
FOV	Field of View
FWHM	Full Width Half Maximum
Gd	Gadolinium
GE	Gradient echo
IR	Inversion Recovery
LGE	Late Gadolinium Enhancement
MOLLI	Modified Look Locker Inversion Recovery
MRA	Magnetic Resonance angiography
MRI	Magnetic Resonance Imaging
M_z	Longitudinal magnetization
M_zb	Longitudinal magnetization of blood
M_zt	Longitudinal magnetization of tissue
NSA	Number of Samples Acquired
NSF	Nephrogenic Systemic Fibrosis
PC - MRI	Phase contrast MRI
PSIR	Phase Sensitive Inversion Recovery
PV	Pulmonary Vein
QIR	Quadruple Inversion Recovery
RF	Radio Frequency
ROI	Region of interest
R_1	longitudinal relaxation rate

R_2	transverse relaxation rate
SE	Spin Echo sequence
SENSE	Sensitivity Encoding
SNR	Signal-to-Noise Ratio
SR	Saturation Recovery
SSFP	Steady State Free Precession
TE	Echo time
TFE	Fast gradient echo sequence
TI	Inversion time delay
TR	Repetition Time
TR_{eff}	Effective Repetition Time
TSE	Turbo Spin Echo
TFE	Turbo Field Echo
T1	longitudinal relaxation time
T2	transverse relaxation times

Chapter 1

1. Introduction

1.1 *Cardiovascular Disease*

Cardiovascular disease is the leading cause of morbidity and mortality in the Western world [1]. The aim of this research was to design, implement, optimize and test novel magnetic resonance imaging (MRI) pulse sequences to characterize several aspects of cardiovascular disease including:

- Abdominal aortic plaques
- Chronic myocardial scar
- Atrial scar after radiofrequency (RF) ablation for atrial fibrillation (AF)

1.2 *Atherosclerotic Plaques*

Atherosclerosis, the build up of fatty plaques in the walls of an artery, is the most common cause of cardiovascular disease. If we consider the progression of an atherosclerotic plaque, it is clear that it is not a disease of the lumen but of the vessel wall itself. The initial response to endothelial injury is vessel enlargement through outward remodeling with relative preservation of the lumen diameter [2]. The stable plaque, which is characterized by a thick fibrous cap and small lipid rich core, often causes more luminal narrowing compared to the unstable plaque, which has a thinner fibrous cap and large lipid rich core (Figure 1.1).

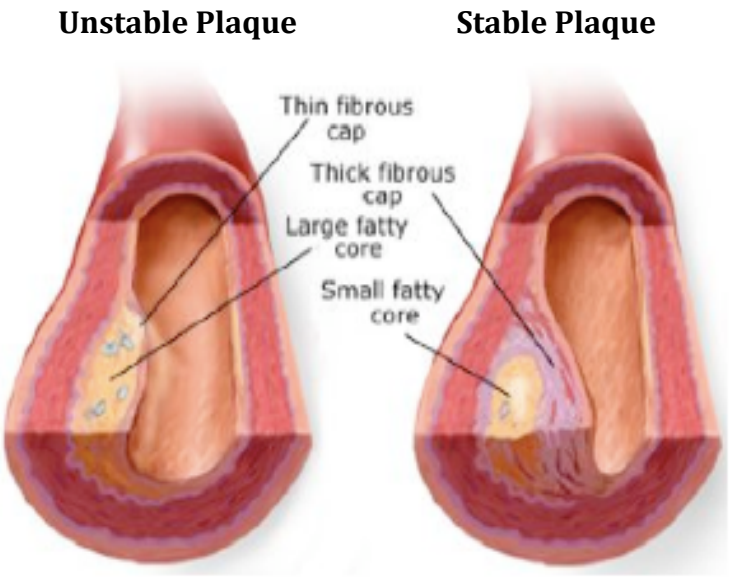

Figure 1-1: Schematic of an unstable and stable coronary plaque [3].

Patients with atherosclerosis are often asymptomatic until plaque rupture. This can lead to the formation of a thrombus, which can subsequently occlude downstream arteries and cause stroke or acute myocardial infarction (AMI). Although it causes less luminal narrowing, an unstable plaque is more vulnerable to rupture due to its thinner fibrous cap. Indeed approximately 60-70 % of acute coronary syndromes are known to be caused by stenosis of less than 50 % luminal diameter [3, 4]. The differentiation of vulnerable from stable plaques is therefore an important area of research. The aim is to determine those at risk who may benefit from medical treatment and/or preventative lifestyle measures.

Autopsy data has demonstrated that the abdominal aorta offers a valuable early window for the study of atherosclerosis [5]. In the development of imaging strategies and novel contrast agents, the aorta is often used as a model due to its large size and simple morphology compared with the coronary arteries. The aorta can be imaged using x-ray angiography or magnetic resonance angiography (MRA) however both techniques can only visualize the vessel lumen and x-ray carries the risk of an invasive procedure. Ultrasound (US) has been used to measure the ratio of intimal to media thickness, however it cannot achieve high spatial resolution at increasing tissue depths and this limits its use

for the aorta [5]. Trans-esophageal echocardiogram (TEE) is a semi-invasive technique which can visualize some plaque characteristics but it has been found to have low sensitivity for atheroma detection [6]. The detection of aortic plaque using computed tomography (CT) has been found to predict vascular events and has been considered as the established imaging technique [7]. However, it employs ionizing radiation and so is perhaps unsuitable for serial monitoring or screening for disease. Positron emission tomography (PET) imaging has also been proposed but also employs ionizing radiation and suffers from limited spatial resolution [8].

MRI has been used to identify plaque components [9-14] and has the advantage of not using ionizing radiation and the availability of different endogenous contrast mechanisms. Gadolinium contrast enhancement in the coronary or aortic vessel wall on MR images has been proposed as an indicator of inflammation or fibrosis [15] and uptake of molecular contrast agents (such as those targeted to elastin or fibrin) may help identify plaque components and measure plaque vulnerability [16, 17].

1.3 *Myocardial Infarction*

If coronary artery disease (CAD) is allowed to progress, coronary artery obstruction may lead to ischemia and eventually infarction of the myocardial tissue supplied by the diseased coronary arteries. Revascularization is an invasive interventional procedure to restore the blood supply to the myocardial tissue. To assess the likelihood of functional recovery after revascularization, it is important to distinguish the areas of viable myocardium from those which have suffered irreversible damage. There are several non-invasive imaging techniques which can assess myocardial viability including positron emission tomography (PET), single-photon-emission computed tomography (SPECT) and dobutamine echocardiography. However, due to their limited spatial resolution, they cannot measure the transmurality of infarction and may not be able to visualize small areas of infarction. The late gadolinium enhancement (LGE) MRI technique has improved spatial resolution compared to these techniques and allows the assessment of transmurality and the detection of small infarcts [18].

Kim et al (2001) and Selvanayagam et al (2004) found a clear relationship between the transmurality of infarction and the likelihood of functional recovery after revascularization [19, 20]. He found that if the scar is more than 50 % transmural, there is less than a 20 % improvement in contractility after revascularization (Figure 1.2). Kwong et al (2008) studied the relationship between major cardiac events (MCE) and the area of infarction measured using LGE imaging [21]. He found that even small areas of infarction (<2 % of left ventricular mass) were associated with a seven-fold increase in MCE (arrows in Figure 1.3) MRI LGE imaging has emerged as the gold standard technique for the evaluation of myocardial viability. The ability of LGE MRI to image myocardial infarction (MI) with such high spatial resolution is thus a key advantage over other imaging modalities.

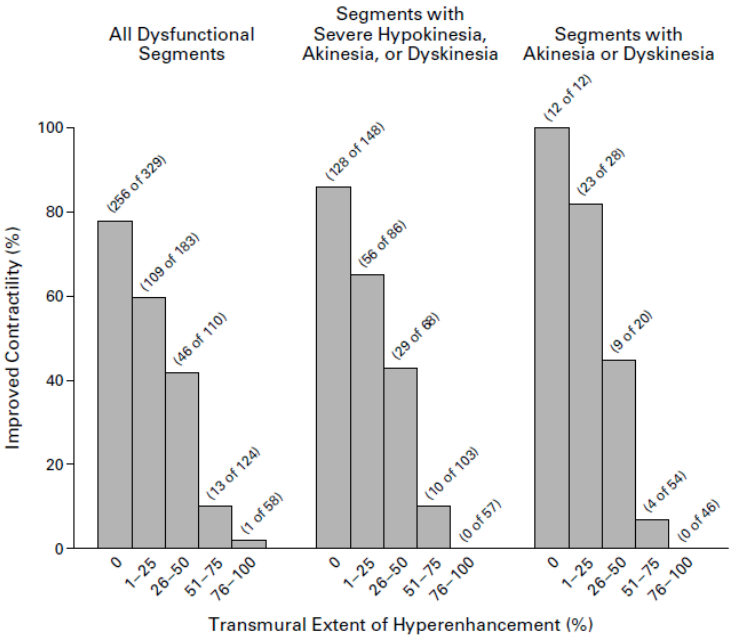

Figure 1-2: Percentage improvement in contractility and its relationship with the transmural extent of hyperenhancement before surgery [19].

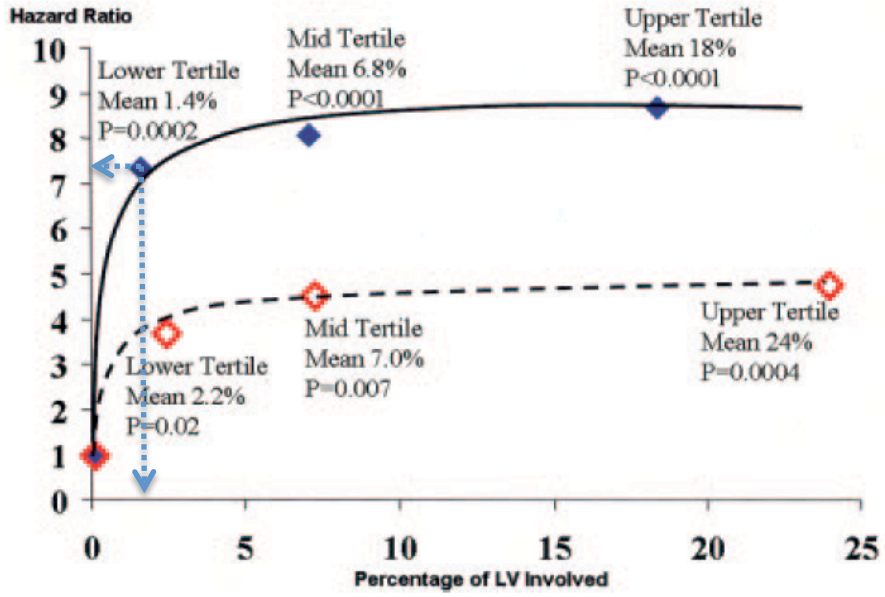

Figure 1-3: Hazard ratio for major cardiac events and its relationship to LGE (blue markers) and wall motion score (red markers) as a percentage of left ventricle involvement [21].

1.4 *Radiofrequency Ablation for Atrial Fibrillation*

In order for the heart to contract in an efficient manner, it must be stimulated by electrical signals which pass down specific conduction pathways to produce ordered contraction and an efficient heartbeat. The timing of electrical stimulation is regulated by the sinoatrial (SA) node which transmits electrical signals along conduction pathways in the atria to the atrioventricular (AV) node. This causes the atria to contract. The AV node then stimulates signals which pass through the ventricles to cause ventricular contraction. AF is the most common irregular heart rhythm or 'arrhythmia'. In AF, the normal regular electrical impulses generated by the SA node are overwhelmed by disorganized electrical impulses usually originating in the roots of the pulmonary veins (PVs), leading to irregular conduction of impulses to the ventricles which generate the heartbeat. Chronic AF leads to a small increase in the risk of death and causes a third of all strokes.

One treatment for persistent AF is catheter ablation where RF ablation is performed around the root of the PVs to create well-defined, limited myocardial

necrosis [22]. The lines of ablation are designed to isolate the PVs and block the trigger points of AF and create a barrier to the propagation of the arrhythmia. This procedure is however often unsuccessful and there are many cases where it has to be re-performed. Traditionally fluoroscopy and 3D mapping devices have been used to monitor the ablation procedure but they are unable to visualize the presence, extent or exact location of the ablation lesions, which are used to indicate the procedural success [23, 24]. MRI has recently been used to image the areas of RF ablation using adapted LGE techniques which were originally developed for imaging ventricular scar [25]. MRI has the advantage that it can visualize the presence and extent of scar and relate this to an exact anatomical location. The extent of atrial scar has been correlated with the success of the ablation procedure [26] and been used to guide repeat procedures [27].

1.5 Magnetic Resonance Imaging

Magnetic resonance imaging (MRI) has great flexibility to manipulate image contrast by employing different pulse sequences and using a variety of extracellular and molecular contrast agents. It is also a non-invasive imaging modality which does not use ionizing radiation. This lends it to serial examinations which are required for the diagnosis, monitoring and screening of disease. It however suffers from inherently low signal-to-noise (SNR) and there exist a vast range of different pulse sequences and adjustable parameters, which make its use challenging and needs well-trained radiographers and physicians. The development and optimization of MRI pulse sequences therefore requires detailed investigation to produce optimal image quality and maximize diagnostic information.

1.6 Thesis Overview

Chapter 2 is a review of the current MRI strategies for aortic and carotid vessel wall imaging. The traditional approach uses the double inversion recovery (DIR) pre-pulse where the inversion time (TI) must be determined using a Look Locker [28] in order to achieve adequate blood suppression after contrast administration. To overcome this limitation, the quadruple inversion recovery

(QIR) pre-pulse was developed [29]. It consists of a DIR pulse, a time delay (TI1), a second DIR pulse, a second time delay (TI2) and the imaging read-out. TI1 and TI2 can be optimized to achieve blood suppression within a wide T1 range (e.g. 100-1400 ms). This means that a Look Locker scan is also no longer required as blood suppression can be achieved before and after contrast administration using identical parameters. The QIR sequence was later modified to image a reduced field-of-view (rFOV) by applying the two inversion pulses in two orthogonal planes [30].

The QIR and rFOV-QIR sequences were mainly tested in the carotid arteries which exhibit little cardiac motion and have relatively constant blood flow throughout the cardiac cycle. To motivate my work in chapter 3, the limitations of the current QIR implementations are described for vessels such as the aorta which exhibit cardiac motion and variable blood flow throughout the cardiac cycle. The zoom imaging technique is also introduced as an alternative to the rFOV-QIR technique for imaging a small FOV [31].

Chapter 3 describes my novel implementation of the QIR pre-pulse to accelerate and optimize black blood properties for imaging the abdominal aortic wall. My hypothesis is that, as there is variable blood flow in the aorta during the cardiac cycle, the sequence must be combined with ECG-triggering. I firstly implemented the QIR sequence with “traditional” ECG triggering where the two DIR pulses are played out after the R-wave. Blood suppression however relies on adequate blood exchange during the second time delay (TI2). Therefore I also implemented “trailing” ECG-triggering where the TI2 time delay is timed just after the R-wave to coincide with peak systolic flow.

I performed simulations and phantom experiments to optimize TI1 and TI2 to minimize the blood signal within the T1 range 100-1400 ms according to the patient’s heart-rate. Ten volunteers were then imaged pre and post-contrast using a conventional ECG-triggered DIR and the QIR implementations with “traditional” and “trailing” ECG-triggering. Zoom imaging was also employed to

accelerate imaging time and achieve a small FOV. I found that the blood SNR and vessel-wall-to-blood CNR, vessel wall sharpness and image quality scores for the 'trailing' QIR images were significantly improved compared to the 'traditional' QIR implementation and untriggered QIR images. This work has extended the use of the QIR sequence to achieve pre and post contrast black blood scans with identical parameters for vessels with variable blood flow or motion.

Chapter 4 describes the current clinical and research LGE MRI techniques used to image myocardial scar. The current gold standard inversion recovery (IR) sequence consists of one non-selective inversion pulse followed by an inversion delay (TI) and the imaging read-out [32]. The TI is chosen using a preceding Look Locker scan to null healthy myocardium. As there is contrast uptake in areas of scar, they have a shorter T1 value and are bright compared to healthy myocardium on IR images. The IR sequence is however only capable of suppressing signal from one T1 species. As blood often has a T1 value just greater than that of scar, it also has high signal in the IR images. The resulting poor scar-to-blood contrast can hamper the detection of small regions of scar and the measurement of transmurality and scar size. In this chapter, I discuss the factors which affect the scar-to-normal myocardium contrast and scar-to-blood contrast in the IR sequence including: the choice of TI, the contrast agent, dosage and timing of imaging. I also briefly discuss the approaches to scar quantification in IR images. I then describe several alternative approaches to the IR sequence including; the phase sensitive inversion recovery (PSIR) sequence [33], T1 and T2 mapping techniques [34, 35] and diffusion sensitized gradients (DSG) [36].

I then discuss a flow-dependent technique which uses a slice selective inversion pulse and a non-selective inversion pulse to achieve simultaneous suppression of the blood and the normal myocardium [37]. However, the blood suppression was found to be significantly less effective in patients with an ejection fraction less than 40 %. This motivates my work in chapter 5 to develop a novel flow-

independent sequence for LGE imaging which reduces the blood signal to improve the detection of scar and the assessment of transmurality.

Chapter 5 describes my work to design and test a new sequence to improve blood suppression in LGE images of myocardial scar. The dual-IR sequence consists of a non-selective IR pulse, a time delay (TI1), a second non-selective IR pulse, a second time delay (TI2) and the imaging read-out. TI1 and TI2 are optimized to achieve signal suppression within a defined T1 range. This means that only tissues with very short T1 values will have high signal while the signal from all other T1 species will be suppressed. My hypothesis is that the dual-IR sequence can null the signal from normal myocardium and reduce the signal in the blood whilst maintaining high signal in the regions of scar.

I performed simulations to optimize the TI1 and TI2 delays to suppress the signal in the following T1 ranges: 50-1400 ms, 100-1400 ms, 200-1400 ms and 300-1400 ms according to the patient's heart-rate. I then validated the signal characteristics of the IR and dual-IR sequences in phantom experiments. I then imaged 12 patients with known myocardial scar at 10, 20 and 30 minutes after contrast administration with the two dimensional (2D) IR sequence and the 2D dual-IR sequence with different T1 suppression ranges and at different time points. I found that there was significantly improved scar-to-blood CNR for the dual-IR technique compared to the IR technique. The dual-IR sequence also gained higher confidence scores for scar detection and transmurality assessment and resulted in more consistent assessment of scar size and transmurality between readers compared to the IR sequence.

Chapter 6 describes the current research into using LGE images to visualize atrial and PV scar after RF ablation for AF. A 3D IR-TFE sequence is normally used to image the PVs and atrial wall which are much thinner than the ventricular walls. This allows the images to be reconstructed as a 3D shell so that the small areas of scar can be related to the complex anatomy of the atria and PVs. This 3D map of scar can then be compared to the electrophysiological

(EP) information to establish a correlation between areas of scar and conduction pathways.

As with imaging of ventricular scar, there is often high blood signal in the IR images which can hamper the detection of scar. This means that imaging is often performed at least 25 minutes after contrast administration which increases the overall scan time. I also describe the causes of the PV in-flow artifact and several approaches to reduce its effect. This motivates the work described in chapter 7 in which I evaluated the dual-IR pre-pulse for LGE imaging of PV and atrial wall scar.

Chapter 7 describes my work to combine the dual-IR pre-pulse with a 3D-TFE read-out and test the sequence for visualizing PV and atrial wall scar. Following RF ablation for AF, 13 patients underwent dual-IR imaging at 15, 20 and 30 minutes post-contrast and IR imaging at 25 minutes. I also combined the sequence with an alternative respiratory navigator method to reduce the PV in-flow artifact [38]. I found that the CNR between the scar and the blood was significantly higher with the dual-IR sequence at 30 minutes compared to the IR sequence at 25 minutes. This may improve the conspicuity of lesion detection and allow imaging earlier after contrast administration.

Chapter 8 summarizes the findings of the three projects described in chapters 3, 5 and 7 and discusses possible future work.

Chapter 2

2. Review of Vessel Wall MRI Techniques

2.1 *Introduction*

Requirements for a vessel wall MR sequence include high spatial resolution and reliable blood suppression as well as extensive spatial coverage of the vasculature within an acceptable scan time. When contrast agents are employed, the area of contrast uptake must be clearly visualized and reliably compared with pre-contrast images. The ultimate aim of vessel wall imaging is to identify vulnerable plaques which are characterized by a thin fibrous cap, a large lipid core, calcification and significant inflammatory cell infiltration [10, 39, 40]. An ideal MR imaging strategy should therefore include sequences which can a) visualize the lipid core, b) identify the fibrous cap and measure its thickness and c) visualize inflammation in the cap [11].

Several studies have employed different MR sequences with and without contrast agents to characterize plaque components [9, 12-14, 41, 42]. A common approach is to combine pre-contrast T1 and T2 weighted TSE imaging and post contrast T1-weighted imaging along with a post-contrast angiogram (MRA) to visualize the lumen of the vessel. Although our study was specifically aimed at developing a sequence for the aorta, in this chapter I will also discuss sequences applied to the carotid arteries. It should be noted that vessel wall sequences are often tested in these vessels in the first instance and later employed to image the coronary arteries which can be more technically challenging.

2.2 *Methods of Blood Suppression*

The spin echo (SE) sequence has inherent black blood properties. In order for spins to produce a signal, they must experience both the 90 ˚ excitation pulse and the 180 ˚ refocusing pulse. If blood which has not experienced the 90 ˚ excitation pulse flows into the imaging slice during the echo time (TE), this will reduce the signal produced. As this cannot always be relied on to null blood signal, there are a number of additional measures used to ensure blood suppression which are briefly described in this section.

2.2.1 Spatial Pre-saturation

Spatial pre-saturation employs a spatially selective saturation band which is applied adjacent to the imaging volume. This saturates the signal of the blood flowing into the imaging volume [43, 44]. Although this approach is less sensitive to T1 changes of blood, it does rely on precise timing to ensure that the suppressed blood is passing through the desired imaging slice at the time of image acquisition (Figure 2.1).

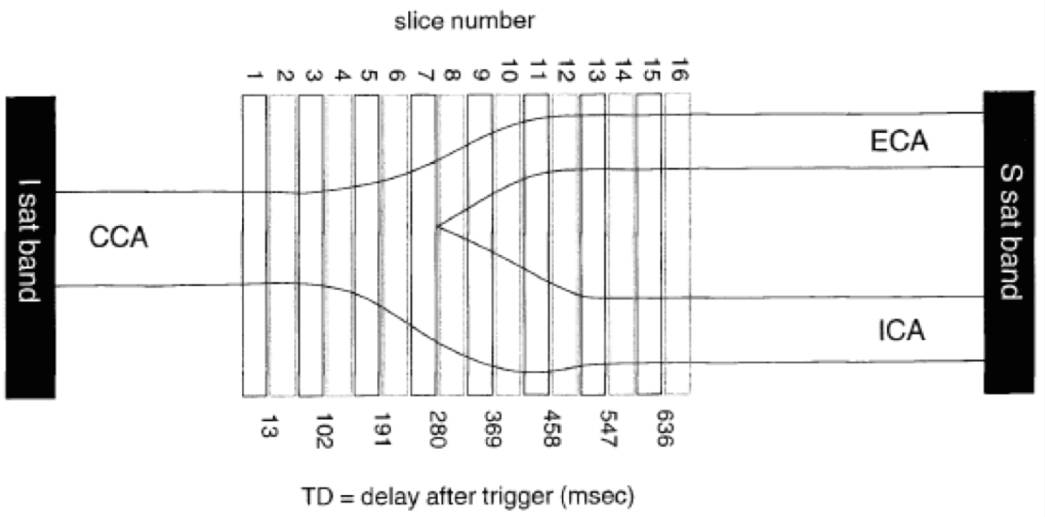

Figure 2-1: The use of a saturation band which nulls the blood signal which is then imaged in slices downstream with an incremental trigger delay [43].

2.2.2 Double Inversion Recovery Pre-pulse

The DIR pre-pulse consists of a non-selective 180 ° inversion pulse immediately followed by a slice-selective 180° re-inversion pulse, followed by an inversion time delay (TI) and the imaging read-out (Figure 2.2) [45, 46]. The static tissue and the blood within the slice will experience both 180 ° pulses and their magnetization will therefore be almost completely restored. Assuming there is complete blood exchange during the TI delay time, at the time of imaging the blood within the slice will have only experienced the non-selective 180 ° inversion pulse. During TI, the blood signal will also experience T1 relaxation. The TI must be set so that the read-out is timed to coincide with the point at which the blood signal is zero.

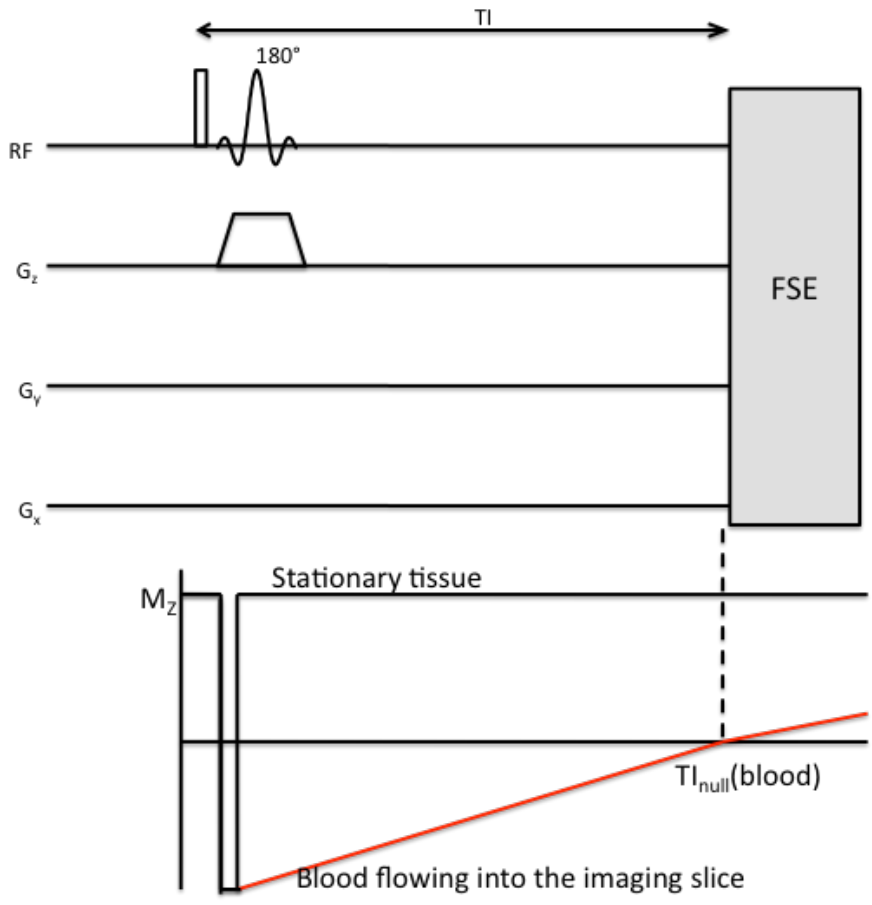

Figure 2-2: The DIR pulse sequence

Kramer et al (2004) used T1-weighted (pre and post contrast) and T2-weighted sequences (pre-contrast) along with an MRA in 23 patients who were undergoing surgery for abdominal aortic aneurysm (AAA) [11]. The area of the aneurysm which demonstrated significant plaque burden was imaged both before and after contrast administration. The study showed that it was possible to identify both thrombus and lipid core and fibrous cap on both pre-contrast T1-weighted images (Figure 2.3a). There was also fibrous cap enhancement on post-contrast T1-weighted images (Figure 2.3b).

The plaque components identified on MR images were found to be in good agreement with histopathology performed on the corresponding slice of the aorta resected during surgery. In addition there was a greater increase in post-contrast enhancement on T1-weighted images in patients in which histology identified an infiltration of inflammatory cells within the fibrous cap compared to those without inflammation.

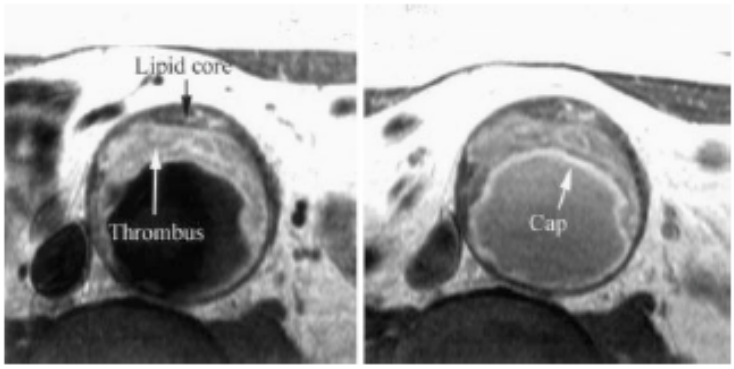

Figure 2-3: Pre-contrast (left) and 5 minutes post contrast (right) T1 weighted imaging [11].

Although there appears to be enhancement of the fibrous cap in the post contrast T1-weighted image, there is inferior blood suppression compared to the pre-contrast image. The approach employed in this study was to maintain the TI which was used before contrast administration for the post-contrast imaging. On the one hand this ensures parameters are identical for both scans which allows a direct comparison between the two images and a reliable assessment of the percentage contrast enhancement. However, as the T1 of blood is significantly shortened after contrast administration, imaging is no longer performed at the null point of blood, hence the appearance of suboptimal blood suppression in Figure 2.3b.

An alternative approach is to shorten the TI value for the post-contrast scans to ensure the optimal TI is used to achieve blood nulling. There are potential issues with this approach though when employing long acquisitions during which the blood T1 can change. This means that the optimal TI set at the beginning of the scan may no longer achieve good blood suppression at the end of the scan.

2.2.2.1 Choosing the Correct TI Value to Null Blood

Before contrast administration, the T1 of blood (T_1^{blood}) can be assumed to be constant for most patients. It has been measured as approximately 1200 ms at 1.5 T [34, 47, 48]. The following equation can then be used to calculate the optimal TI:

$$TI = T_1^{blood} \ln(2)$$

Equation 2-1

If the TR_{eff} is insufficient to allow for complete T1 recovery before the following inversion pulse, then the Fleckenstein formula [49] must be used to calculate the correct TI:

$$TI = T_1^{blood} [\ln(2) - \ln(1 + \exp(-TR_{eff} / T_1^{blood}))]$$

Equation 2-2

2.2.2.2 Look Locker Scans

After contrast administration, the T1 of blood can be difficult to predict due to its dependency on the type of contrast agent, dosage, patient physiology and time after contrast. In this case, a Look Locker scan [28] can be performed just prior to imaging to choose the optimal TI on a patient specific basis. The Look Locker scan is a method of T1 quantification which employs a 180 ° inversion pulse. The signal is then sampled at multiple time points during recovery using many low flip angle excitations. Due to the application of RF excitation pulses, some fraction of the longitudinal magnetization (M_z) is moved into the transverse plane with each excitation. The relaxation process is therefore affected and M_z recovers with an apparent T1 known as T1* which is less than the true T1. Instead of converging to the equilibrium magnetization, M_0, M_z converges to M_0* where:

$$M_z(TI) = M_0 - (M_0 + M_0^*)e^{-TI/T_1^*}$$

Equation 2-3

The apparent T1* is related to the true T1 using the following equation:

$$T_1^* = \frac{TR}{\frac{TR}{T_1} - \ln(\cos\alpha)}$$

Equation 2-4

where TR is the repetition time and α is the flip angle.

2.2.3 Quadruple Inversion Recovery Pre-pulse

Because the DIR pre-pulse can only null the blood signal from one T1 species, the TI must be changed post-contrast as the T1 of the blood is shortened. To deal with this problem, the QIR pre-pulse was developed [29]. It aims to achieve pre and post contrast blood signal suppression with identical imaging parameters. It consists of a DIR pre-pulse, a time delay TI1 and second DIR pre-pulse, followed by TI2 and the imaging read-out (Figure 2.4).

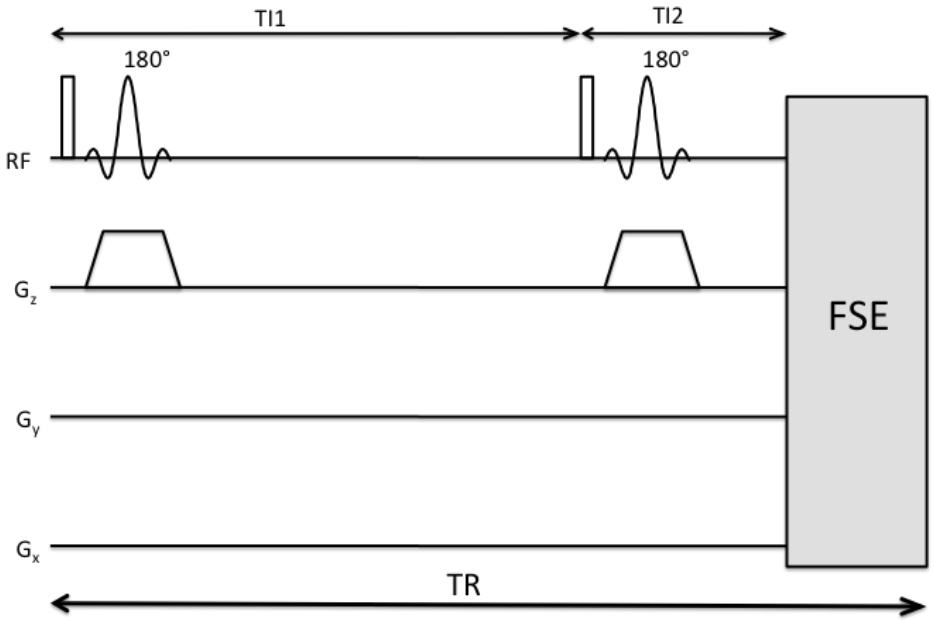

Figure 2-4: The QIR pulse sequence as implemented for carotid artery imaging (adapted from [29]).

The use of two inversion pulses to achieve simultaneous signal suppression of two T1 species has been previously explored and has been used to image the brain and the lungs [50, 51]. A 90 ˚ preparation pulse followed by a series of two, three or four pulses has also been optimized to null not just two T1 species but an entire range of T1 values to achieve background suppression in angiography applications [52, 53].

The aim of the QIR pre-pulse is to null the signal of both pre and post contrast blood. In the work by Yarnykh et al (2002), rather than setting the two inversion delays (TI1 and TI2) to null two specific T1 species, the delays was specifically optimized to achieve complete signal suppression for a wide range of T1 values. In this way, it is not necessary to know the precise T1 of blood before or after contrast administration which means there is no need for a Look Locker scan. Furthermore, the QIR technique should be insensitive to changes in the blood T1 during the acquisition.

The steady state M_z of blood (Mzb) at the time of imaging in the DIR and QIR sequences can be expressed as a function of the delays (TI, TI1 and TI2), and T1 using the following equations [29]:

$$M_z b^{QIR} = 1 - \frac{2\exp(-TI2/T1)[1-\exp(-TI1/T1)}{1-\exp(-TR_{eff}/T1)}$$

Equation 2-5

$$M_z b^{DIR} = 1 - \frac{2\exp(-TI/T1)}{1+\exp(-TR_{eff}/T1)}$$

Equation 2-6

The TI1 and TI2 delays were optimized to minimize the integral of $(M_z b^{QIR})^2$ between $T1_{min}$ and $T1_{max}$ for a fixed effective TR (TR_{eff}) of 400 and 800 ms. Optimizations were performed with $T1_{max}$ always set as 1400 ms and $T1_{min}$ set at 100 ms and 200 ms. When the QIR pre-pulse was performed with optimized delays, it achieved blood signal suppression within a wide T1 range (Figure 2.5a). This compares to the DIR sequence which only suppresses the signal from one specific T1 value (Figure 2.5b).

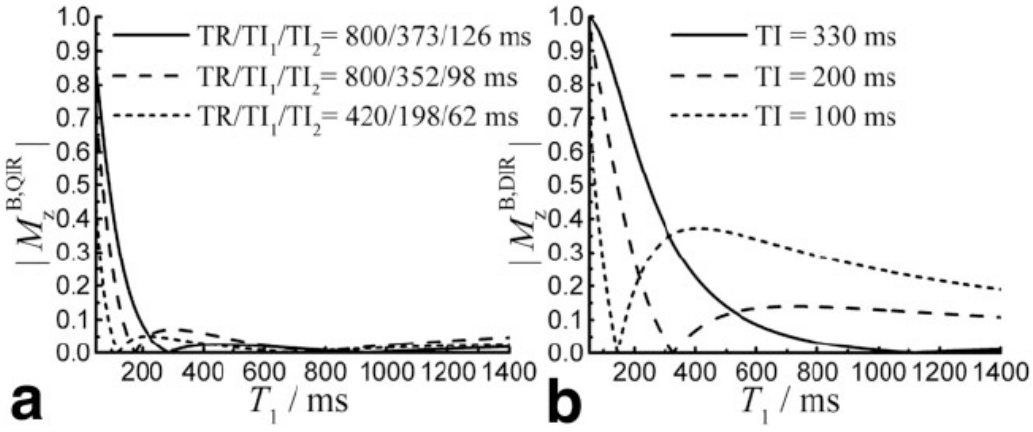

Figure 2-5: Plots of the Mzb versus T1 value for a) the QIR and b) the DIR sequence [29].

Yarnykh et al (2002) tested the signal characteristics of the two sequences by imaging a flow phantom with the QIR and DIR sequences. Fluid with four different T1 values was pumped through the phantom and the results confirmed that each T1 fluid was suppressed by the QIR sequence whereas only one species was suppressed by the DIR sequence. The QIR sequence with optimized delays was then used to image three patients with carotid artery atherosclerosis and compared to the DIR technique. The QIR sequence applied pre (Figure 2.6a) and post contrast (Figure 2.6b) successfully achieved blood suppression with identical parameters and showed post-contrast enhancement in the vessel wall (arrow). This is compared to the DIR sequence which achieved good blood suppression pre contrast (Figure 2.6c) but when applied post contrast with identical parameters exhibited flow related artifacts (Figure 2.6d).

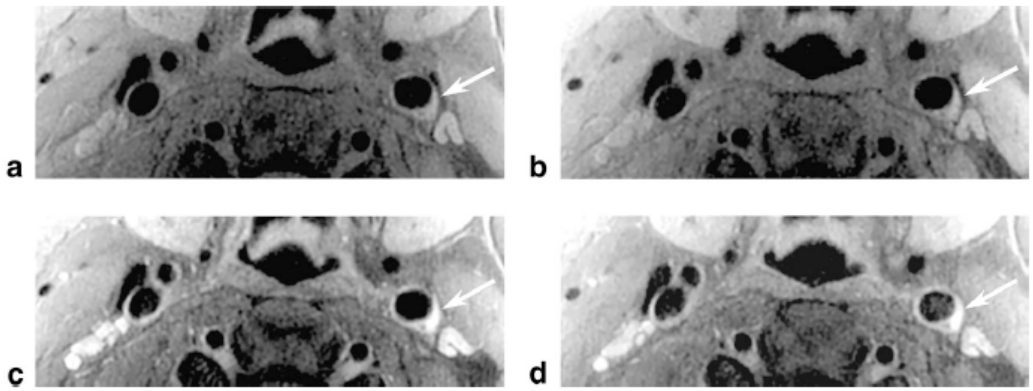

Figure 2-6: Pre and post contrast QIR and DIR images of a patient with a carotid artery plaque [29].

Yarnykh et al (2002) also investigated the effect of the DIR and QIR pre-pulses on stationary tissue signal. They found that both pre-pulses caused a significant reduction in the signal intensity from both $MnCl_2$ solution and bovine muscle compared to the unprepared TSE sequence (Figure 2.7). Both the QIR and DIR pre-pulses reduced the muscle signal more than the signal from $MnCl_2$ solution. The typical biexponential shape of the dependence of the signal on TI for muscle indicates the presence of the magnetization transfer effect which is the result of specific saturation of macromolecular protons by DIR pulses. The signal intensity was also shown to be dependent on the TI used in the DIR sequence with a short TI allowing less time for recovery of signal after the application of the pre-pulse. They found that when the DIR and QIR sequences were used to image patients with atherosclerotic plaque that the average percentage contrast enhancement of muscle was 32 % in the QIR sequence compared to 19 % in the DIR sequence. The range of enhancement in the plaque was 71-113 % in the QIR sequence compared to 54-101 % in the DIR sequence. This indicated that changing the TI after contrast administration can reduce the signal from stationary tissue which could cause an underestimation in contrast enhancement. As the QIR sequence can be applied pre and post contrast with inversion delays maintained, it appears not to suffer from this inaccuracy.

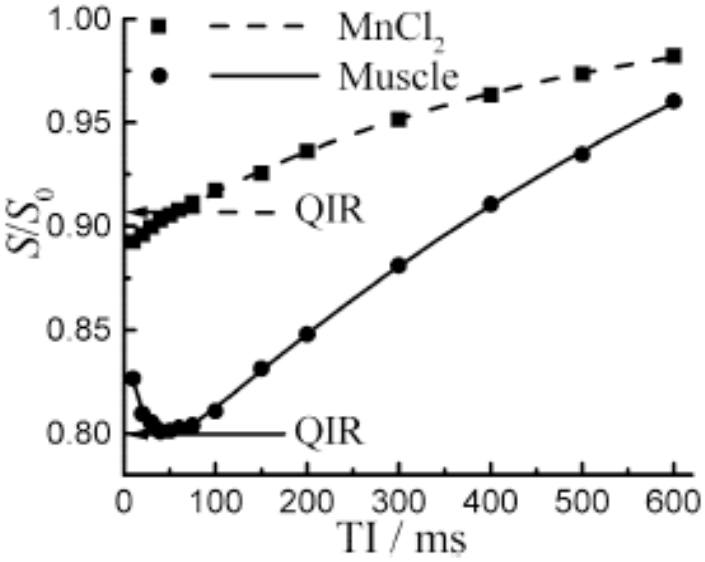

Figure 2-7: Signal intensity measurements (S) normalized to the signal in unprepared TSE sequence (S_0) for bovine muscle and $MnCl_2$ solution with the QIR pre-pulse and DIR pre-pulse with a range of TI values [29].

2.2.4 Diffusion Sensitizing Gradients

The blood suppression in DIR and QIR sequences relies on the complete exchange of blood which can be compromised for thick imaging slices, slow or complex flow and short TI or TI2 delays. There has been work employing 'diffusion-sensitizing gradients' (DSG) to suppress the blood signal. This technique has been applied to carotid arteries first using a 3D steady state free precession (SSFP) acquisition [54] and then with a 2D multi-slice TSE acquisition [55].

The DSG pre-pulse is performed just prior to the imaging readout and consists of 90 ° - 180 °- 90 ° non-selective pulses combined with a pair of unipolar motion–sensitizing gradients positioned on either side of the 180 ° pulse (Figure 2.8). The first 90 ° pulse tips the magnetization into the transverse plane, after which the gradients, which are applied in all three directions, cause an accelerated dephasing of flowing spins. The 180 ° pulse flips the magnetization within the x-y plane after which the applied gradient causes a refocusing of the spins. The 90 ° then tips the magnetization back along the equilibrium direction. A spoiler gradient ensures that any residual transverse magnetization is destroyed.

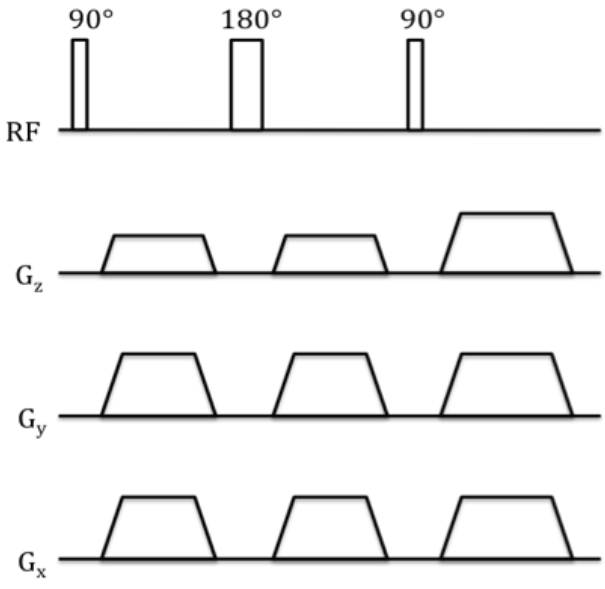

Figure 2-8: The diffusion sensitizing gradients (DSG) pre-pulse module (adapted from [56]).

The level of gradient sensitization is dependent on the gradient amplitude, duration and direction. As well as reducing the signal from moving spins, the DSG module can also lead to signal loss in the vessel wall as a result of T2 decay as well as loss of signal from diffusion effects rather than flow. To reduce these unintended effects, the gradients should ideally be applied at maximum amplitude and minimum duration. However, applying the gradients in such a way results in eddy-current effects. In an attempt to overcome this problem, the DSG module has recently been combined with a DIR preparation and TSE readout [56] which allowed a shorter DSG module duration. When applied in volunteers, the DIR-DSG resulted in fewer flow related artifacts and no significant difference in vessel wall SNR compared to the DIR-TSE technique.

2.3 *2D and 3D Imaging*

2D imaging involves applying the excitation pulse simultaneously with a slice selective gradient in order to isolate one slice for imaging. 3D imaging involves excitation of an entire 3D slab and applying phase encoding in two orthogonal directions and frequency encoding along the third. A 3D k-space is filled and a 3D Fourier transform is performed to reconstruct a 3D dataset. The advantages of a 3D acquisition include an increased SNR and good spatial coverage. It also allows thinner slices to be reconstructed which can reduce partial volume effects and to detect smaller plaque components compared to a 2D acquisition.

Spatial pre-saturation and DIR and QIR pre-pulses can provide good blood-suppression when imaging individual 2D slices. However, there may be insufficient blood suppression in 3D images due to incomplete blood exchange within the entire 3D volume. 3D is also time-consuming as phase encoding must be performed in two spatial dimensions. A faster alternative is a multi-slice 2D acquisition which acquires all the data for one slice location at a time. One advantage of the DSG approach is that it does not rely on the complete out-flow of blood and can therefore be applied to a 3D imaging volume [54].

2.4 *Methods of Outer Volume Suppression*

A common application of the black blood vessel wall imaging techniques is to screen for aortic plaques. The DIR-TSE technique has been used to create a series of 2D transverse imaging slices which extend from the aortic arch to the aorta-iliac bifurcation. In order to achieve the imaging time of 20 minutes, the sequence acquired 24 slices with a slice gap of 10 mm [57]. For effective screening, it is desirable to have no slice gap but this was not possible due to time constraints. One way to speed up image acquisition is to image a reduced FOV. This section will describe two such techniques.

2.4.1 QIR with Reduced Field-of-view Imaging

A modification to the original QIR sequence was implemented in order to achieve outer volume signal suppression for a multi-slice approach [30]. Within each DIR pulse pair, the two inversion pulses are applied in two orthogonal planes which are the imaging plane ('Z-slice' in Figure 2.9b) and the slab which is the width of the FOV in the phase-encoding direction ('Y slab' in Figure 2.9b). The spins within the region where the Y slab and the Z-slice intersect are re-inverted ('re-inverted volume' in Figure 2.9b). The inflowing blood on the other hand only experiences the inversions in the Y direction.

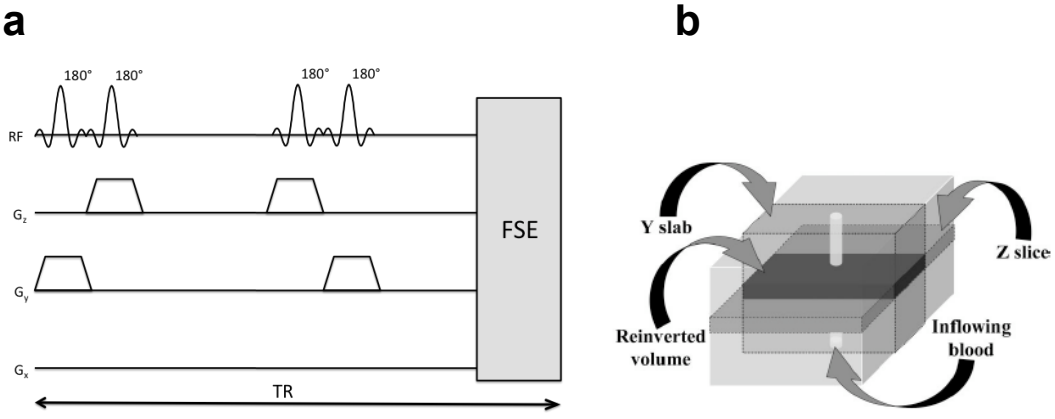

Figure 2-9: QIR with a small FOV implementation a) pulse sequence and b) schematic diagram of inversion planes [30].

Both single slice and multi-slice versions of the SFQIR were implemented. In simulations and phantom studies, the outer volume suppression in the single slice technique was found to be superior for shorter TR_{eff} values (Figure 2.10a). The multi-slice implementation required a longer TR as the entire imaging sequence for each slice is applied within the time TR_{eff}/Ns where Ns is the number of slices. The multi-slice approach therefore requires a longer TR_{eff} value. For a constant TR_{eff} of 4000 ms, the outer volume suppression was plotted versus T1 for different Ns values. It was found that higher number of imaging slices resulted in improved signal suppression in the desired T1-range (Figure 2.10b).

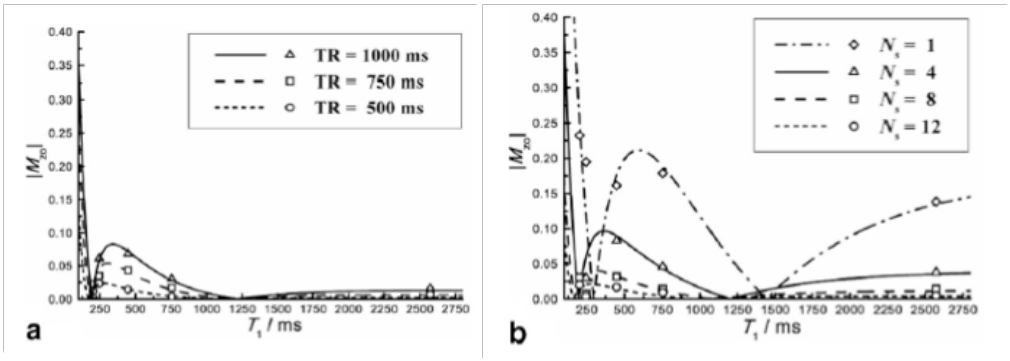

Figure 2-10: Signal in the outer volume as a function of T1value in a) the single slice techn ique with different TR_{eff} times and b) the multi-slice technique with a constant TR_{eff} of 4000 ms and different number of slices [30]

The delays used for the experiments presented in Figure 2.10 were optimized to null tissue in the outer volume for T1 values between 100 ms and 2500 ms rather than the blood signal. The simulated signal values for the blood using these delays was found to be suboptimal compared to the signal characteristics obtained with the QIR sequence with delays specifically optimized for blood suppression (Figure 2.11).

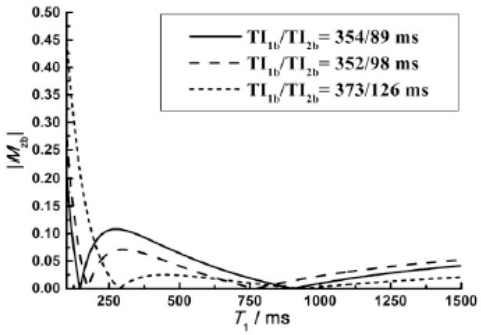

Figure 2-11: Signal characteristics for single-slice SFQIR sequence acquisition with a) delays optimized to suppressed outer FOV (solid line) compared to b) and c) delays optimized to null blood in T1 ranges 100 and 200 ms to 400 ms respectively (dotted lines) [30].

In volunteer studies in the aorta, they found that the single-slice SFQIR sequence achieved good outer volume suppression which helped to reduce the artifacts which result from the motion of the abdominal wall (Figure 2.12). This sequence was applied with a slice thickness of 4 mm and a non-gated free breathing approach.

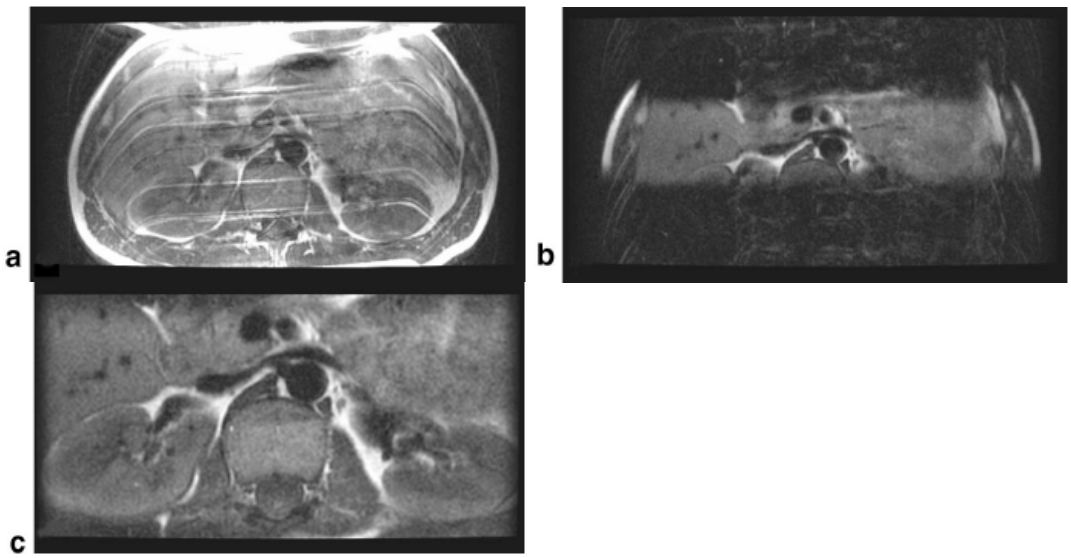

Figure 2-12: Imaging of the abdominal aorta with the SFQIR sequence. a: Reference T1-weighted DIR-FSE image, b: Outer volume suppression achieved with the SFQIR-FSE technique and c: Reduced-FOV SFQIR image with improved in-plane resolution. All images were obtained with a single-slice, untriggered, free-breathing acquisition [30].

One limitation of SFQIR is that the level of blood suppression in the multi-slice approach is dependent on the number of slices imaged. In addition, the sequence was tested in only 4 volunteers for aorta imaging and measurements of the vessel wall and blood SNR and CNR were not included. The outer volume signal is not entirely eliminated by the sequence, which may risk residual artifacts. The SFQIR sequence is still flow-dependent and the slice thickness is thus limited by the need for out-flow. In the multi-slice approach the authors suggest that the blood suppression is aided by the bidirectional saturation of the inflowing blood.

2.4.2 Zoom Imaging

Zoom imaging is a method which allows a small FOV to be imaged. It is implemented for the TSE technique by applying the slice-selection and refocusing pulses in orthogonal planes (Figure 2.13). The 90 ° excitation pulse is applied simultaneously with a phase encoding gradient which only excites spins within the FOV in the phase-encoding direction [31]. The 180 ° refocusing pulse is applied in the slice-select direction. Signal will be generated only from those spins which lie in the region which is crossed by both gradients and have experienced both excitation and refocusing pulses. As there is no signal generated outside of this region, the FOV in the phase encoding direction can be reduced to encompass only this region without wrap-around artifacts. Fewer phase encoding steps can thus be employed which reduces the imaging time.

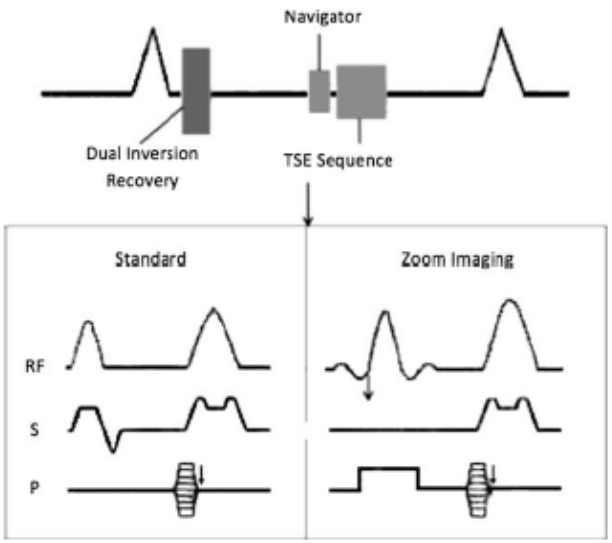

Figure 2-13: TSE readout for standard full FOV and zoom imaging [58].

Hussain et al (2011) performed a study in the abdominal aorta to compare DIR-TSE with a full FOV, DIR-TSE with a reduced FOV using zoom imaging and DIR combined with SENSE acceleration [58]. They found that zoom imaging reduced the imaging time and had no significant difference in CNR or vessel wall sharpness compared to full FOV imaging. Although there was a decrease in SNR due to the acquisition of fewer phase encoding lines, there was good agreement in vessel wall thickness measurement. In comparison, SENSE reduced CNR and resulted in an underestimation of the vessel wall thickness compared to the conventional DIR-TSE full FOV imaging sequence.

2.5 *Blood Flow and ECG-triggering*

Both the DIR and QIR techniques rely on complete blood exchange during TI or TI2 respectively. Studies have examined the variation of blood flow during the cardiac cycle in the aorta and carotid arteries. The velocity of blood can be measured using MRI by employing a sequence known as phase contrast (PC) MRI [59-61]. It employs a set of bipolar gradients (Figure 2.14). The effect of a gradient is to induce a phase shift proportional to the area of the gradient. A positive gradient induces a positive phase shift on stationary tissue. As this is followed by a negative gradient which is equal in area, the phase shift induced by the positive gradient is cancelled out so that the net effect of the two gradient lobes is zero phase shift. As blood is moving along this gradient during its application, the net phase shift is proportional to its velocity, v(t).

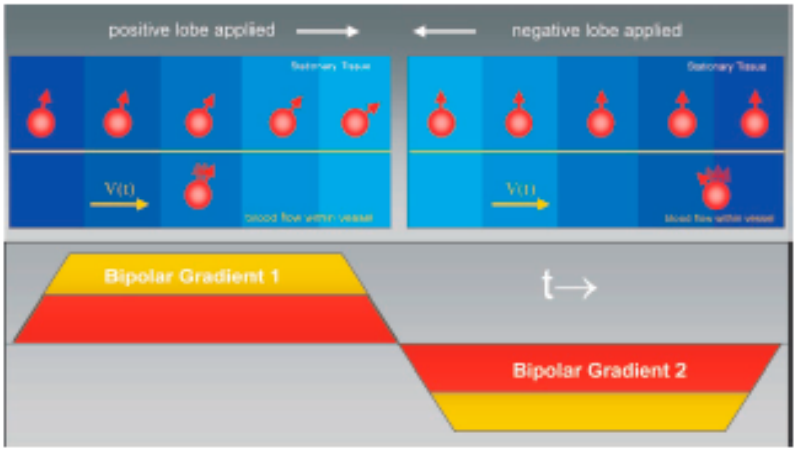

Figure 2-14: PC mapping pulse sequence [62]

When applied to vessels such as the aorta, the velocity of blood can be measured at different time points in the cardiac cycle. The flow rate (F) can be calculated at each point in the cardiac cycle as:

$$F = v(t).A$$

Equation 2-7

where A is the area of the vessel measured in magnitude reconstructed images.

Cheng et al (2003) used PC-MRI to measure the flow at the supraceliac and infrarenal levels in the abdominal aorta [63]. They performed the measurements both at rest and after exercise. They found that at rest there is a large peak of forward flow (point A in Figure 2.15) after about 200 ms. At the infrarenal level, there is then a small amount of backward flow or 'regurgitation' at about 400 ms (point B). This is followed by a period of very little flow for the remainder of the cardiac cycle. After exercise, the forward peak is higher and there is no regurgitation. Although the period of diastole is shortened at higher heart-rates, the period of systolic flow is however maintained at approximately 400 ms.

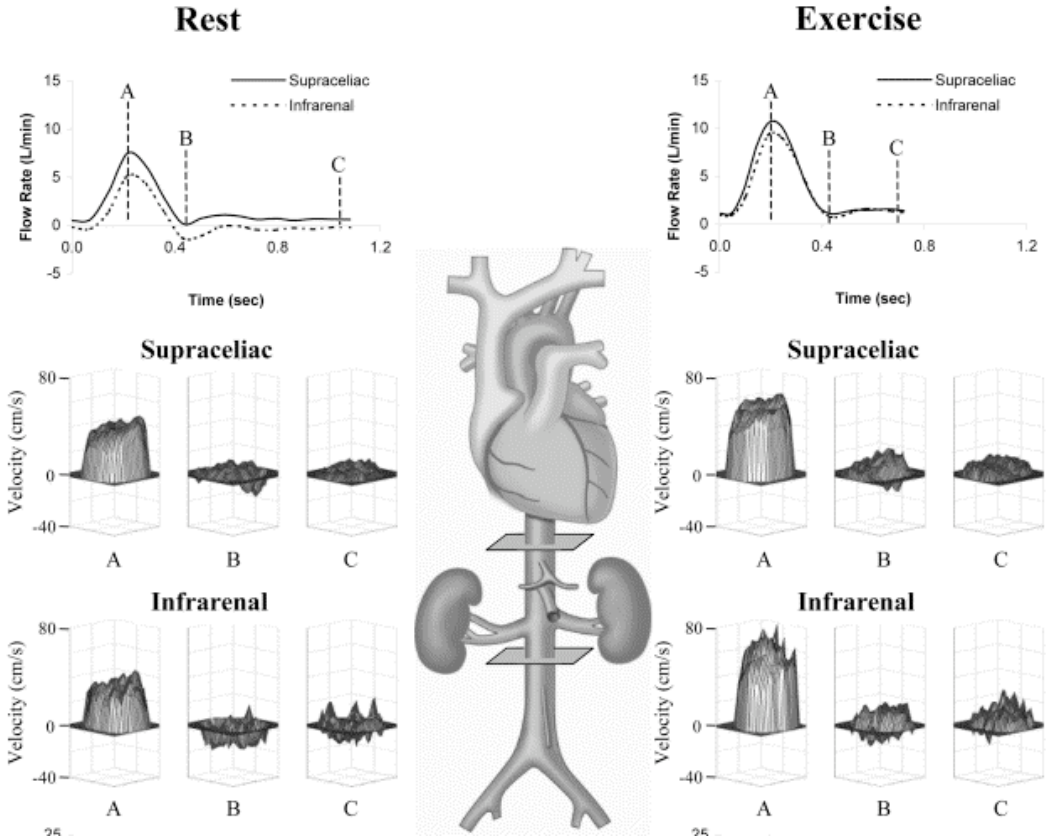

Figure 2-15: Blood flow measurements in the supraceliac and infrarenal locations in the abdominal aorta at rest and at rest [63].

In order to achieve sufficient blood suppression when imaging the aorta, there must be complete blood exchange within the TI period, the DIR-TSE sequence is triggered on the R-wave of the ECG. The inversion pulse is performed immediately after the R-wave so that there will be maximum blood exchange before the imaging is performed. The flow profiles in Figure 2.15 indicate that there is maximum flow in the centre of the vessel which falls to zero at the edge of the vessel. If there is poor blood suppression due to slow flow, these artifacts will often appear at the edges of the vessel wall which can mimic vessel wall enhancement.

Harloff et al (2009) performed similar flow measurements in the carotid arteries [64]. There is a peak in systole after about 150 ms but, in comparison to the aorta, there is a baseline level of flow throughout the entire cardiac cycle (Figure 2.16). Carotid artery imaging is often performed without the use of cardiac triggering because it can be assumed that whenever the inversion pulse and imaging sequence are applied, there will be sufficient flow to allow complete blood exchange to occur. There is also little motion of the carotid arteries throughout the entire cardiac cycle, so that imaging can be performed at any time in the cardiac cycle without significant motion artifact.

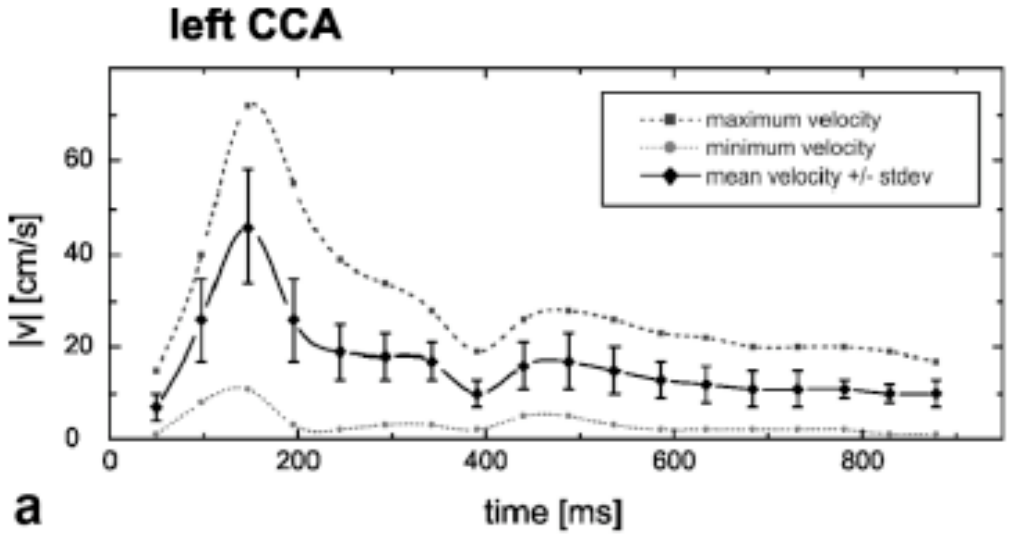

Figure 2-16: Mean, maximum and minimum blood velocities over the cardiac cycle measured in eight normal volunteers in the left common carotid artery using 4D PC cine MRI [64].

2.6 *Summary*

In summary, the original implementation QIR and rFOV-QIR sequences were mainly tested in the carotid arteries which exhibit little cardiac motion and have limited variability in blood flow throughout the cardiac cycle. This limits the use of the current QIR implementations for vessels such as the aorta which have variable flow during the cardiac cycle.

Chapter 3

3. Novel Implementation of the Quadruple Inversion Recovery Sequence for Aortic Vessel Wall Imaging

3.1 *Introduction*

In the original implementation of the QIR sequence described in chapter 2, no ECG triggering was performed; the TR_{eff} was therefore an independent parameter, which was optimized together with TI1 and TI2 to achieve optimal signal suppression within the user defined T1 range [29]. I hypothesize that in blood vessels, which are subject to cardiac or respiratory motion and/or have variable blood flow such as the aorta, image quality and blood suppression may be improved by combining the sequence with cardiac triggering and by synchronizing the second DIR pre-pulse with systolic blood flow. Thus, the TR_{eff} must be set to equal a multiple of the patient's RR interval. I also explored the combination of the new QIR implementation combined with 'zoom' imaging.

3.2 *Methods*

3.2.1 Simulations

3.2.1.1 Optimization of the TI1 and TI2 Delays in the QIR Sequence

M_zb at the start of the imaging readout in the QIR and DIR sequences can be predicted by equations 2.5 and 2.6 [29]. Simulations in MATLAB were performed using equation 2.6 to plot M_zb^{QIR} for all T_1 values up to 1400 ms. TR_{eff} was set to equal the RR-interval for heart-rates between 30 and 120 bpm at 15 bpm intervals. For each heart-rate, the optimal values of TI1 and TI2 were calculated by minimizing the integral of M_zb^{QIR} between 100 ms and 1400 ms. The optimal TI1

and TI2 times were plotted versus the RR interval. A cubic equation was then fitted to the curves to enable the optimal TI1 and TI2 times to be predicted for any RR interval. For comparison, M_zb^{DIR} was also simulated for each heart-rate using equation 2.5, with TI values calculated to null the blood signal for pre and post-contrast T1 values (1200 ms and 200 ms respectively) using the Fleckenstein formula [49].

3.2.1.2 Simulation of the Evolution of M_zb during DIR and QIR sequences

Equations 2.6 and 2.7 assume that M_zb has reached a steady state between cardiac cycles. Further simulations were performed in order to examine the behavior of the signal throughout the sequence and to find out how many heartbeats were required to reach as steady-state between heartbeats. Assuming that the blood within the imaging slice will be replaced each heartbeat, it will only experience the non-selective inversion pulse(s). In each RR period, blood will therefore experience:

DIR Sequence: 180 °– TI – TD

Equation 3-1

QIR Sequence: 180 °– TI1 – 180 °– TI2 – TD

Equation 3-2

where TD is the time between the beginning of the imaging sequence and the following inversion pulse. The DIR and QIR pulse sequence diagrams were shown graphically in Figures 2.2 and 2.4.

When the DIR and QIR sequences are combined with a zoom readout, it is possible that the inflowing blood has also experienced the 90 º excitation pulse which is applied with the phase encoding gradient. Simulations were therefore also performed assuming that within in each RR interval the blood will have experienced:

DIR Sequence + zoom: 180 °– TI – 90 °- TD

Equation 3-3

QIR Sequence + zoom: 180 °– TI1 – 180 °– TI2 – 90 °- TD

Equation 3-4

The pulse sequence for the zoom readout is shown graphically in Figure 2.10.

The simulations to examine the evolution of M_zb were performed in MATLAB for a heart-rate of 75 bpm. M_zb in the DIR and QIR sequences (with and without zoom imaging) was calculated over ten cardiac cycles at regular time intervals of 10 ms using equation 3.5 derived from the Bloch equations [65].

$$M_z(t) = M_z e^{-t/T_1}\cos(\alpha) + M_0(1 - e^{-t/T_1})$$

Equation 3-5

where T1 is the T1 relaxation constant, α is the flip angle and M_0 is the equilibrium magnetization. Simulations were performed assuming that the blood experiences a) only two non-selective inversion pulses and b) the two non-selective inversion pulses and the additional 90 º excitation pulse. A low-high phase order was assumed, meaning that the first echo in each heartbeat is used to fill the central lines of k-space. The value of M_zb at beginning of image acquisition was then plotted versus T1 for each heartbeat. This was used to examine the number of cardiac cycles required for M_zb to reach a steady state.

3.2.2 Phantom Studies

A T1 phantom which consisted of tubes containing gel samples made from agarose doped with Gadolinium, inserted in a holder filled with a copper sulphate solution was scanned using the DIR and QIR sequence on a 1.5 T Achieva clinical scanner (Philips Healthcare, Best, The Netherlands) using the body coil for both transmit and receive. To examine the signal characteristics of blood in the DIR and QIR

sequences, the slice selective pulses were removed and only the non-selective pulses were applied.

TR_{eff} was set to one RR interval for each simulated heart-rate. As in the simulations, the TI of the DIR sequence was set to null pre and post-contrast blood for each examined heart-rate. The heart-rate optimized TI1 and TI2 delays were used for the QIR sequence. Other imaging parameters included: spatial-resolution = 2 x 2 x10 mm and TR / TE = 10 ms /5 ms. A fast gradient echo (TFE) readout was used with a flip angle of 25 ° and a TFE factor of 1 to ensure that T2 effects could be assumed to be negligible and that the imaging sequence did not affect the signal characteristics. For each phantom image, a corresponding noise scan was acquired with RF and gradients of the imaging sequence switched off. The SNR for each sample was calculated using:

$$SNR = \frac{\mu_{image}}{\sqrt{(\mu_{background}{}^2 + \sigma_{background}{}^2)/2}}$$

Equation 3-6

where μ_{image} is the average signal intensity in a region of interest defined within each sample in the image and $\mu_{background}$ and $\sigma_{background}$ are respectively the average and standard deviation of the signal intensity in the same region of interest in the noise image [66]. The phantom was also scanned with no pre-pulses and the TR_{eff} set to five times the longest T_1 species (i.e. 5 x 1400 ms). The SNR measurements from this scan were then used to normalize the simulated $M_z b$ values to the fully relaxed magnetization in order to compare them with the measured SNR values.

3.2.3 QIR ECG-triggering

The clinical QIR pre-pulse was combined with two ECG-triggering methods; 'traditional' and 'trailing' ECG-triggering. In the traditional ECG-triggering approach (Figure 3.1a), the QIR pre-pulse was performed immediately after the R-wave followed by the imaging sequence. In an attempt to ensure adequate blood exchange during TI2 regardless of the patient's blood flow characteristics or the TI1 and TI2 delays, 'trailing' ECG-triggering (Figure 3.1b), performed the "second" DIR pre-pulse immediately after the R wave, followed by TI2 and the imaging sequence. A delay (T_{trail}) was then performed followed by the "first" DIR pre-pulse. In order to ensure that remaining time was equal to the TI1 delay, T_{trail} was calculated using:

$$T_{trail} = RR - TI_1 - TI_2 - T_{acq}$$

Equation 3-7

where RR is the subject's RR interval and T_{acq} is the acquisition time.

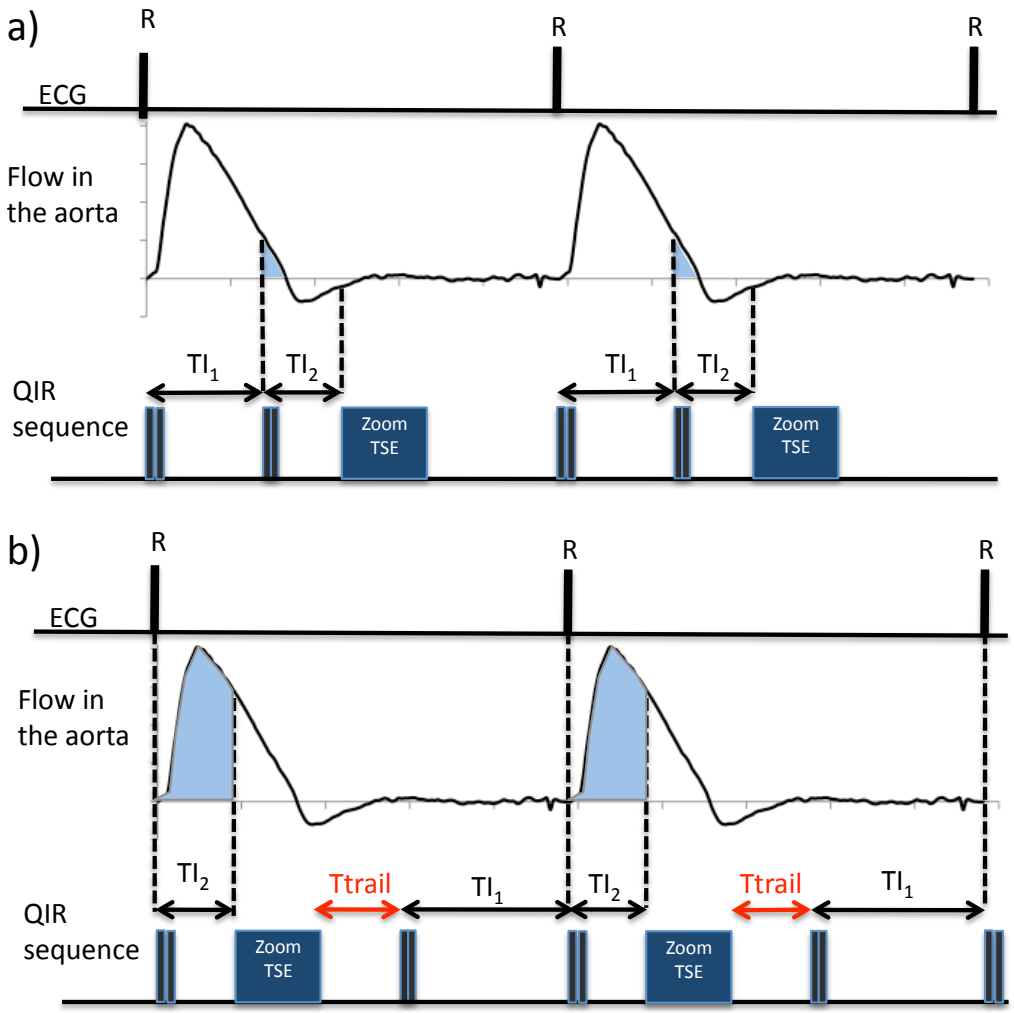

Figure 3-1: **The quadruple inversion pre-pulse sequence implemented with a) "traditional" ECG triggering and b) with "trailing" ECG-triggering resulting in different amounts of blood flow (blue area under the curve) during TI2.**

3.2.4 Volunteer Studies

Ten healthy subjects were imaged at 1.5 T using a 32-channel coil. This study was performed at 1.5 T as it was part of an existing study at this field strength. Firstly pre-contrast images were acquired of the abdominal aorta using a multi-slice DIR-TSE zoom scan. Imaging parameters included: 33 slices, slice thickness = 5 mm, inversion slice thickness = 8 mm, FOV = 79 x 201 mm, spatial resolution = 1 x 1 mm, TSE factor = 25, TE = 5 ms, FA = 90 °, low-high profile order, five start-up shots, two signal averages, shortest trigger delay. TR_{eff} was set to one heartbeat and

the TI was chosen to null blood using the Fleckenstein formula assuming a pre-contrast blood T_1 value of 1200 ms.

Five slices (with best vessel wall depiction on pre-contrast images) were then imaged with the DIR pre-pulse replaced by the QIR pre-pulse with heart-rate optimized TI1 and TI2 delays and all other imaging parameters maintained. QIR scans were performed firstly with "traditional" ECG-triggering (Figure 3.1a) and repeated with the "trailing" ECG-triggering method (as described in Figure 3.1b).

10-15 minutes after the injection of 0.2 mmol/kg of Gadovist (Bayer Schering AG, Berlin, Germany), the DIR-TSE scan was repeated in the same five slices. The TI was set first to the same TI from the pre-contrast DIR-TSE scan and repeated with the TI set according to a preceding Look locker scan. The QIR-TSE sequences were then performed in the same five slices with the two ECG-triggering methods and TI1 and TI2 maintained. The QIR-TSE scan was also repeated with the TR_{eff} set to the patient's average RR interval but with ECG triggering switched off. In seven patients, the post-contrast QIR-TSE sequence was also repeated without zoom imaging thereby acquiring the full FOV. To minimize aliasing artifacts fold-over suppression was enabled using external saturation bands. The acquisition time per slice was 11 heartbeats for the zoom DIR-TSE and zoom QIR-TSE sequences and 30 heartbeats for the full FOV QIR-TSE sequence. PC velocity encoded images with velocity encoding set to 150 cm/s were also acquired perpendicular to the abdominal aorta just above the bifurcation in each subject to estimate blood flow during TI2.

3.2.5 Image Analysis

Image analysis was performed on all images. The measurements were an average of those calculated in all five slices. The SNR of blood was measured in all the images of healthy volunteers using region of interest analysis performed in OsiriX© Medical Imaging Software (version 3.2.1, Los Angeles, California). Soapbubble software was used to the track the path of the vessel wall using edge detection algorithm and SNR of the vessel wall was calculated as the average signal intensity of the centerline divided by the standard deviation of the signal in a noise region. CNR between the vessel wall and blood (CNR(VW/blood)) was calculated as the difference between the vessel wall SNR and blood SNR. The vessel wall sharpness was calculated in percent by normalizing the magnitude of the local change in signal intensity at the selected vessel border to the average signal intensity of the centerline of the selected vessel using a Deriche algorithm [67].

3.2.6 Image Quality Scores

Image quality was assessed by two blinded, independent, experienced observers. The qualitative analysis of the vessel wall was graded for each image (the central slice) on a scale from 0 to 4 for the depiction of the aortic vessel wall: 0, vessel wall not visualized; 1, insufficient visualization of vessel wall; 2, sufficient visualization of vessel wall with significant artifact level; 3, good visualization of vessel wall with low artifact level; and 4, excellent image quality.

3.2.7 Statistical Analysis

Statistical analysis was performed to compare the quantitative measurements made in pre and post contrast sequences using firstly a one-way ANOVA comparison followed by a post-hoc Newman-Keuls paired t-test with a confidence interval of 95 %. The difference in image grading scores between the different sequences and

between the two observers were assessed by the Wilcoxon matched-paired signed rank test.

3.2.8 Flow Measurements

Region of interest analysis was performed on phase-contrast images using ViewForum software (Philips Healthcare, Best, NL) to plot the flow-rate versus time curves for each subject. The total blood exchange volume during TI2 was calculated for the two ECG-triggering methods by calculating the area under the curve during TI2 (see Figure 3.1). The total blood exchange volume (V) required during TI2 to achieve complete blood exchange was estimated using:

$$V = t.A$$

Equation 3-8

where A is the area of the aorta (2 cm^2 which was the average measurement from PC magnitude images in ten volunteers) and t is the inversion slice thickness which was set at 8 mm for the volunteer scans.

3.3 *Results*

3.3.1 Simulations and Phantom Studies

3.3.1.1 Optimization of the TI1 and TI2 Delays in the QIR sequence

The optimal TI1 and TI2 delays from simulations were plotted versus the TR_{eff} (equal to the RR interval) and a cubic equation was fitted to the curves. This equation was programmed in the scanner software to automatically predict the optimal TI1 and TI2 values according to the entered heart-rate (Figure 3.2).

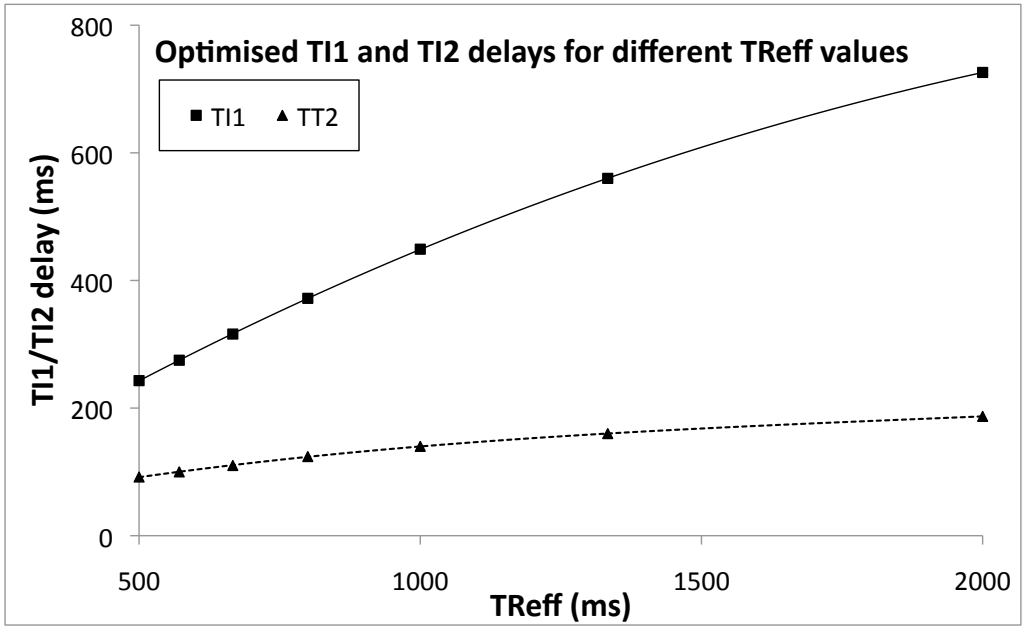

Figure 3-2: **Optimal TI1 TI2 times for the QIR sequence from simulations of the Bloch equations were plotted versus the TR_{eff} and fitted with a cubic equation.**

The simulated (lines) and measured (points) blood signal characteristics of the DIR sequence for different heart-rates for pre-contrast (Figure 3.3a) and post-contrast (Figure 3.3b) show that blood is only suppressed for one specific T1 value. The results for the QIR sequence (Figure 3.3c) show that in contrast to the DIR sequence, the signal is suppressed for all values of T1 greater than approximately 200 ms. There is a small variation in signal characteristics with heart-rate which indicate that the suppression of blood T1 values less than 200 ms is superior for higher heart-rates.

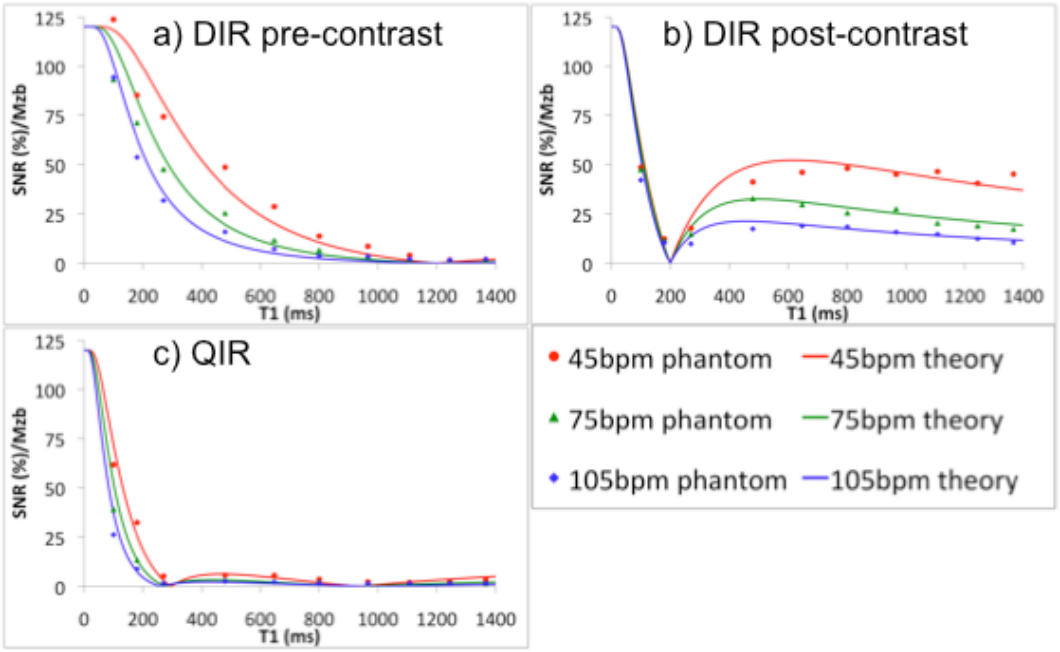

Figure 3-3: Blood signal characteristics for different heart-rates for a) the pre-contrast DIR with TI calculated to null T1 = 1200 ms, b) the post-contrast DIR with TI calculated to null T1 = 200 ms and (c) the QIR sequence with optimized TI1/TI2 = 560/160 ms for a heart-rate of 45 bpm, TI1/TI2 = 372/124 ms for a heart-rate of 75 bpm and TI1/TI2 = 275/100 ms for a heart-rate of 105 bpm. Normalized M_zb values from theoretical simulations (solid lines) and the SNR measurements from phantom experiments (points).

3.3.1.2 Simulation of the evolution of M_zb during the DIR and QIR sequences

The signal characteristics predicted by equations 2.5 and 2.6 and shown in Figure 3.3 assume that a steady-state has been reached between heartbeats. Simulations using the Bloch equations were used to examine the evolution of M_zb for blood with a T1 of 100, 200, 700 and 1200 ms during the first ten heartbeats of the sequence for a heart-rate of 75 bpm. The pre-contrast DIR sequence employs a TI to null blood with a T1 of 1200 ms. It is only by the 6th heart-beat when the M_zb for blood with a T1 of 1200 ms crosses the zero point at the time of imaging (Figure 3.4a). These simulations were also used to calculate the M_zb value at the time of imaging for each T1 species between 1 and 1400 ms (Figure 3.4b), which indicate that it takes approximately 10 heartbeats to reach a steady-state for all T1 values but that an approximate steady-state is reach by the 6th heartbeat.

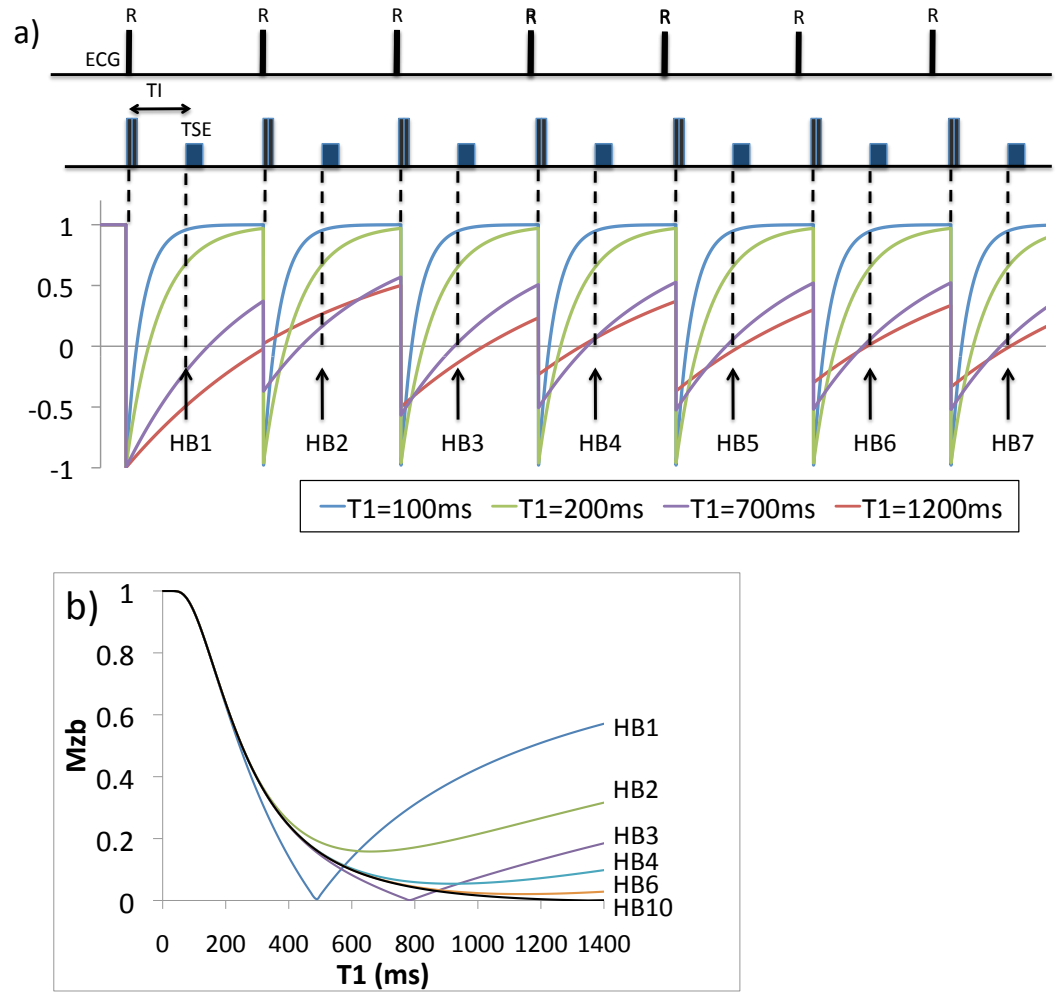

Figure 3-4: a) The evolution of M_zb during the pre-contrast DIR sequence with TI set to 335 ms in order to null a T1 value of 1200 ms for T1 of 100, 200, 700 and 1200 ms and a heart-rate of 75 bpm and b) M_zb versus T1 plots for each heartbeat.

The equivalent results for the post-contrast DIR sequence show that the M_zb for a T1 of 200 ms is nulled from the first heartbeat (Figure 3.5a). It still takes 6 heartbeats to reach an approximate steady-state for all T1 species (Figure 3.5b).

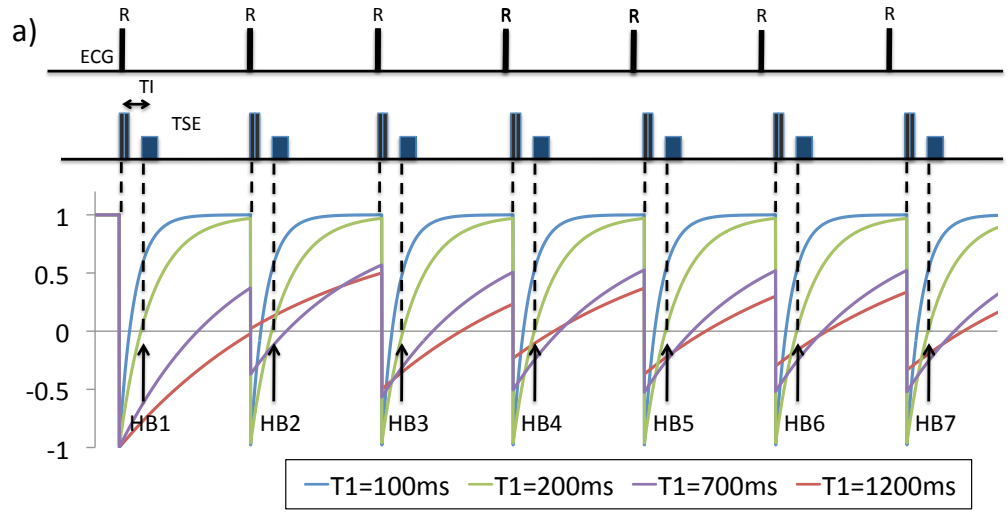

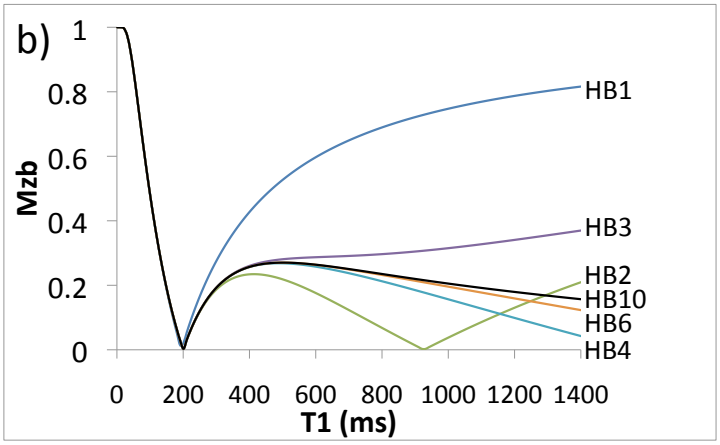

Figure 3-5: a) The evolution of M_zb during the post-contrast DIR sequence with TI set to 135 ms in order to null a T1 value of 200 ms for T1 of 100, 200, 700 and 1200 ms and a heart-rate of 75 bpm and b) M_zb versus T1 plots for each heartbeat.

The results for the QIR sequence show that by the sixth heartbeat, the Mzb for a T1 of 200, 700and 1200 ms are all nulled at the time of imaging (Figure 3.6a). Again it takes 6 heartbeats for longer T1 species to reach an approximate steady state (Figure 3.6b).

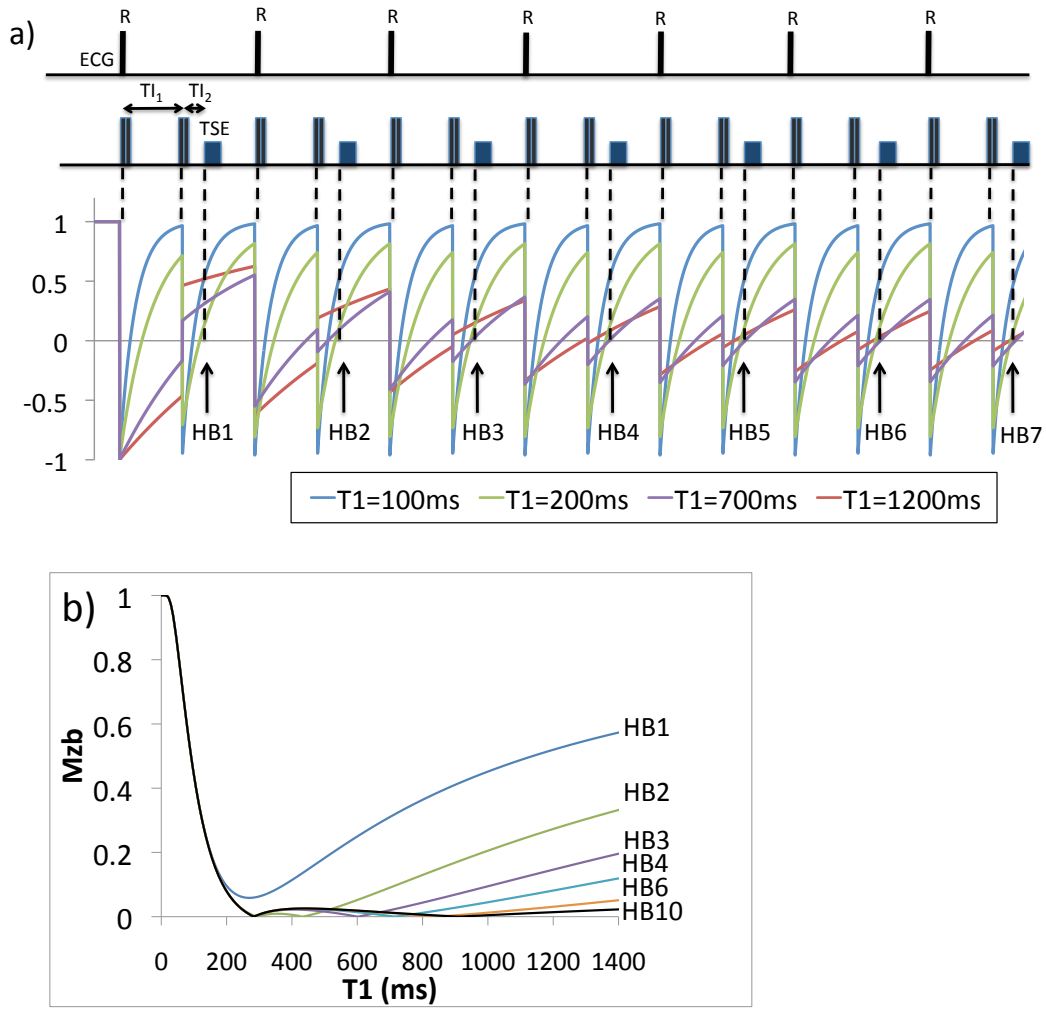

Figure 3-6: a) The evolution of Mzb during the QIR sequence with TI1/TI2 set to 372/124 ms for T1 of 100, 200, 700 and 1200 ms and a heart-rate of 75 bpm and b) Mzb versus T1 plots for each heartbeat.

It is important to ensure that the M_zb has reached a steady-state between heartbeats as a modulation of the signal can cause ghosting artifacts. It was therefore decided to use five start-up shots in all the volunteer studies (i.e. data acquired in the first five cardiac cycles were disregarded and not used for image reconstruction).

When the DIR and QIR sequences are combined with a zoom readout, it is possible that the inflowing blood has also experienced the 90 ° excitation pulse which is

applied with the phase encoding gradient. Simulations which included the 90 º excitation pulse showed that as M_zb is brought into the transverse plane, the blood signal is completely suppressed for nearly all T1 values. Depending on the orientation of the imaging slice and phase encoding gradient, the patient anatomy and amount of blood flow in each cardiac cycle, the blood within the imaging slice may have experienced the inversion pulses with or without the additional 90º excitation pulse. It cannot be predicted whether the blood has experienced the 90º excitation pulse from previous heartbeats on an individual patient basis. In this study, the QIR delays were therefore optimized assuming that the blood only experiences the inversion pulses. Five start-up shots were employed in all studies to ensure a steady state had been reached between heartbeats.

3.3.2 Volunteer Studies

The zoom read-out allowed a reduced FOV to be imaged in a shorter time without fold-over artifacts (Figure 3.7). The ratio of the vessel wall SNR in the zoomed images to that in the full FOV images was 0.64 ± 0.09. This is in good agreement with the expected ratio of the square root of the total sampling time of 0.6 for the zoomed and full FOV images. There was also a significantly higher blood SNR, CNR(VW/blood) and vessel wall sharpness in the full FOV images compared to the image acquired with zoom imaging ($p<0.05$) but no significant difference in the image quality scores.

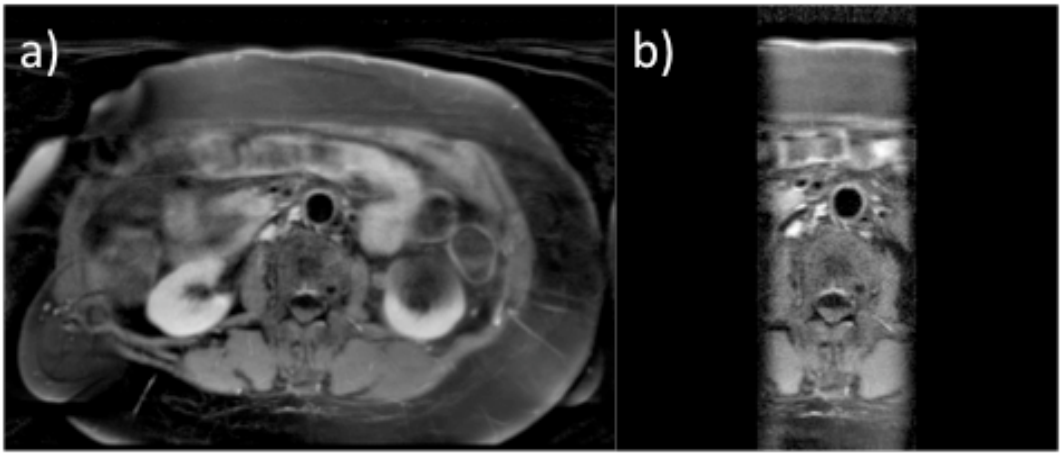

Figure 3-7: Post-contrast images using the QIR pre-pulse and trailing ECG-triggering with a) full FOV imaging (320 x 220 mm) and fold-over suppression and b) a reduced FOV (79 x 220 mm) zoom imaging.

The heart-rates in volunteers ranged between 55 and 90 bpm. The TI values used in the post-contrast DIR ranged from 130 to 160 ms and the T1 values for the blood calculated from the Look Locker scans were between 278 and 385 ms. When using the DIR pre-pulse the TI value had to be shortened in order to achieve adequate blood suppression after contrast administration (Figures 3.8a, 3.8d and 3.8e). In comparison, the QIR pre-pulse allowed imaging to be performed pre and post contrast using identical pre-pulse parameters. When the QIR pre-pulse was combined with "traditional" ECG-triggering, there was suboptimal blood suppression (Figures 3.8b and 3.8f). This is particularly important as incomplete blood exchange due to slow flow near the vessel wall could mimic vessel wall enhancement. There was however consistently good blood suppression in all volunteers using the QIR sequence with "trailing" ECG-triggering (Figures 3.8c and 3.8g). The trailing ECG-triggering approach also resulted in superior blood suppression compared to un-triggered QIR-TSE scans (Figure 3.8h).

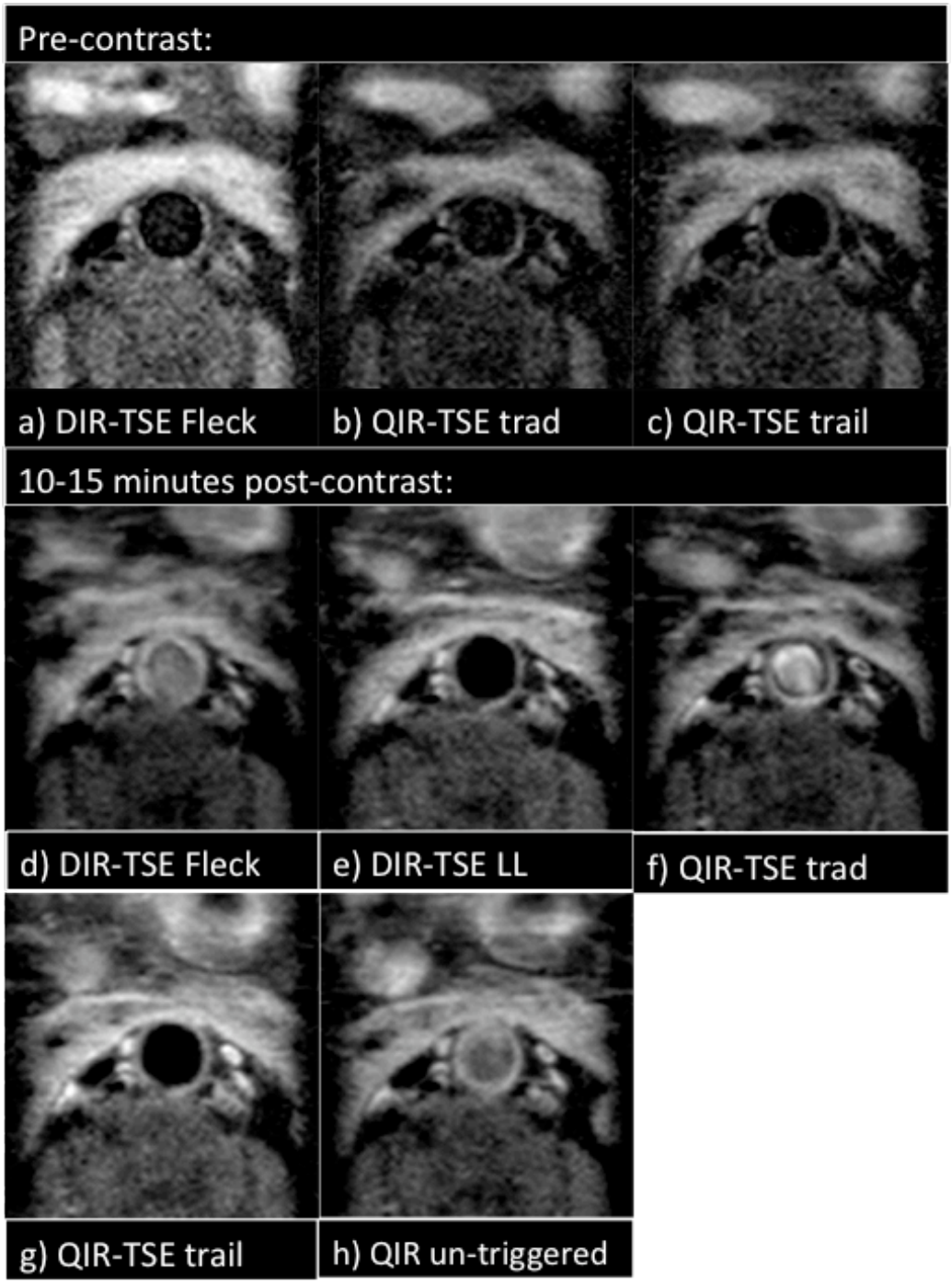

Figure 3-8: Volunteer images (heart-rate = 75 bpm) through the abdominal aorta. Pre-contrast scans: a) DIR-TSE with TI set using the Fleckenstein formula, b) QIR-TSE with "traditional" ECG triggering, c) QIR-TSE with "trailing" ECG triggering and post-contrast scans d) DIR-TSE with TI set using the Fleckenstein formula, e) DIR-TSE with TI set using a preceding Look Locker, f) QIR-TSE with "traditional" ECG triggering, g) QIR-TSE with "trailing" ECG triggering and h) QIR-TSE without ECG triggering.

3.3.3 Flow Measurements

The total blood exchange volume during TI2 measured from PC imaging for the two triggering techniques shows that the inferior QIR blood suppression using the traditional ECG-triggering is caused by insufficient blood exchange during TI2 (Figure 3.9). These results also indicate that the inversion slice thickness could be as much as doubled and there would still be sufficient blood exchange within TI2 to achieve adequate blood suppression when using the trailing ECG-triggering technique.

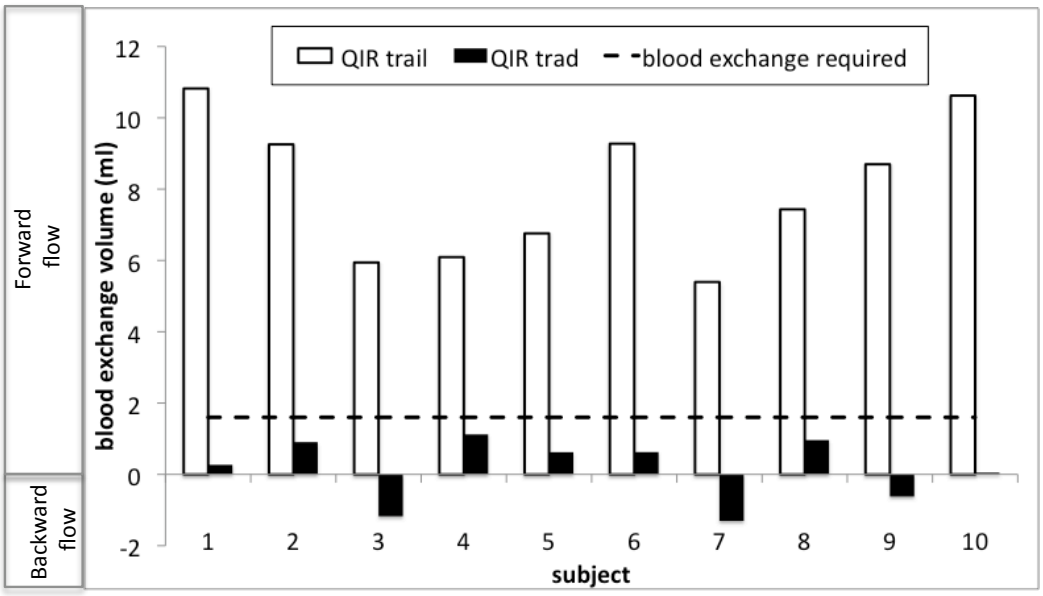

Figure 3-9: **The total blood exchange volume during TI2 measured from PC imaging for the QIR sequence using the two ECG triggering methods. The dotted line indicates the total blood exchange volume required during TI2 for an inversion slice thickness of 8 mm.**

3.3.4 Image Analysis and Image Quality Scores

There was no significant difference found between the image quality scores given by the two observers. The image analysis and image quality scores are displayed in Figure 3.10. There was no significant difference in pre-contrast blood SNR or CNR(VW/blood) between sequences. The pre-contrast vessel wall SNR, vessel wall sharpness and image quality scores were however higher with the DIR sequence ($p<0.05$) compared to the QIR technique using “trailing” ECG-triggering. There

were no significant differences between the QIR sequences with the two different triggering methods when imaging before contrast.

Post-contrast, the DIR-TSE sequence with TI adjusted using a preceding Look Locker had improved blood SNR, CNR(VW/blood), vessel wall sharpness and image quality scores compared with the DIR-TSE sequence which used the same TI as pre-contrast scans ($p<0.05$). Post-contrast, the QIR technique using "trailing" ECG-triggering had significantly lower blood SNR, higher CNR(VW/blood), improved vessel wall sharpness and image quality scores compared to the un-triggered and the "traditional" ECG-triggered QIR scans ($p<0.05$).

There was no significant difference in the blood SNR, vessel wall SNR, CNR(VW/blood) or image quality measurements between the post-contrast DIR-TSE with TI adjusted using a preceding Look Locker and the QIR scans using the "trailing" ECG-triggering method. Vessel wall sharpness was significantly higher in the QIR scans using the "trailing" ECG-triggering method compared to the DIR-TSE with TI adjusted using a preceding Look Locker ($p<0.05$).

The percentage contrast enhancement was calculated as the difference between the post-contrast and pre-contrast CNR(VW/blood). The enhancement values for the DIR with TI adjusted using a preceding Look Locker and for the QIR with trailing ECG-triggering were 231 ± 66 % and 237 ± 125 % respectively with no significant difference found.

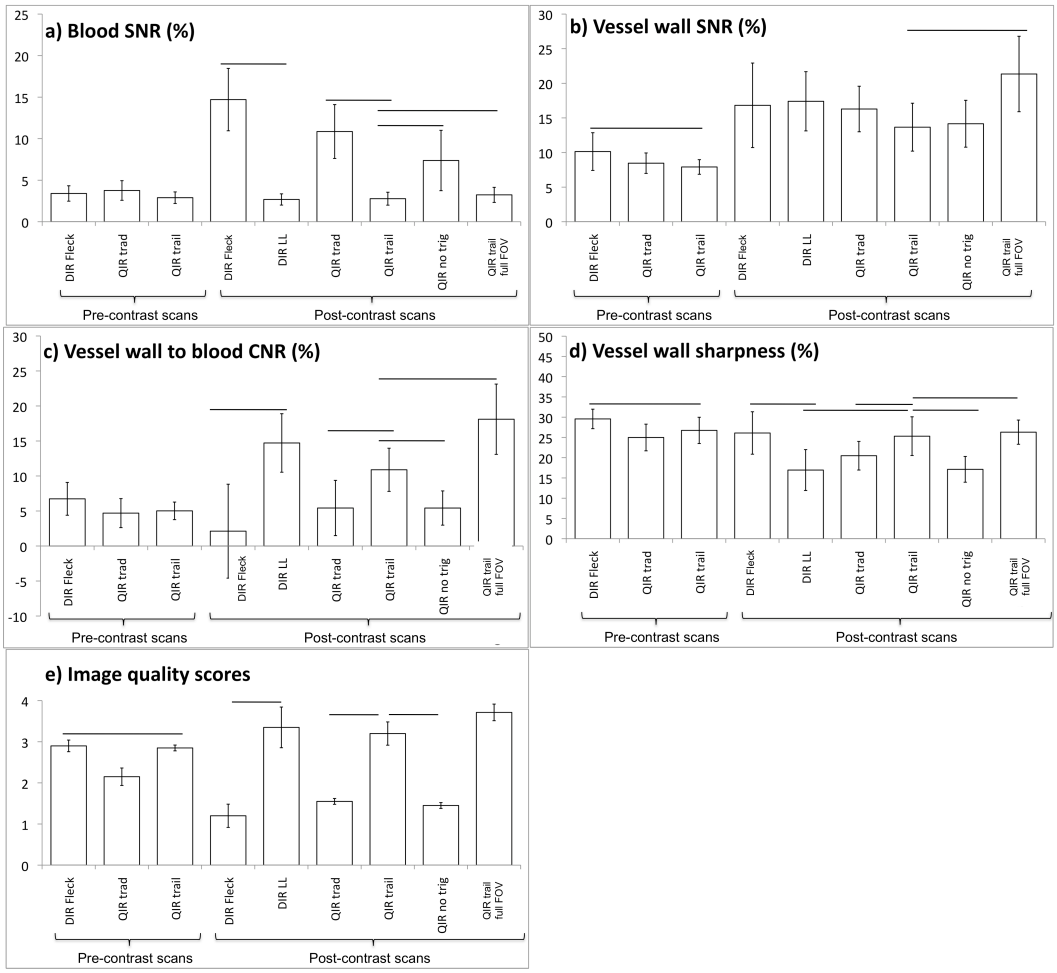

Figure 3-10: **a) Blood SNR measurements, b) vessel wall SNR, c) vessel wall to blood CNR measurements, d) vessel wall sharpness measurements and e) image quality scores for each acquisition. N.B. All measurements were made on ten volunteers except the post-contrast QIR full FOV measurements which were based on seven volunteers. The bars indicate a statistically significant difference between measurements according to a one-way ANOVA comparison followed by a post-hoc Newman-Keuls paired t-test with a confidence interval of 95 %.**

3.4 *Discussion*

In this study I have shown that the QIR sequence can be successfully combined with zoom imaging to achieve a reduced FOV resulting in a shorter scan-time. In the DIR-TSE sequence, it is mandatory to adjust the TI value after contrast administration to achieve adequate blood suppression. This requires a Look Locker scan to determine the optimum TI value which adds additional scan time. This limits the use of DIR-TSE for long acquisitions where the TI may change during image

acquisition. I have implemented a QIR-TSE sequence with “trailing” ECG-triggering, which achieved consistently good blood suppression by ensuring that the TI2 delay coincides with maximum systolic flow. This sequence does not require a Look Locker scan and can be applied together with long multi-slice acquisitions without the need of adapting the inversion times.

Limitations include the fact that the volunteers studied had relatively little variation in heart-rate. In patients with variable heart-rates, arrhythmia rejection may be useful in ensuring that the optimized QIR delays are correctly calculated from the average RR interval in equation 3.7. Future studies should also investigate whether the QIR sequence improves the visualization of vessel wall enhancement in patients with atherosclerosis. Furthermore, I could evaluate the QIR technique in patients who are undergoing endarterectomy where plaque is surgically removed from the aorta to assess whether the enhancement is more closely related to the degree of fibrosis measured in the tissue samples.

In conclusion, ECG triggering with a “trailing” TI1 delay was found to be vital when applying the QIR sequence to vessels, which are subject to motion and/or variable blood flow during the cardiac cycle.

Chapter 4

4. Review of LGE MRI Techniques for Myocardial Infarction

4.1 *Introduction*

MRI using LGE is the gold standard non-invasive method to measure MI. It is arguably this MR technique which has led to the widespread clinical use of cardiac MRI over the last decade. Its superior spatial resolution compared with single photon emission computed tomography (SPECT) enables more accurate measurement of the extent and transmurality of infarction which are crucial for the clinical management of patients with MI [18].

LGE imaging is based on the delayed washout of Gadolinium contrast agent from infarcted myocardium compared with healthy myocardium. At 10-30 minutes after contrast administration, areas of infarction appear hyperintense on T1-weighted images. The IR-TFE technique is the most widely used MR-LGE sequence as it maximizes the contrast between infarcted and normal myocardium [32]. A number of research studies have investigated the optimal sequence parameters, contrast agent, contrast dose and timing for the IR-TFE approach. Alternative LGE sequences such as PSIR imaging and T1 mapping have also been investigated.

Although IR-TFE, PSIR and T1 mapping techniques achieve high contrast between infarcted and uninfarcted myocardium, they can exhibit low contrast between infarct and blood. This can make it difficult to identify small subendocardial infarcts and accurately measure transmurality. There have been various strategies developed to improve the differentiation of infarcted myocardium from blood. This chapter presents a summary of this research and identifies the key strengths and drawbacks of each approach.

4.2 *Current Clinical Practice*

4.2.1 Inversion Recovery Sequence

Simonetti et al (2001) compared ten MR sequences in dogs with induced chronic myocardial infarction and examined image contrast, signal difference between infarcted and normal myocardium ($SD_{inf\text{-}myo}$), SNR, imaging time and the motion sensitivity of each technique [32]. The sequences included the segmented IR-TFE sequence, the T2-weighted turbo spin echo (TSE) sequence with and without an IR pre-pulse and a T1 weighted TSE with and without an IR pre-pulse. All sequences had the same spatial resolution. The post-contrast T1 weighted imaging was found to be more sensitive than non-contrast T2-weighted techniques and that GE read-out was superior to TSE readout. Overall the segmented IR-TFE images produced highest $SD_{inf\text{-}myo}$.

The IR-TFE technique (Figure 4.1), employs a 180 ° inversion RF pulse after the R-wave. Image acquisition is then performed at a certain time delay (TI) after this inversion pulse. To reduce motion artifacts, ECG-triggering is employed to time image acquisition with mid-diastole when there is least cardiac motion. To reduce respiratory artifacts, breath-holding is performed. K-space segmentation is used rather than a single-shot approach which requires a long acquisition window and has been found to cause motion artifacts. A single shot approach also tends to drive the magnetization into a steady-state during the acquisition period and $SD_{inf\text{-}myo}$ is reduced. By segmenting the acquisition, fewer phase encoding steps are performed and so the main determinate of image contrast is the IR pre-pulse. A low flip angle between 20 and 30 ° is employed to minimize the effect of the read-out on the signal characteristics. Imaging is performed every two heartbeats (TR_{eff} = 2 heartbeats) to allow for T1 recovery between data acquisitions.

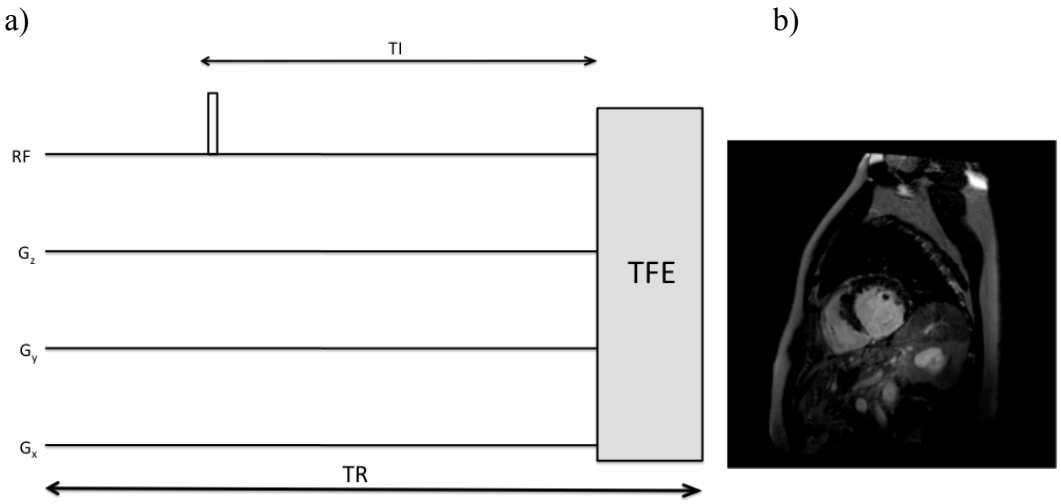

Figure 4-1: a) IR-TFE imaging sequence and b) an example LGE image of a patient with MI.

4.2.2 The Importance of Choosing the Correct Inversion Time

Gupta et al (2004) investigated the optimization of TI times for LGE imaging. It was found that relative signal intensity between infarcted and normal myocardium ($SI_{inf-myo}$) is determined largely by the precise timing of the image acquisition at the null point of normal myocardium [68]. In this study, the optimal TI was measured in 17 patients 10-15 minutes after administration of 0.15 mmol/kg of Magnevist using a T1 mapping technique. The patients then underwent IR-TFE imaging. It was found that $SI_{inf-myo}$ in IR-TFE images varies considerably with the choice of TI (Figure 4.2). The peak at TI_0 corresponds to the null point of normal myocardium. There is a sharp drop in $SI_{inf-myo}$ for TI values less than TI_0 which indicates that an underestimation of TI severely affects the contrast. There is a more gradual but nonetheless significant drop at higher TI values. In this study, the optimal TI was found to range from 180 to 315 ms. The optimal TI can also vary widely with contrast dose and time after contrast administration as well as patient specific factors such as patient weight and cardiac and renal function [68]. TI must therefore be determined separately for each patient.

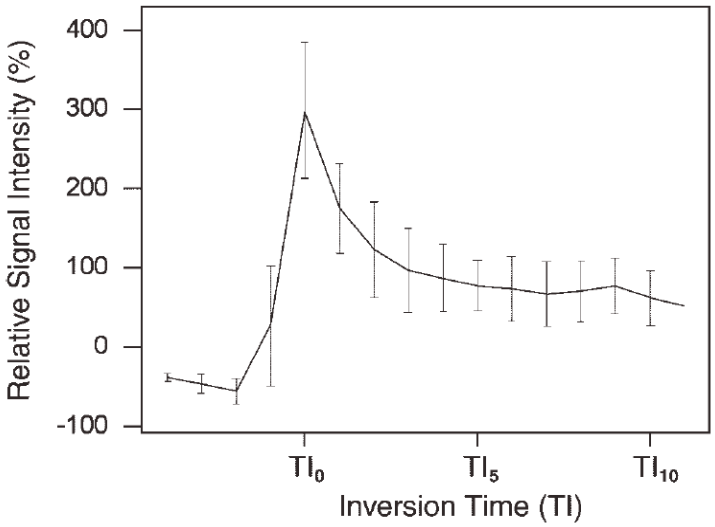

Figure 4-2: Relative signal intensity of infarcted to uninfarcted myocardium for varying TI values [68].

4.2.3 Look Locker Scans

TI_0 is normally determined by performing a Look Locker scan just prior to the IR-TFE sequence. As described in chapter 3, the Look Locker sequence is used to acquire images each with a different TI value [28]. Each image has different signal intensity in the myocardium, infarct and blood (Figure 4.3a). TI_0 can be estimated by choosing the image in which the myocardium signal is most suppressed. Alternatively the signal intensity in a region of interest (ROI) in the viable myocardium can be plotted as a function of TI where TI_0 corresponds to the x-intercept of this graph (Figure 4.3b).

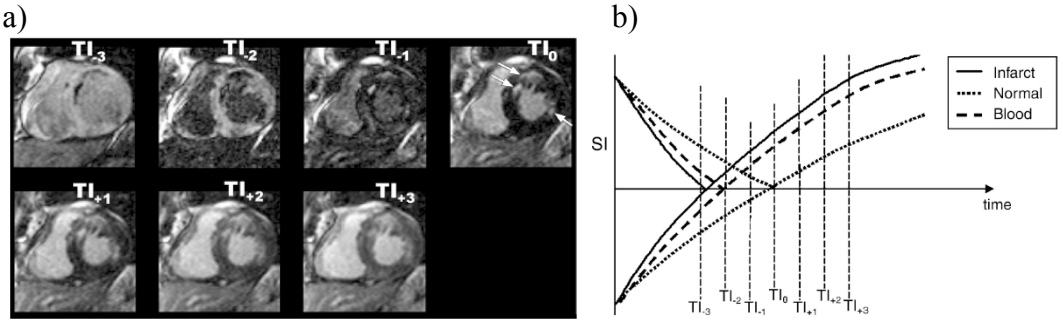

Figure 4-3: a) IR-TFE images at selected TI values showing the change in image contrast with TI and b) plot of signal intensity for infarcted myocardium, uninfarcted myocardium and blood in the IR sequence using different TI values [68].

4.2.4 Gadolinium Contrast Agents used for LGE Imaging

There are several factors which influence the choice of contrast agent, dose and timing of image acquisition. These include the licensing and cost of the agent as well as its physical properties which affect safety and image quality. As there is currently no consensus on the optimum contrast agent, dose or timing of LGE imaging, this section will examine the current research and guidelines for clinical practice.

Although highly toxic as a free ion, when gadolinium is bound to an organic compound, it is generally regarded as safe for use as a MRI contrast agent [69]. The properties of the different contrast agents used for LGE imaging are summarized in Table 4.1. Contrast agents can be categorized on the basis of the biochemical structure of the chelates used to bind the gadolinium ion as either 'macrocyclic' or 'linear' (Figure 4.4) [70]. Each contrast agent also has a property known as 'relaxivity' (r_1). The relaxivity of a tissue after contrast administration (R_1) can be calculated as:

$$R_1 = R_{T1} + r_1 \cdot C$$

Equation 4-1

where R_{T1} is the relaxivity of the tissue before contrast administration and C is the concentration of administered contrast agent present in the tissue. The T1 of the myocardium after contrast administration can then be calculated as:

$$T_1 = 1/R_1$$

Equation 4-2

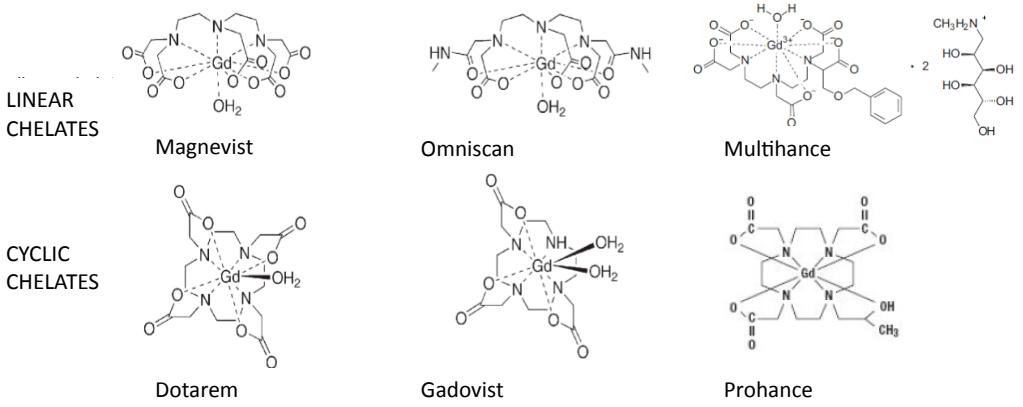

Figure 4-4: Contrast agents can be categorized on the basis of the biochemical structure of the chelates used to bind the gadolinium ion as either 'macrocyclic' or 'linear' [71].

Biochemical structure	**Trade name**	**Generic Name**	**Relaxivity** (mM-1s-1)
LINEAR CHELATES	Magnevist	Gadopentetate dimeglumine	r1 = 5.3 (2T)
	Omniscan	Gadodiamide	r1 = 3.9 (1T)
	MultiHance	Gadobenate Dimeglumine	r1 = 8.1 (1.5 T)
CYCLIC CHELATES	Dotarem	Gadoterate meglumine	r1 = 3.4 (1T)
	Gadovist	Gadobutrol	r1 = 6.1 (2T)
	ProHance	Gadoteridol	r1 = 3.7 (1T)

Table 4-1: Contrast agents used in LGE imaging of MI and their properties [69, 70, 72].

4.2.5 Nephrogenic Systemic Fibrosis

Nephrogenic Systemic Fibrosis (NSF) is a severely disabling systemic fibrosing condition associated with increased morbidity and mortality. It was first linked with Gadolinium contrast agents in 2006 [73]. A causal relationship is yet to be proven and there are thought to be a number of additional risk factors. It is also extremely rare and has only been reported in patients with impaired renal function [69]. One theory proposes that the decreased clearance rate in these patients can allow other cations to displace gadolinium from its chelate, releasing free gadolinium which is then deposited in various tissues [69]. However, this has not been clinically proven and the pathogenesis of NSF is yet to be established.

NSF has been most commonly linked to linear chelates. Most reports are for Omniscan, followed by Magnevist with fewer reports for the macrocyclic agent, Prohance [74-76]. This appears to support the theory that macrocyclic chelates tend to bind more tightly to gadolinium chelates compared with linear chelates but it may also be because Ominscan has more often been administered in high doses [77]. Despite the ongoing controversy surrounding NSF and its association with different contrast agents, the European Committee for Medicinal Products for Human Use (C.H.M.P.) recently issued advice on Gadolinium contrast agents [78]. They have contraindicated the use of high risk gadolinium contrast agents in patients with severe renal impairment, patients in the perioperative liver-transplantation period and in neonates. They have categorized contrast agents into the following three groups according to risk:

- High risk - Omniscan, OptiMARK, Magnevist
- Medium risk - MultiHance, Primovist, Vasovist
- Low risk - Gadovist, ProHance, Dotarem

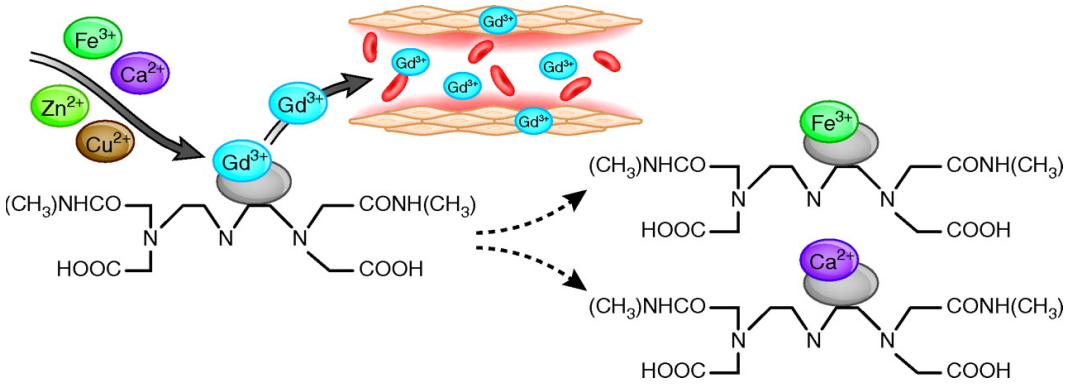

Figure 4-5: A non-ionic linear chelate (gadodiamide) which binds gadolinium less tightly than other chelates (macrocyclic and ionic), is shown undergoing the process of transmetallation. Other endogenous cations such as copper, iron, Zinc and calcium compete with gadolinium for chelate binding, allowing free gadolinium to be released into the circulation where it may bind other anions such as phospate and uremic organic anions [79].

Before the first description of NSF, clinical LGE studies were regularly performed with Magnevist and Omniscan using a double dose (0.2 mmol/kg patient body

weight). Although the NSF guidelines contraindicate these agents only in specific patient groups, in practice most clinical studies are now performed with 'low risk' agents. However, research studies are still performed with medium and high risk agents. Studies have been performed to compare the image quality when using low and medium risk agents with that achieved with Magnevist and Ominscan. As contrast agents have different relaxivity and binding, these studies have also investigated the optimum dose and image timing.

4.2.6 Dose of Contrast Agent Used for LGE

The signal intensity of the myocardium, infarct, blood and other tissues in the IR sequence will be dependent on their T1 values at the time of image acquisition. Equations 4.1 and 4.2 show that the T1 value is affected by the relaxivity of the contrast agent and the concentration present in the tissue. For example Multihance has almost double the relaxivity of Magnevist (Table 4.1). Schlosser at al (2005) found that a double dose of Multihance produced images with higher $CNR_{inf\text{-}myo}$ than a double dose of Magnevist but also resulted in an increased blood SNR [80]. Subsequent studies compared LGE imaging using a double dose of Magnevist and using a single dose (0.1 mmol/kg) of Multihance. In LGE images taken at 10 minutes, Bauner et al (2009), found higher $CNR_{inf\text{-}myo}$ with a single dose of Multihance and no significant difference in $CNR_{inf\text{-}blood}$ compared with a double dose of Magnevist [81]. There was however a significant increase in blood SNR with Multihance. In images taken at 15 minutes, Balci et al (2006), found no difference in $CNR_{inf\text{-}myo}$ or relative $SI_{inf\text{-}blood}$ [82].

Papini et al (2010) found that a single dose of Multihance was also found to produce higher $CNR_{inf\text{-}myo}$ compared to a single dose of Dotarem [83]. Although there was a higher blood signal in Multihance images, there was no significant difference in $CNR_{inf\text{-}blood}$ between the two contrast agents.

Although Multihance produces high $CNR_{inf\text{-}myo}$, it binds weakly to albumin [69] which means it remains in the blood pool for longer and has a higher relaxivity upon binding. Imaging later after contrast administration may reduce blood signal but can also reduce patient throughput. Although few cases of NSF have been reported with

Multihance, it is a linear chelate and is therefore categorized as medium risk. This means that Multihance is not widely used in the UK for LGE imaging.

Gadovist is now commonly used in the UK. It is a macrocyclic agent and is categorized as low risk. There is limited published work on the optimum dose of Gadovist for LGE imaging. A recent study in 20 patients compared Gadovist at a single dose and Magnevist at a double dose found no difference in total volume of myocardium, percentage of myocardial wall involvement, SNR and CNR [84]. However, the relaxivity of Gadovist is only slightly higher than Magnevist so a single dose may not produce sufficient signal intensity in the infarct. The current SCMR guidelines recommend a dose of Gadovist between 0.1 and 0.2 mmol/kg for LGE imaging [85].

4.2.7 Timing of LGE Imaging after Contrast Administration

The late enhancement effect is due to the higher signal in infarcted compared to normal myocardium. There is higher gadolinium concentration in infarcted myocardium partly because the contrast agent volume of distribution (V_d) is higher in infarcted myocardium [86]. There are also differences in wash-in and wash-out rates between infarcted and normal myocardium. It is thought to be a combination of these two phenomena which results in the late enhancement effect. As the concentration of Gadolinium in different tissues changes after administration, the T1 values of infarct, myocardium and blood will also vary with time after contrast administration and these will in turn affect the signal characteristics of IR images.

Goldfarb et al (2009) studied the T1 values of tissues in 25 patients with chronic MI after the administration of a double dose of Omniscan [87]. Imaging was performed with an inversion pulse followed by a series of balanced steady state free precession (bSSFP) readouts per breath hold. These images were acquired approximately every two minutes after contrast administration. The T1 values of blood pool, healthy myocardium and areas of infarction were calculated every minute using interpolation. The time course of the average T1 data (Figure 4.6) shows that the difference between infarct and viable myocardium and between infarct and blood both increase with time. It appears that blood and infarct have different T1 values as early as 8 minutes. However, the dotted lines which correspond to 1 standard

deviation for the 25 subjects show that the T1 values vary considerably between patients.

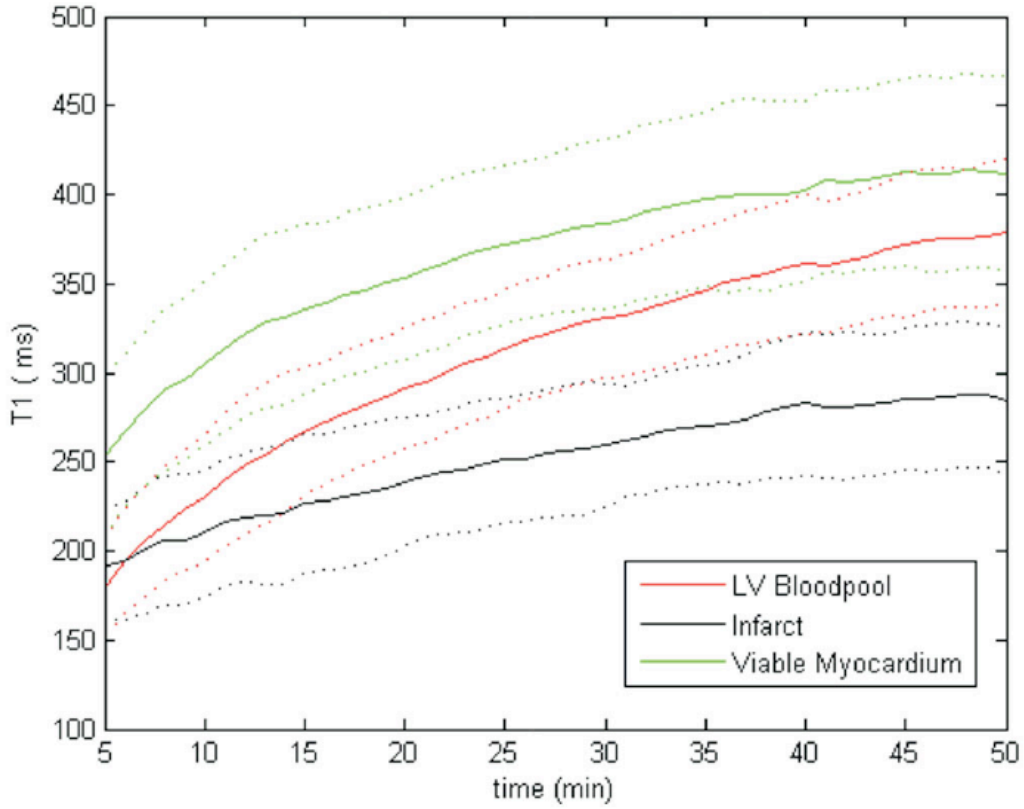

Figure 4-6: Average T1 values after a double dose of Omniscan for 25 subjects with chronic MIs

Similar data from Klein et (2004) using a double dose of Magnevist show that although scar and blood T1 values are significantly different at all time points after contrast administration, scar and blood T1 values are not significantly different between 5 and 15 minutes after contrast (Figure 4.7) [86].

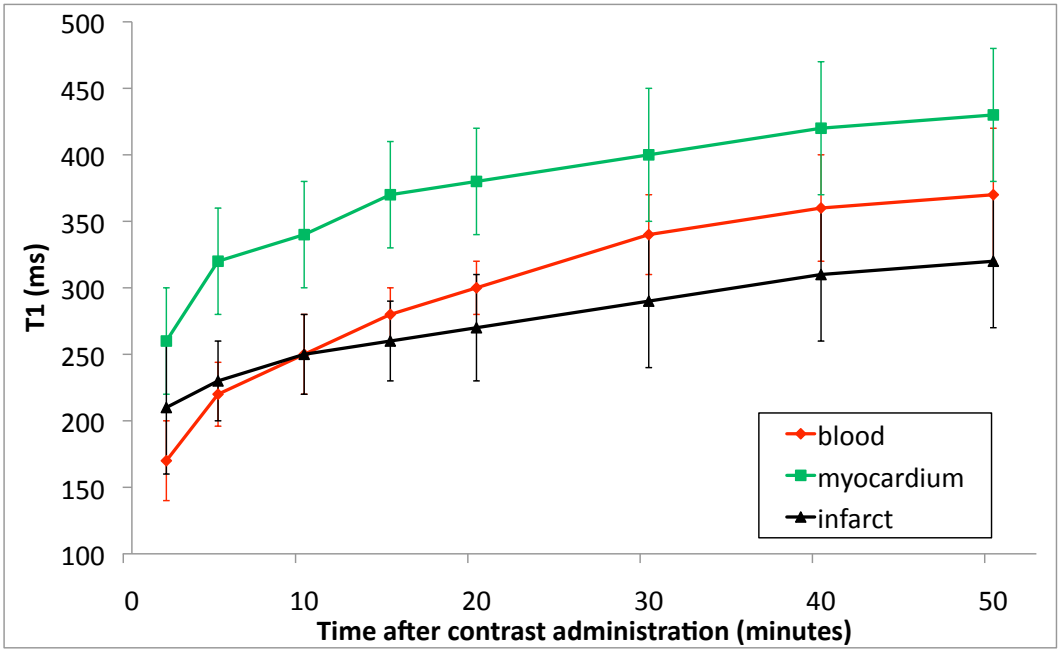

Figure 4-7: Average T1 values after a double dose of Magnevist for 11 subjects with chronic MI (adapted from [86])

The above studies both used the Look Locker technique to calculate T1 values and are therefore limited by the accuracy of this technique. There appears to be a wide variation of T1 values between different patients so the standard deviation of the measurements is quite high. It appears that blood has a higher T1 value than infarct as early as 10 minutes but this was not found to be significant.

The magnetic field strength causes the T1 values in most tissues to change. Sharma et al (2006) compared blood and myocardium T1 values with Ominscan at 1.5 T and 3.0 T [47]. They found that the T1 is significantly longer for myocardium (but not blood) at 3.0 T compared to 1.5 T. The differences in T1 due to field strength are reduced following contrast administration.

All the extracellular agents have a similar pharmacokinetics with the exception of Multihance which binds slightly to albumin. Therefore, although many of the above studies relate to 'high risk' contrast agents which are no longer routinely used, it is useful to examine the changes in T1 of different tissues with time after contrast administration. Although the pharmacokinetics are similar in low risk agents, the

relaxivity of the agent and field strength of the MRI scanner will also affect the T1 values of tissues [47].

4.2.8 Scar Quantification

There are several approaches to scar quantification on IR images. The scar can be outlined manually by the user. There have also been several computerized approaches applied to the problem of scar quantification (Figure 4.8). These approaches start with the outlining of the epicardial and endocardial borders to exclude the blood pool and isolate the myocardium. The 'standard deviation method' requires the user to define a region of interest in the remote myocardium. The scar is then defined as the pixels with a signal intensity greater than 2, 3, 4, 5 or 6 times the standard deviation of the signal in this region [32, 88, 89]. In the 'FWHM method' the scar ROI is either defined by the user in the hyperintense myocardium [90] or is automatically calculated as a region which has the maximum signal intensity in 10 contiguous pixels [91].The scar is then defined as all pixels with a signal intensity at least half this maximum value.

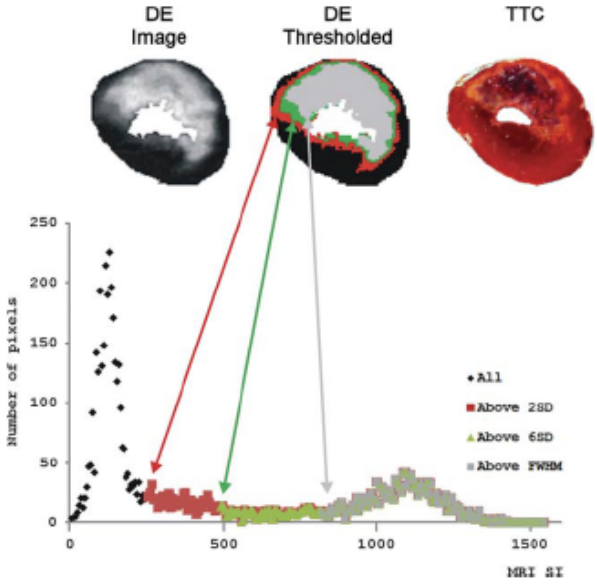

Figure 4-8: Histogram of the number of pixels with different signal intensities and the FWHM and standard deviation thresholding methods for scar quantification [91].

Amado et al (2004) compared the standard deviation, FHWM and manual contouring approaches to TTC histological staining in a canine model of MI [92]. They found that the FWHM method was most accurate compared to both the

standard deviation and manual contouring approaches. They found that FWHM technique was also more reproducible than manual contouring. Simor et al (2010) also found that the FWHM technique was more accurate than the standard deviation technique when compared with histological staining [91]. Flett et al (2011) performed a study in patients and found that the FWHM technique produced similar results to manual contouring and is statistically more reproducible than manual contouring or the standard deviation technique [93].

The inaccuracy of the standard deviation method could be due to the signal intensity variation at different locations in the normal myocardium due to the different distances from the receiver coil. Therefore the threshold can vary with the choice of the region of interest in the remote myocardium. The FWHM method always takes the highest intensity pixels in the infarct and therefore should be less affected by the distance from the receiver coil as only a relatively small ROI is evaluated depending on infarct size. Although manual contouring has higher inter-observer variability, it has been shown that it is useful for a reader to perform adjustments to the computer detected regions to exclude blood pool and regions of microvascular obstruction [94, 95].

4.3 *Alternative Sequences for LGE Imaging*

4.3.1 PSIR Sequence

The image contrast achieved using the IR sequence is sensitive to the choice of TI time. In clinical practice, 8 to 12 slices are acquired in a short-axis stack each requiring a separate breath-hold. As the T1 value of the normal myocardium increases with time after contrast administration, the optimal TI also changes. This means that the TI used to image slices at the end of the stack may no longer be optimal. As shown in Figure 4.9a, the IR technique uses a magnitude reconstruction which means that if the TI time is underestimated, the contrast between the infarct and normal myocardium is reduced. Kellman et al (2002) developed the PSIR sequence to overcome this problem [33]. As shown in Figure 4.9b, the PSIR technique uses phase information to preserve the polarity of the magnetization meaning that the contrast between infarcted and viable myocardium is less sensitive to the choice of TI time.

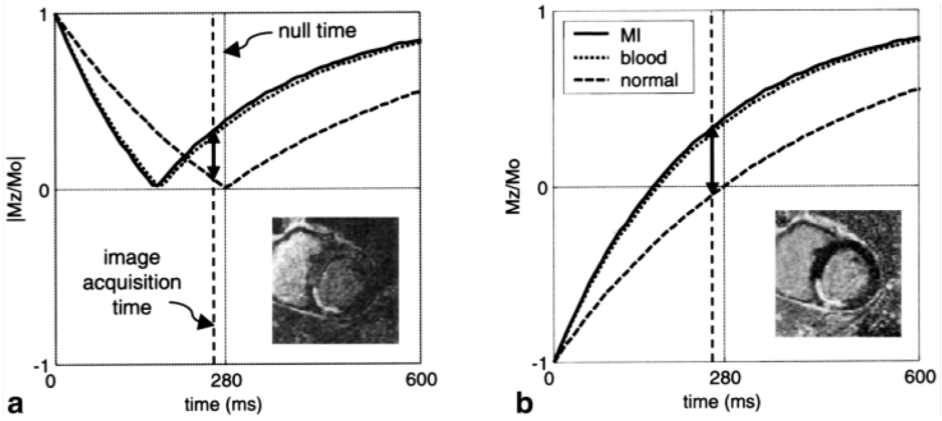

Figure 4-9: An underestimation of the null point of the myocardium in a) the IR sequence results in inferior contrast between scar and normal myocardium . However, the contrast between scar and normal myocardium in the b) PSIR sequence is maintained over a wide range of TI times [33].

4.3.2 T1 Mapping Techniques

The Look Locker sequence produces a series of images with different inversion times. ROI analysis can be used to calculate the T1 value of a particular tissue. T1 mapping techniques, on the other hand, produce one image in which the signal intensity reflects the T1 value of the spins within the voxel. This is achieved by plotting the signal intensity in a particular voxel against the TI time and fitting a curve using a multi-parametric non-linear least squares fitting algorithm. This is performed on a voxel-by-voxel basis in order to produce a map of the T1 relaxation values.

The traditional Look Locker approach produces images of the heart in different cardiac phases. As the heart undergoes significant morphological deformation during the cardiac cycle, the resulting T1 map would be inaccurate. To overcome this problem, Messogrolli et al (2004) developed the modified Look Locker Inversion Recovery (MOLLI) sequence for T1 mapping in the heart (Figure 4.10) [96]. Each single shot image is acquired at the same cardiac phase in mid-diastole when the heart is quiescent. After an initial inversion pulse, a single shot image is acquired, two further images are acquired in the following two heartbeats in the same phase. A period of four seconds is then allowed for complete relaxation of the magnetization to its equilibrium value. A repetition of the first three heartbeats is then performed but with a larger gap between the inversion pulse and the image acquisition. After a

second rest period of 4 seconds, this sequence is played out again with a larger still delay between the inversion and the image acquisition and five images instead of three are acquired. In total this results in eleven images with different TI values all in the same cardiac phase. The fitting of this data to a model thus results in an image relatively free from cardiac motion artifacts. As this sequence can be performed within a breath-hold, respiratory motion is also therefore avoided.

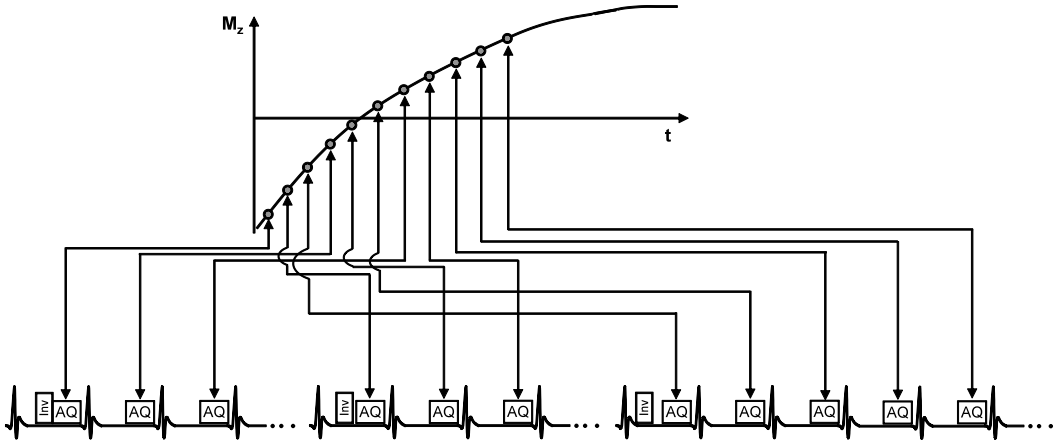

Figure 4-10: The acquisition scheme for T1 mapping using the MOLLI sequence (adapted from [96]).

4.4 *Strategies to Differentiate Scar from Blood in LGE Images*

Despite high contrast between the infarct and normal myocardium, at 5-20 minutes post-contrast administration, due to their similar T1 values during this time, there is often poor contrast between the blood pool and infarct. This can make it difficult to assess the size and transmurality of the infarct and to identify small sub-endocardial infarcts. Imaging can be performed later after contrast administration (>20 minutes), when the contrast concentration in the blood is lower. However, this can reduce patient throughput especially if the agent is slowly cleared from the blood due to patient physiology.

4.4.1 Subtractive Techniques

The endocardial border can be delineated on SSFP 'cine' images and used as a visual aid to interpret the IR image [97]. It can however be time-consuming to interpret the results due to differences between spatial and temporal resolution of the two sets of images. The results can also be inaccurate because of differences in image position due to separate breath-holds.

4.4.2 Multi-contrast Techniques

Kellman et al (2005) developed a LGE approach to allow differentiation of infarct from blood by exploiting the fact that T2 of blood is much longer than that of acute or chronic MI [35]. This sequence, known as multi-contrast delayed enhancement (MCODE), combines a PSIR sequence with a T2-weighted image acquisition. The two images have identical spatial resolution and slice position and are acquired in the same cardiac and respiratory phase which aids spatial registration of the two images.

The T1 weighted PSIR image provides good differentiation between the infarcted and normal myocardium due their differences in T1. The T2-weighted image on the other hand, displays similar signal intensity for infarcted and normal myocardium but higher blood signal. In this way the combination of the two images can aid the definition of the endocardial border. The multi-contrast images can be analyzed by method of outlining the epi and endocardial borders on the T2 weighted images and transferring the contours onto the T1-weighted image to aid infarct delineation. There was also the option of overlaying the images and 'flickering' between the T1 and T2 weighted images. The T2 weighted images unfortunately do not exhibit pure T2 weighting as there is also some residual T1 weighting from the inversion pre-pulse. Another drawback is the fact that 3 heartbeats are required to acquire the PSIR and T2-weighted images.

This technique has also been extended by interleaving T1 and T2 mapping acquisitions [98]. Although T2-weighted images and T2 maps help to distinguish infarct from blood, the imaging time is increased and the two images must still be overlaid to determine the endocardial border.

4.4.3 Flow Dependent Black Blood LGE Approaches

There is therefore interest in developing an imaging sequence which will simultaneously null blood and normal myocardium whilst preserving high signal in the infarct. One such sequence has been proposed and which prepares the blood and myocardium magnetization differently [37]. This sequence, shown in Figure 4.11a, consists of a slice-selective inversion pulse (SSIR), followed by a time delay (TD1), a non-selective inversion pulse (NSIR), then a second time delay (TD2) followed by image acquisition. Assuming sufficient in-flow of blood during the time, TD1, the

imaged blood will only experience the non-selective pulse whereas the infarcted and viable myocardium will experience both pulses.

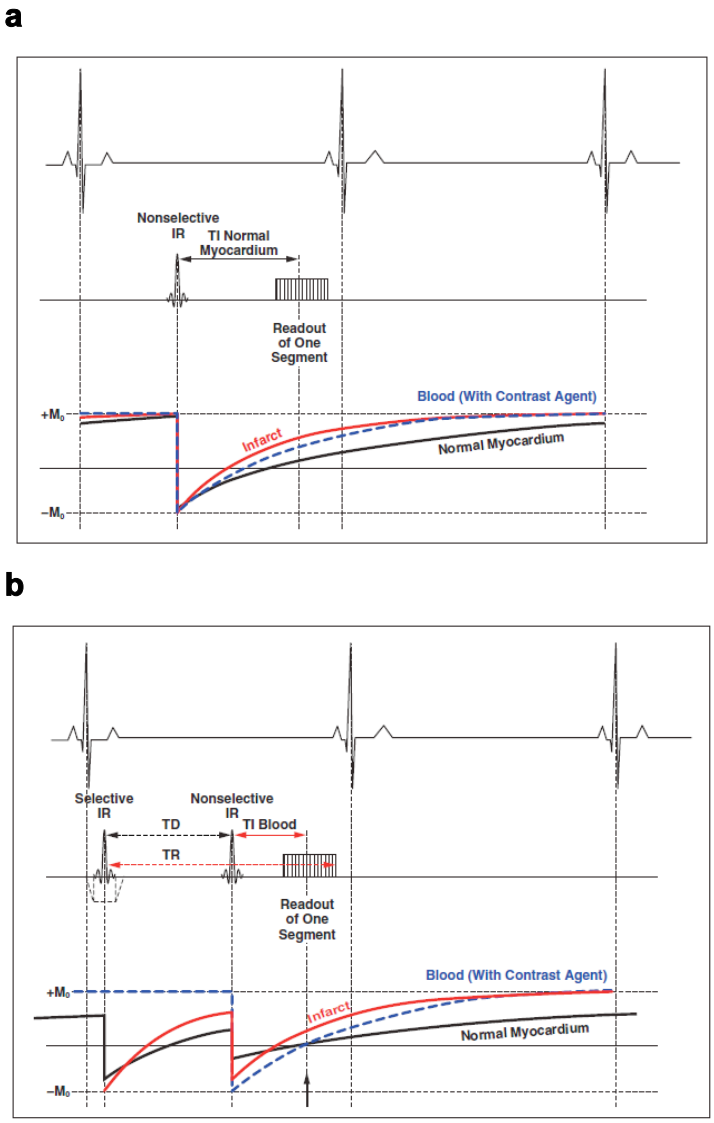

Figure 4-11: The pulse sequence and magnetization evolution for a) the IR sequence and b) the SSIR-NSIR sequence [37].

Whereas the IR sequence requires the operator to choose one TI delay time to null the healthy myocardium, the SSIR-NSIR requires the selction of two delay times. Firstly the TI which is required to null the blood pool is chosen by examining the preceeding Look Locker scan. The delay, TD2 is set to equal TIblood. As the magnetization of normal myocardium will experience both inversion pulses, the first delay, TD1, must be timed so that in combination with the specified TD2, the myocardium is nulled. The Look Locker is used to calculate TInormal, the TI which

corresponds to the Look Locker image with the lowest signal from normal myocardium.

As derived in chapter 2, the Bloch equation describing T1 recovery of M_z is as follows:

$$M_z(t) = M_0 + (M_Z - M_0)e^{-t/T_1}$$

Equation 4-3

If M_1 is the magnetization just after the first inversion pulse and M_2 is the magnetization immediately prior to the second inversion pulse. The first time delay, TD1, can be expressed as:

$$TD1 = \frac{TI_{normal}}{\ln(2)} \ln\left[\frac{-2M_0}{M_2 - M_0}\right]$$

Equation 4-4

By considering the value of M_2 which is required for the magnetization of the normal myocardial cross zero follwoing the time period TD2 after the second inversion pulse,TD1 can be related to $TI1_{blood}$ and TI_{normal} using the following equation for M_2:

$$M_2 = M_0\left[e^{\frac{TI_{blood}\ln(2)}{TI_{normal}}} - 1\right]$$

Equation 4-5

For effective blood supression, there must be complete blood exchange out of the imaging slice between the slice selective inversion pulse and the imaging sequence. This ensures that blood present in the imaging slice at the time of image acquisition has only experienced the non-selective inversion pulse.

The SSIR-NSIR sequence was compared to the standard IR technique in three pigs with induced MI and twenty six patients with a known history of MI. The authors found the $CNR_{inf\text{-}blood}$ was higher using the SSIR-NSIR technique compared with the IR technique. However, the $CNR_{inf\text{-}myo}$ and SNR_{inf} were both decreased using the SSIR-NSIR technique. The mean $SI_{blood\text{-}myo}$ was significantly, higher in those

patients with a a left ventricular ejection fraction less than or equal to 40 % compared to those with an ejction fraction greater than 40 %.

Qualitative analysis of patient data showed that experts detected hyperenhancement in more segments and a statistically significant increase in the number of scars with transmurality between 0-25 % (subendocardial) was observed with the SSIR-NSIR technique compared to the IR technique. The experts gave the SSIR-NSIR images higher scores for infarct conspicuity but lower confidence values for grading transmurality.

The problems with the SSIR-NSIR approach include the flow dependence of blood suppression requiring sufficient blood exchange between the two inversion pulses. Many of the patients who undergo delayed enhancemnt imaging will have severely impaired ejection fraction and the sequence will result in impaired blood suppression. Also because it relies on the precise timing of the two inversion pulses which are calculated based on TI_{blood} and TI_{normal}, the technique is also sensitive to changes in TI_{blood} and TI_{normal} which can change with time after contrast administration.

4.4.4 Diffusion Sensitized Gradients for Black Blood LGE Imaging

The blood suppression in DIR imaging relies on the complete exchange of blood which can be compromised for thick imaging volumes and for in-plane flow. Diffusion-Sensitized gradients have been applied to the heart in healthy volunteers [99]. The mechanism of blood signal attenuation was found to be the velocity encoding effect acting on spins which are moving in a coherent fashion with only a slight effect from diffusion on incoherently moving spins. Salerno et al (2009) have combined the standard IR sequence with diffusion sensitizing gradients (DP-IR) to achieve black-blood LGE images [100].

In a canine model of chronic infarction, there was a greater than 700 % increase in $CNR_{inf\text{-}blood}$ but a 25 % decrease in SNR_{inf} and a 40 % decrease in $CNR_{inf\text{-}myo}$ [36]. The DP-IR technique appears to improve the visualization of sub-endocardial infarcts in images taken at 5-10 minutes after administration of 0.15 mmol/kg of Magnevist (Figure 4.11). The DP-IR technique does not rely on complete blood

exchange and should be relatively insensitive to changes in the relaxation times. Although the blood suppression is clearly effective, there is also reduced differentiation between blood pool and healthy myocardium which might make it difficult to define the epicardial border which is also vital for accurate transmurality assessment.

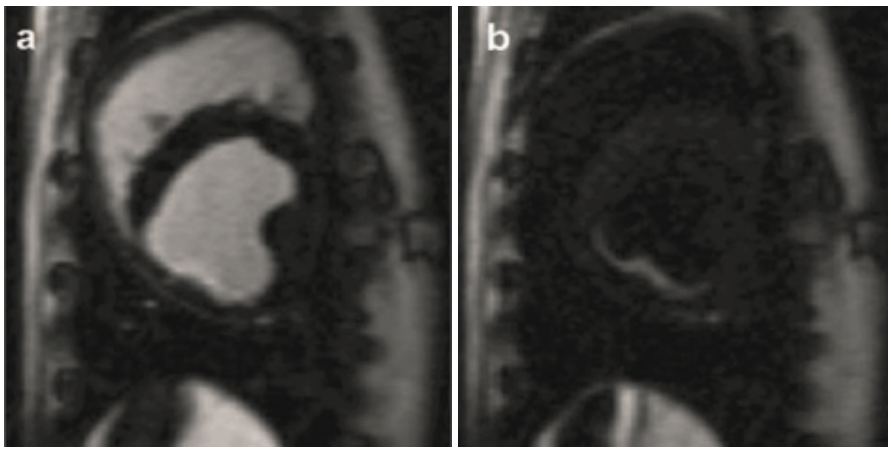

Figure 4-12: a) IR-TFE and b) diffusion-prepared IR images in a canine model of chronic infarction [100].

4.5 *Summary*

The traditional IR pre-pulse can be optimized to achieve high contrast between scar and normal myocardium. However, it can also result in high blood signal which can hamper the detection of small infarcts and the assessment of transmurality and scar size. There have been attempts at improving blood suppression by waiting longer after contrast administration but this increases the overall scan time. A flow-dependent technique has been developed [37], however the blood suppression was found to be significantly less effective in patients with an impaired ejection fraction. DSG gradient preparation has been shown to effectively suppress the blood, but the epicardial border is then difficult to define [36]. There is therefore a need to develop a flow-independent LGE technique which reduces but does not completely suppress the blood signal to aid scar detection and assessment.

Chapter 5

5. Novel Dual-IR Pre-pulse for Improved Blood Suppression in LGE imaging of Myocardial Scar

5.1 *Introduction*

The IR-GE sequence remains the gold standard for LGE imaging of myocardial scar. As it is less sensitive to changes in TI, the PSIR approach is also often used clinically and in research studies. Both the IR and PSIR sequences null only the T1 value which relates to healthy myocardium. This results in high contrast between scarred and normal myocardium. However, there can be also high signal from other T1 species including blood which can result in poor contrast between scar and blood pool. In some cases, this can make it difficult to accurately delineate the endocardial border which in turn can compromise accurate assessment of scar size and identification of small sub-endocardial scars. An alternative pulse sequence has been previously developed which uses an additional slice selective inversion to null the signal from blood [37]. This approach is however reliant on sufficient blood exchange to achieve black blood properties. There is therefore interest in a flow-independent technique which improves blood suppression in LGE imaging of myocardial scar.

I implemented a dual inversion recovery (dual-IR) pre-pulse which was optimized to suppress the signal of tissues and blood within a wide T1 range so that only short T1 species generate a high signal. My hypothesis is that this sequence will allow specific visualization of the contrast agent whilst suppressing the background signal

and reducing blood signal, as long as the T1 of blood is greater than that of scar. I sought to investigate whether this leads to improved contrast between scar and blood, higher confidence in the detection and evaluation of scar as well as more consistent scar size and transmurality assessment.

5.2 *Methods*

5.2.1 The Dual-IR Pre-pulse

The dual-IR sequence is a modification of the QIR sequence described in chapter 3. Whereas the QIR sequence consists of two double inversion pre-pulses, the dual-IR sequence consists of two non-selective inversion pulses (Figure 5.1).

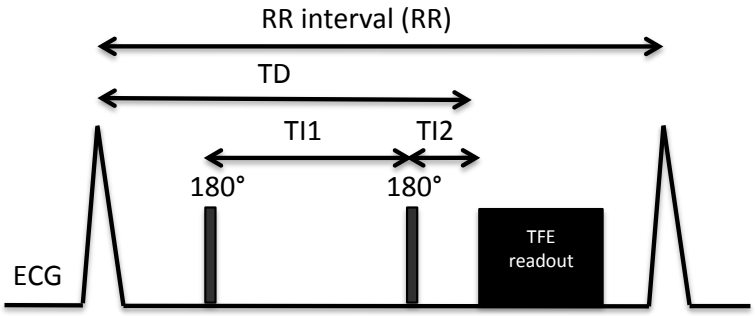

Figure 5-1: The dual-IR pre-pulse combined with TFE read-out

5.2.2 Simulations

5.2.2.1 Optimization of the TI1 and TI2 Delays in the Dual-IR Pre-pulse

Whereas the aim of the QIR pre-pulse (described in chapter 3) was to suppress only the blood signal, I aimed to optimize the dual-IR pre-pulse to suppress the signal from tissue as well as blood within a defined T1 range. In the QIR implementation, the TI1 and TI2 delays were optimized to minimize the blood signal for T1 values between 100 and 1400 ms signal in order to ensure pre and post contrast blood suppression. In the dual-IR sequence, the aim is to suppress the signal of healthy myocardium and to suppress the signal from blood but it is also important to maintain as high as possible signal in the areas of scar. Rather than just one

suppression range, the optimization was performed for different suppression ranges for different heart rates to examine which produced the best image contrast. I decided to optimize the TI1 and TI2 delays in the dual-IR sequence using the same approach as in chapter 3 by minimizing the integral of $M_z b$ within a defined suppression range using equation 2.5. $T1_{min}$ was varied between 50, 100, 200 and 300 ms with $T1_{max}$ always set at 1400 ms. The optimal TI1 and TI2 delays were then programmed to be automatically calculated by the scanner software based on the $T1_{min}$ value selected by the user and the patient's heart rate.

5.2.2.2 Simulation of the Evolution of Mz for Tissue and Blood in the IR and Dual-IR Sequences

Equations 2.5 and 2.6 describe the signal characteristics for blood which will only experience the inversion pulses. The tissue on the other hand will also experience the imaging sequence. In the IR and dual-IR sequences, in each RR period, tissues will experience:

IR Sequence (tissue): 180 °– TI – (α °- TR)*N – TD

Equation 5-1

Dual-IR Sequence (tissue): 180 °– TI1 – 180 °– TI2 – (α °- TR)*N – TD

Equation 5-2

where α is the imaging flip angle and N is the number of radio frequency (RF) excitations and TR is the time between the RF pulses used for imaging. With RR being the time between two R-waves, the time between the end of the imaging sequence and the following inversion pulse (TD) can be expressed as:

IR Sequence(tissue): TD = RR – TI – N*TR

Equation 5-3

Dual-IR Sequence(tissue): : TD = RR – TI1 – TI2 – N*TR

Equation 5-4

Simulations were performed in MATLAB to examine the evolution of the longitudinal magnetization of tissue (M_zt) and that of blood (M_zb) separately. M_zt and M_zb were calculated for the IR and dual-IR sequences over ten cardiac cycles using equation 5.5 to determine the effect of the pre-pulses and imaging sequence on the tissue and blood separately.

$$Mz(t) = Mz.e^{-t/T_1}.\cos(\alpha) + M_0(1-e^{-t/T_1})$$

Equation 5-5

where T1 is the T1 relaxation constant, ∝(t) is the flip angle applied as a function of time and M_0 is the equilibrium magnetization. For the M_zt simulations, the number of RF excitations (N) was set to 13 for imaging every heartbeat and to 25 for imaging every two heartbeats. A constant flip angle of 25 º was applied for all imaging RF pulses with a TR of 4 ms. A low-high phase order was assumed, meaning that the first echo in each heartbeat is used to fill the central lines of k-space. The value of M_zt at the beginning of image acquisition was plotted versus T1 for each heartbeat. This was used to examine the number of cardiac cycles required for M_zt and M_zb to reach a steady state.

In the IR sequence, the Fleckenstein formula [49] was used to calculate the optimal TI to null healthy myocardium for a given heart rate assuming a T1 value of 535 ms for the myocardium. In the dual-IR sequence, the TI1 and TI2 delays were optimized for each heart rate to null the signal in the T1 range between 200 and 1400 ms. These simulations were performed for heart rates of 45, 75 and 105 bpm (imaging every heartbeat and every two heartbeats). In the IR sequence, 'imaging every two heartbeats' refers to applying the inversion pulse and imaging sequence in the first heartbeat and then waiting an entire cardiac cycle to allow for T1 recovery. In the

dual-IR sequence, ‘imaging every two heartbeats’ refers to allowing the pre-pulse to be played out over the time period of two RR intervals. This aims to produce signal characteristics that would be achieved at half the heart rate.

5.2.3 Phantom Studies

For both the IR sequence (imaging every two heartbeats) and the optimized dual-IR sequence (imaging every heartbeat), simulations were performed for different heart-rates to calculate the signal which is available at the time of imaging for T1 species between 1 and 1400 ms. This was calculated once a steady state had been achieved between heartbeats. The SNR of different T1 samples was calculated from scans of a T1 phantom using the IR and dual-IR sequences at simulated heart rates of 45, 75 and 105 bpm. The phantom consisted of tubes containing gel samples made from agarose doped with Gadolinium, inserted in a holder filled with a copper sulphate solution. The samples had T1 values ranging from 140 to 1720 ms. Imaging parameters were set as for the simulations with a spatial resolution of 1.5 x 1.5 x 15 mm, a constant flip angle of 25 º, a TE of 2 ms and a low-high (centric) phase order. To ensure that a steady-state had been established between heartbeats, ten start-up shots were used. Four signal averages were used. N = 1 was used to simulate the characteristics of blood.

A scan with the IR or dual-IR sequence enabled but with the RF and gradients of the imaging sequence switched off was used to estimate noise. As for the phantom measurements performed for the QIR pre-pulse in chapter 3, the SNR was calculated for each sample using equation 3.6. The phantom was also scanned with no pre-pulses and the TR_{eff} set to five times the longest T1 species. The SNR measurements from this scan were then used to normalize the measured SNR values to the fully

relaxed magnetization in order to compare them to the simulated M_zb and M_zt values.

5.2.4 Volunteer Studies

In order to examine the signal suppression of the dual-IR sequence, three healthy volunteers were imaged at 3.0 T using a 32 channel coil without contrast administration. A single short axis slice was acquired using the same parameters as the patient studies (see below) but with N set to 13 for every heartbeat and 25 for imaging every 2 heartbeats. The effect of changing the number of start-up cycles was examined for both the IR and dual-IR sequences.

5.2.5 Patient Studies

Fifteen male patients (63 ± 8 years) with a history of MI at least 3 months prior and who were known to have LGE on previous clinical IR images were consecutively recruited between October 2010 and April 2011. Patients with contraindications for MRI were excluded. This prospective study was approved by the local ethics committee and all patients gave their written informed consent. All scans were performed using a 32-channel coil on a 3.0 T Achieva MR Scanner (Philips Healthcare, Best, the Netherlands). Three patients were used to optimize the MR protocol. The remaining twelve patients were then consecutively imaged as follows: after initial localizer scans, patients were administered 0.2 mmol/kg of Gadobutrol (Gadovist, Bayer Healthcare). Five minutes after contrast injection, breath-hold 2D IR segmented GE scans were performed to image three slices in the expected scar location on previous clinical LGE IR images. Imaging parameters included: spatial resolution = 1.5 x 1.5 x 10 mm, repetition time = 3.8 ms, echo time = 2 ms, two start-up shots, constant flip angle = 25 °, imaging every other heartbeat. The TFE factor was adjusted to achieve the 12 second breath-hold for each patient. The TI

was set to null the myocardium according to a preceding Look Looker scan. An imaging slice, which demonstrated the scar, was selected as the slice position for all subsequent single-slice images.

The following scans were then performed at 10, 20 and 30 minutes post-contrast in the selected slice position. A Look Locker scan followed by a breath-hold 2D IR-TFE sequence (parameters set as above). Dual-IR scans were then acquired with $T1_{min}$ set at 50, 100, 200 and 300 ms. All dual-IR scans were performed every heartbeat with the TFE factor adjusted to achieve a 12 second breath-hold for each patient. The order of the dual-IR scans was randomized for each patient prior to the start of the imaging session. In five of the patients, additional 2 or 4 chamber views were also acquired at 25 or 35 minutes post-contrast.

5.2.6 Expert Analysis

Short axis IR and dual-IR images taken at 20 minutes post-contrast were presented on different occasions in a random order to two blinded, independent experts, Amedeo Chiribiri and Andreas Schuster, who both have at least 5 years experience in cardiovascular MR. They were asked to identify the scars in each image and estimate the maximum transmurality of each scar as 0 - 25, 26 - 50, 51 - 75 and 76 - 100 %. They also manually traced the borders of each identified scar using Osirix Imaging Software (version 3.2.1, Los Angeles, California) and gave each scar a confidence score for scar detection and transmurality assessment with 1) being negative low confidence, 2) negative medium confidence, 3) negative high confidence, 4) positive low confidence, 5) positive medium confidence and 6) positive high confidence. Enhancement of the papillary muscle was not included in this analysis.

5.2.7 SNR and CNR Measurements

Osirix Imaging Software (version 3.2.1, Los Angeles, California) was used to measure the mean signal intensity in regions of interest in scar, remote myocardium and left ventricular blood pool and the standard deviation of signal in the lung. The SNR of blood pool, myocardium and scar and the scar-to-blood CNR, scar-to-myocardium CNR and blood-to-myocardium CNR were calculated for all short-axis images at all time points.

5.2.8 Statistical Analysis

SPSS version 20 (IBM Software Group, New York, USA) was used to compare CNR and SNR measurements with a one-way Analysis of Variance between groups (ANOVA) which included both time after contrast administration and scan type as separate factors. A post-hoc Bonferroni test was performed to adjust for multiple comparisons. The differences between the confidence scores were compared using a Wilcoxon matched-pairs signed ranks test. The percentage of infarcts where the experts gave a different transmurality assessment was compared using a student t-test. The inter-observer variability for the scar size was assessed using the Bland Altman test and the Pearson's correlation coefficient. I made the assumption that if patients had more than one region of scar, each was evaluated independently.

5.3 *Results*

5.3.1 Simulations

5.3.1.1 Optimization of the TI1 and TI2 Delays in the Dual-IR Pre-pulse

The TI1 and TI2 delays in the dual-IR pre-pulse were optimized for four different T1 suppression ranges according to TR_{eff} (Figure 5.2).

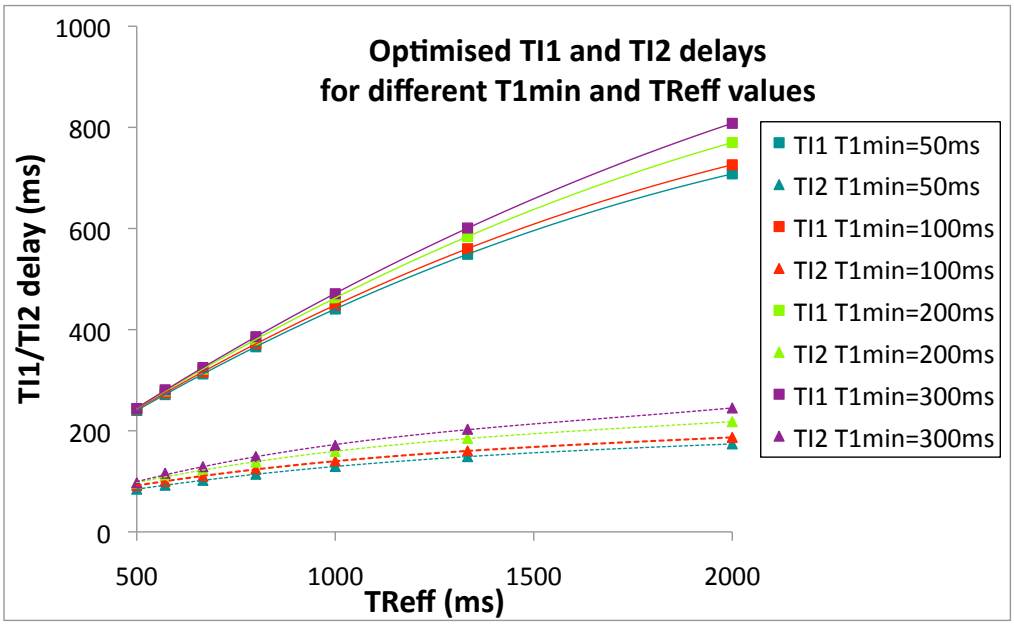

Figure 5-2: The TI1 and TI2 delays optimized to achieve signal suppression in four different T1 ranges according to TR_{eff}.

5.3.1.2 Simulation of M_zb and M_zt in the IR and dual-IR Sequences

M_zt simulations for the IR sequence indicate that, for a heart rate of 60 bpm, a steady state is reached by the third heartbeat when imaging every heartbeat (Figure 5.3a) and by the second heartbeat when imaging every other heartbeat (Figure 5.3b). The M_zb simulations show that it takes seven heartbeats for blood to reach a steady state when imaging every heartbeat (Figure 5.3c) whereas a steady state is reached after only four heartbeats when imaging every other heartbeat (Figure 5.3d.)

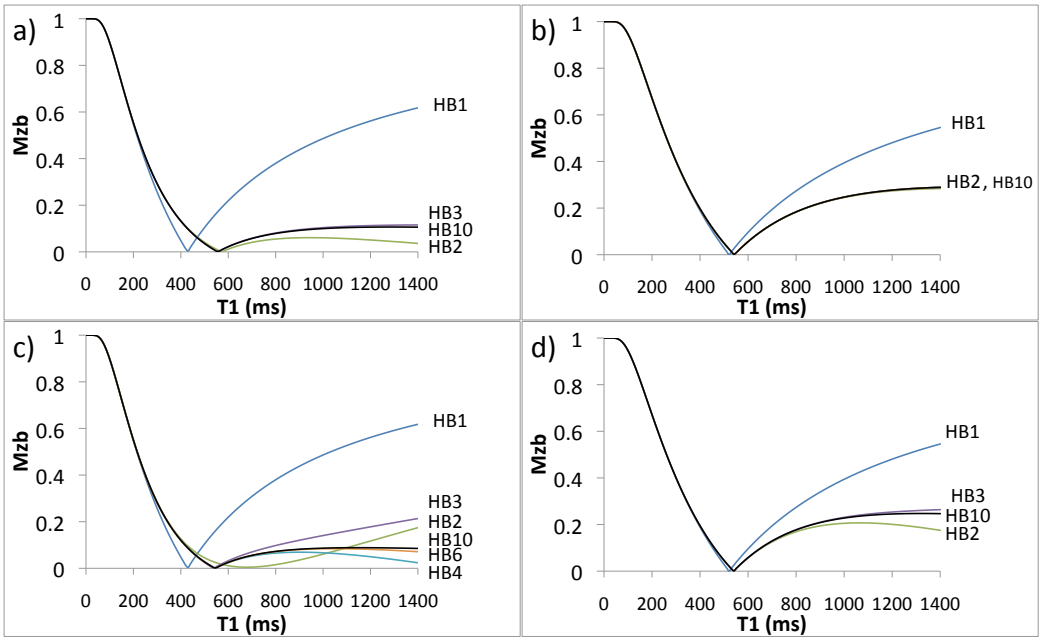

Figure 5-3: The simulated M_zt values in the IR sequence for each cardiac cycle for a heart rate of 60 bpm: a) imaging every heartbeat and b) imaging every other heartbeat and the simulated M_zb values for c) imaging every heartbeat and d) imaging every other heartbeat.

The M_zt simulations for the dual-IR sequence show that, as with the IR sequence, three start-up cycles are required to reach a steady state when imaging every heartbeat (Figure 5.4a) whereas two are sufficient when imaging every other heartbeat (Figure 5.4b). The M_zb simulations show that, six cycles are required for blood signal to reach a steady state when imaging every heartbeat (Figure 5.4c). Once this is reached, the blood signal should be suppressed in the entire defined T1 range. Only three cycles are required to reach a steady state when imaging every other heartbeat (Figure 5.4d), however the signal suppression within the T1-range may not be as optimal.

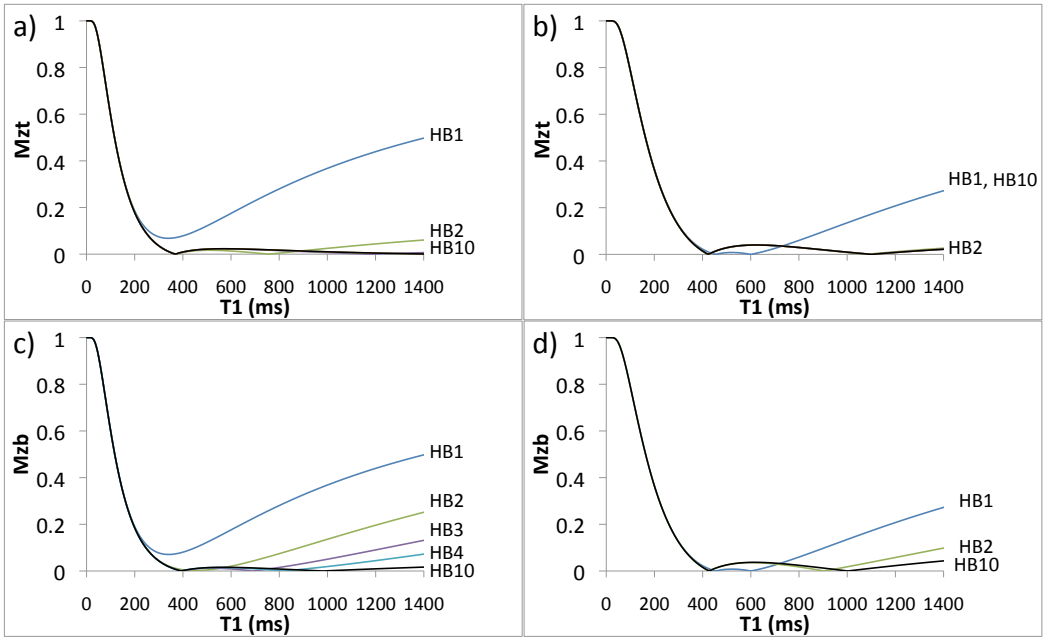

Figure 5-4: The M_zt simulations in the dual-IR sequence for each cardiac cycle for a heart rate of 60 bpm a) imaging every heartbeat and b) imaging every heartbeat and the M_zb simulations c) imaging every heartbeat and d) imaging every heartbeat.

5.3.2 Phantom Studies

The M_zb at the time of imaging was plotted versus T1 for the IR and dual-IR sequences (lines in Figure 5.5a, b and c) and were in good agreement with phantom SNR measurements (markers). For the IR sequence the signal is zero only for one specific T1 value (T1 = 535 ms) while the signal is suppressed over a wide T1 range for the dual-IR sequence. In both sequences there is a relatively linear relationship between signal intensity and T1 for T1 values less than the null point or T1 min value, respectively. There is also a variation of both the IR and dual-IR signal characteristics with heart rate. In the dual-IR sequence the signal below $T1_{min}$ is suppressed to a greater extent for high heart rates (Figure 5.5b). For a constant heart rate, the range of signal suppression of the dual-IR sequence varies with the choice of the $T1_{min}$ value (Figure 5.5c).

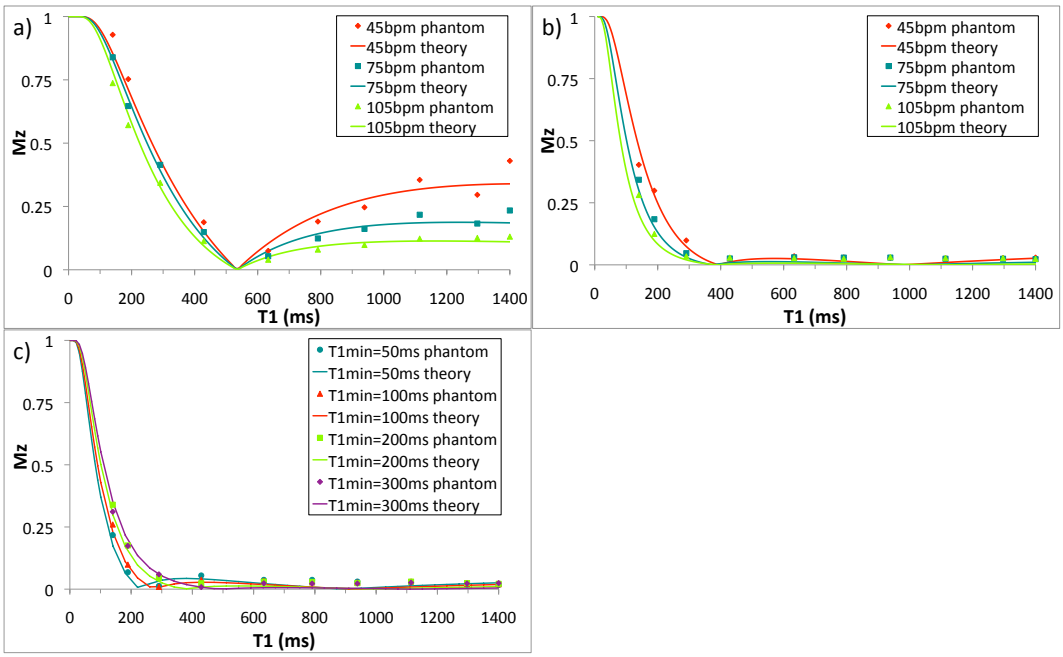

Figure 5-5: Normalized M_zb values from simulations (lines) and SNR measurements from phantom experiments (points) for a) the IR sequence with TI chosen using the Fleckenstein formula [49] to null a T1 of 535 ms for normal myocardium derived from the Look Locker measurements at 20 minutes for each heart-rate and the dual-IR sequence with $T1_{min}$=200 ms for different heart-rates and c) for the dual-IR sequence for a heart-rate of 75 bpm with different $T1_{min}$ values. Heart rate variation has little effect on signal suppression of long T1 values (e.g. normal myocardium) but leads to variable suppression of tissues with short T1 values.

5.3.3 Volunteer Studies

For the IR sequence, when imaging every heartbeat (images 5.6a-e), at least 2 start-up cycles were required to overcome the ghosting artifacts caused by Mz modulation. When imaging every 2 heartbeats (images 5.6f-j), only 1 start-up cycle was sufficient to avoid significant ghosting. This is consistent with theoretical simulations which indicated that a steady state was established sooner when imaging every other heartbeat. For the dual-IR sequence, when imaging every heartbeat (images 5.6k-o), at least two start-up cycles were required to avoid ghosting and achieve suppression of the blood signal. When imaging every 2 heartbeats (images 5.6p-t), high image quality and blood suppression was achieved with only 1 start-up

cycle. It can also be seen that imaging every two heartbeats increases the signal for the short T1 species (e.g. the fat in the chest wall) compared to imaging every heartbeat. However, there appears to be inferior blood suppression in the right ventricle. From these results, it was decided to perform the IR sequence imaging every other heartbeat and the dual-IR sequence imaging every heartbeat both with two start-up cycles.

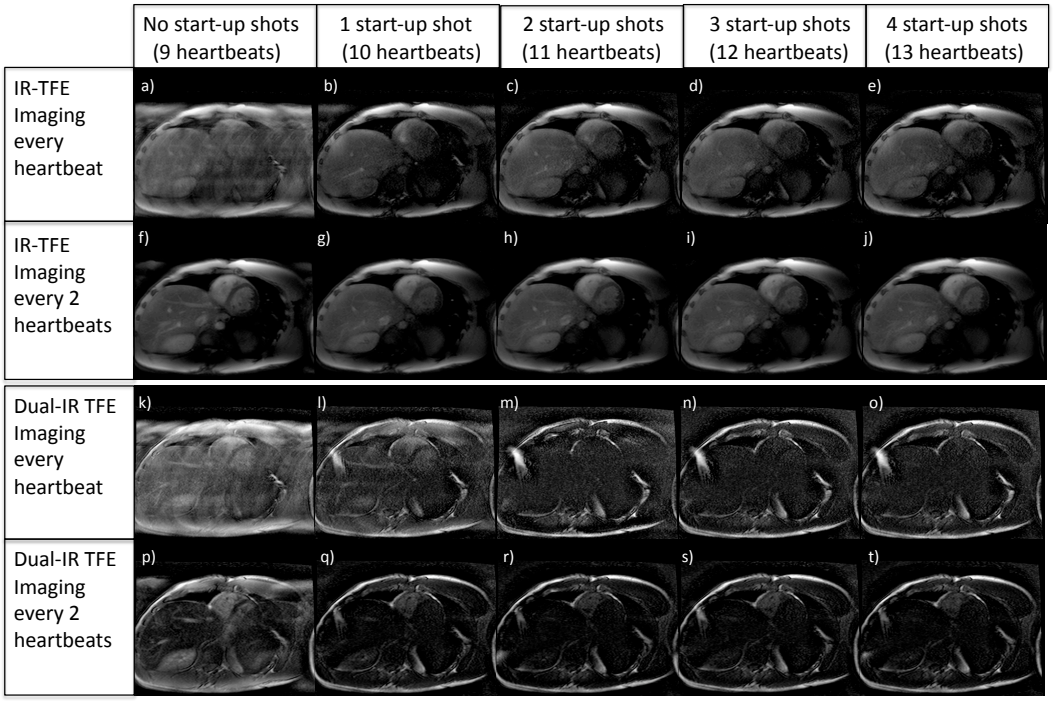

Figure 5-6: Images in a volunteer (heart-rate 60 bpm) from left to right with: no start-up cycles, 1 start-up cycles, 2 start-up cycles, 3 start-up cycles and 4 start-up cycles using the IR sequence imaging every heartbeat (a-e) and imaging every 2 heartbeats (f-j), and the dual-IR sequence with $T1_{min}$ set at 200 ms, imaging every heartbeat (k-o) and imaging every 2 heartbeats (p-t).

5.3.4 Patient Studies

Imaging was successfully performed in all patients. Patient characteristics are shown in Table 1.

Age (Mean ± standard deviation)	63 ± 8 years
Weight	84 ± 12 kg
Heart rate	60 ± 8 bpm
Scar age	60 ± 74 months
LVEF*	44 ± 9 %.
Male	100 %
Diabetes	17 %
Hypertension	83 %
Smokers	42 %
Hypercholesterolemia	58 %
Previous percutaneous coronary intervention	83 %
Previous coronary artery bypass graft	42 %
Scar location†	50 % inferior, 17 % lateral, 8 % anterior and inferior, 25 % anterior / antero-septal.

Table 5-1: Patient characteristics. *LVEF = left ventricular ejection fraction (measured on short-axis cine images in the previous MR clinical scan), †Scar location was assessed on previous clinical IR images.

Representative images in one patient (Figure 5.7) show that the dual-IR sequence reduces the blood signal compared to the IR sequence. The level of blood signal reduction can be controlled by adjusting the $T1_{min}$ value. For the same $T1_{min}$ value, blood signal is reduced at later time points after contrast administration as the T1 of blood increases. The blood appears bright at all three time points for the IR sequence which hampers the delineation of the endocardial border.

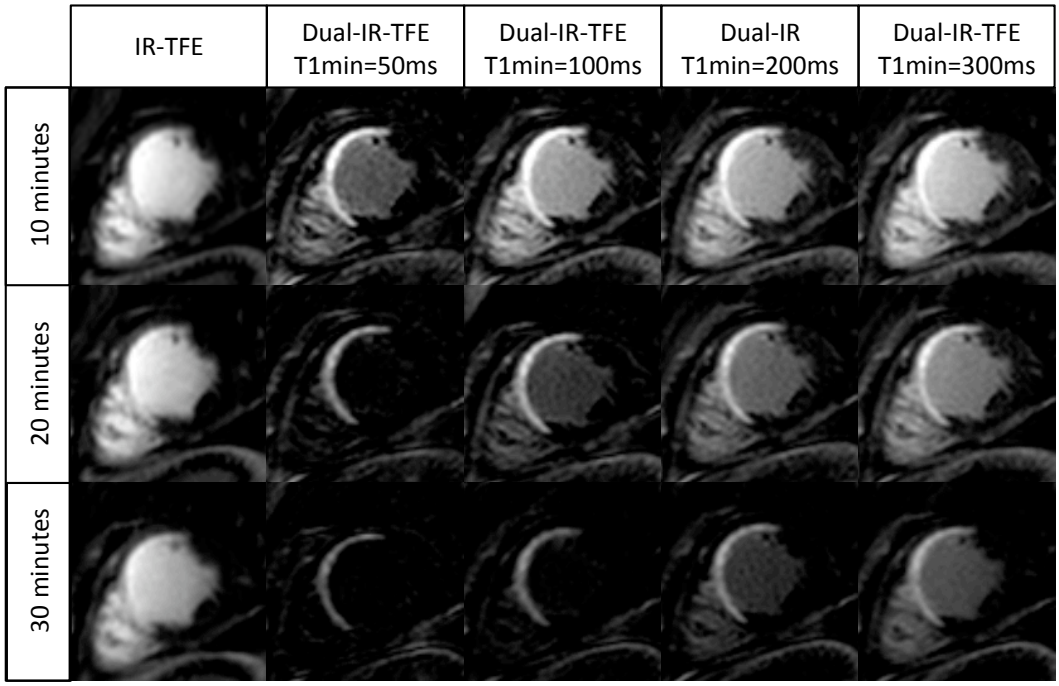

Figure 5-7: Representative image in a patient aged 62 years. Images in a short axis view taken at 10 minutes, 20 minutes and 30 minutes after contrast administration with the IR, dual IR with $T1_{min}$ = 50, 100 200 and 300 ms. Dual-IR images show reduced blood signal and improved scar delineation.

IR images and dual-IR images taken at 20 minutes post-contrast with a $T1_{min}$ of 200 ms in four patients (Figure 5.8) show that the dual-IR technique achieves blood signal reduction in all cases. Sub-endocardial scar appears to be more easily delineated with the dual-IR sequence. Four-chamber (Figure 5.9) and two chamber views taken (Figure 5.10) also show reduced blood signal with dual-IR technique and areas of contrast uptake are shown more clearly.

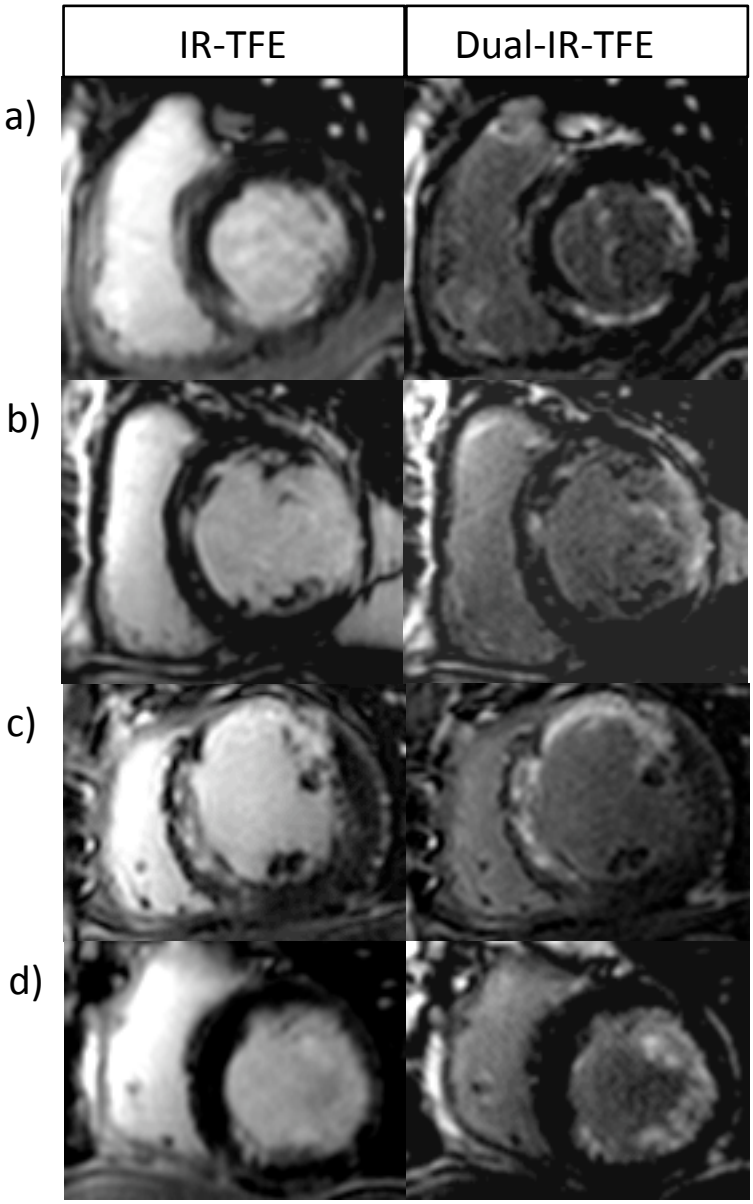

Figure 5-8: Short axis images in 4 patients at 20 minutes after contrast administration using the IR sequence (left) and the dual-IR sequence (right) with a $T1_{min}$ of 200 ms. (a) 73 year old patient with antero-lateral, infero-lateral and inferior sub-endocardial scar, (b) 72 year old patient with sub-endocardial antero-lateral, infero-lateral scar with some atypical patchy enhancement in the septum, (c) 64 year old patient with extensive scar which is transmural in the anterior wall and subendocardial in the septum and (d) 66 year old patient with thin subendocardial antero-lateral, infero-lateral and inferior scar. Dual-IR images showed equally good or improved scar visualization in all 12 patients compared to the IR sequence.

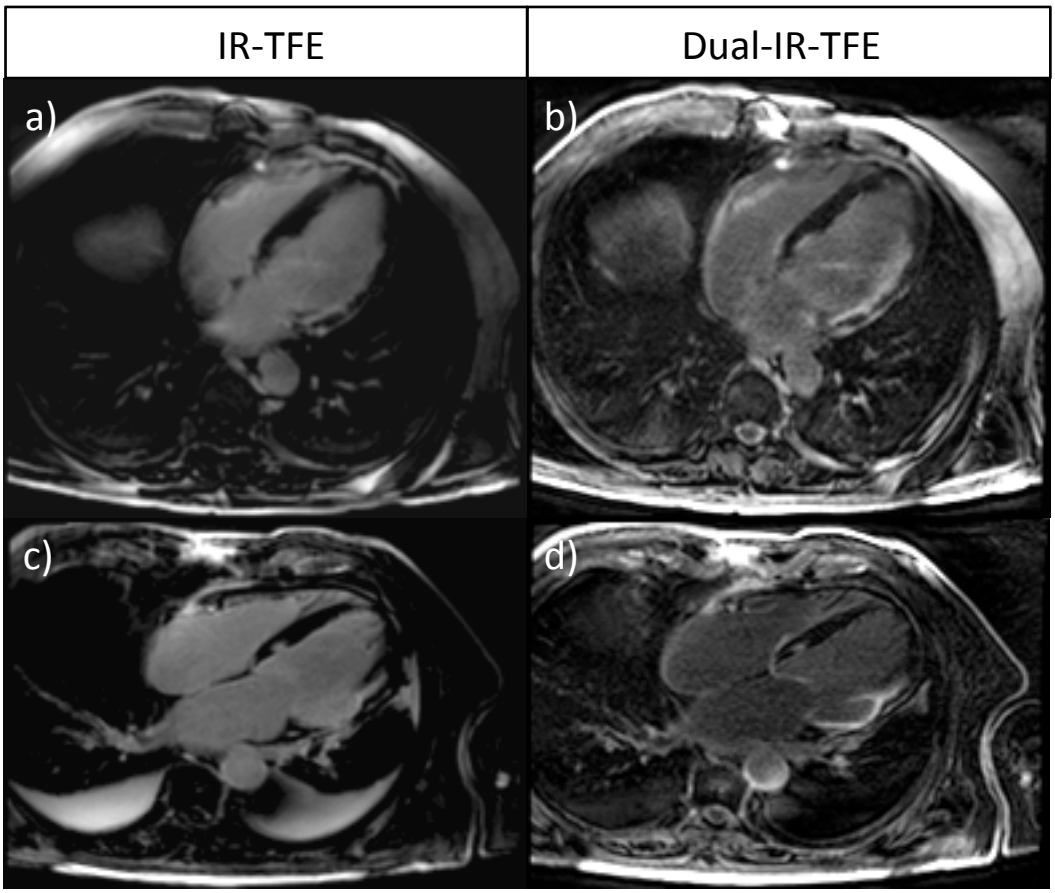

Figure 5-9: Four-chamber view taken at 25 minutes after contrast administration of a patient (aged 66 years old) with a sub-endocardial basal to mid lateral wall scar with the IR sequence (a) and the dual-IR sequence with a $T1_{min}$ of 200 ms (b), and a patient (aged 72 years old) with a transmural basal to mid lateral wall scar with the IR sequence (c) and the dual-IR sequence with a $T1_{min}$ of 200 ms (d). As well as improved myocardial scar depiction, the dual-IR sequence appears to suppress the signal in the pleural effusion and allows visualization of contrast uptake in the aortic and pulmonary artery vessel walls (d).

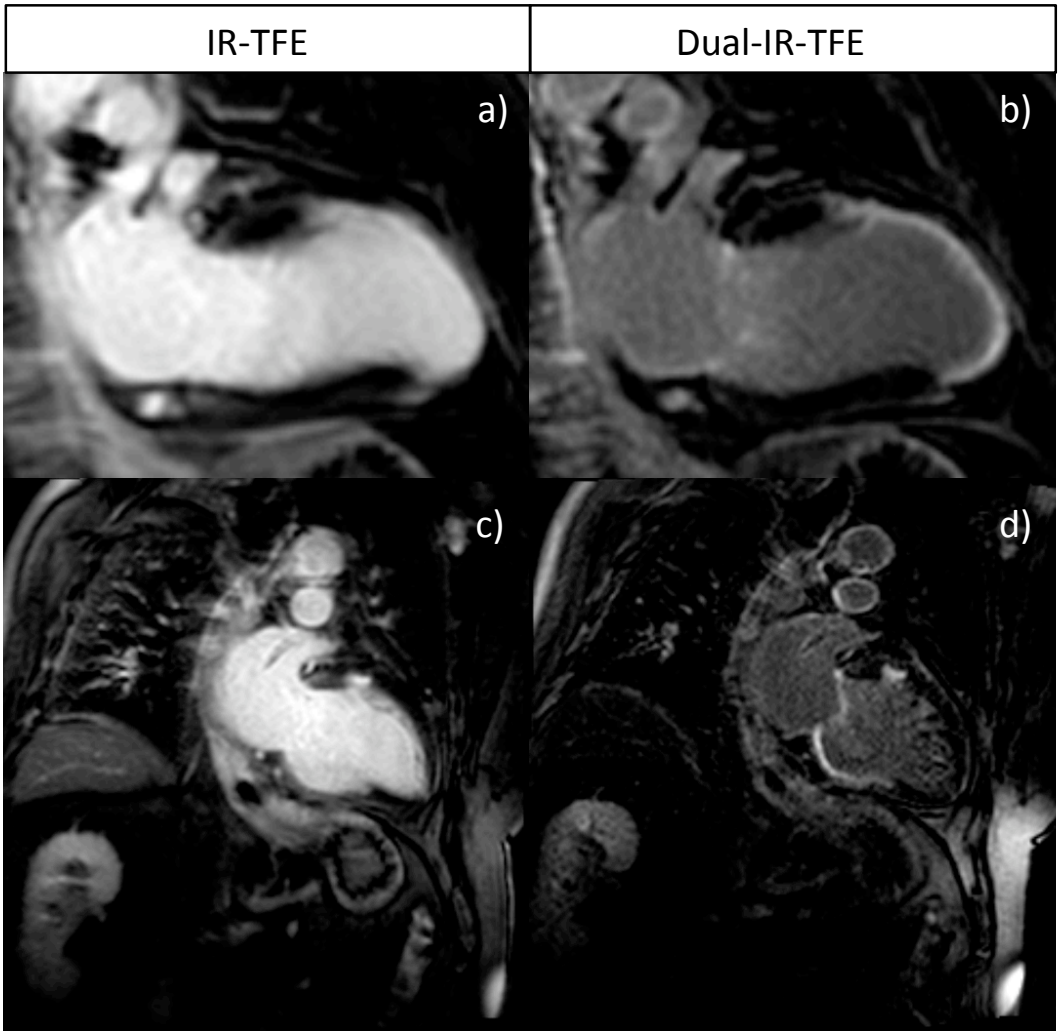

Figure 5-10: Two-chamber view taken at 25 minutes post contrast administration in a patient (aged 62 years old) with a transmural scar in the mid anterior wall and septum, which extends to the apex with the IR sequence (a) and the dual-IR sequence with a $T1_{min}$ of 200 ms (b) and a images taken at 35 minutes post-contrast administration of a patient (aged 70 years old) with a transmural basal to mid inferior wall scar and a small basal anterior wall scar with the IR sequence (c) and the dual-IR sequence with a $T1_{min}$ of 200 ms (d).

5.3.5 Expert Analysis

Scar presence (Figure 5.11a) and transmurality assessment (Figure 5.11b) confidence scores were higher with the dual-IR sequence (with $T1_{min}$ of 100, 200 and 300 ms) compared to the IR sequence for both experts. The differences in transmurality confidence scores were significant for expert 1 when the IR sequence was compared to the dual-IR sequence with $T1_{min}$ of 100, 200 and 300 ms ($p<0.05$). With the dual-IR sequence, there were fewer differences in transmurality assessment between the two experts compared to the IR sequence (Figure 5.11c). This was significant for the dual-IR technique with a $T1_{min}$ of 100 ms and 300 ms ($p<0.05$).

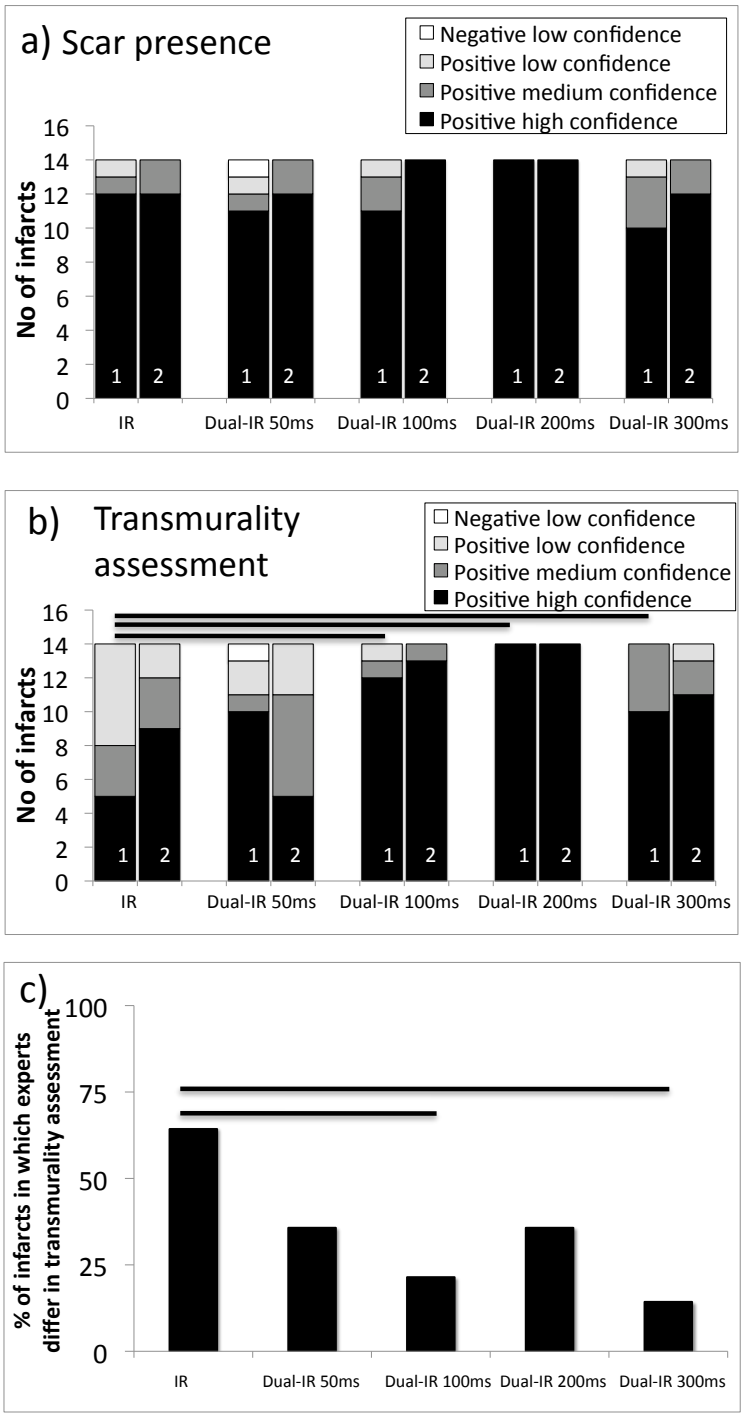

Figure 5-11: a) Scar presence and b) transmurality assessment confidence scores from the two independent experts (1 and 2), (the bars show the statistically significant differences as assessed using the Wilcoxon matched-paired signed rank test $p < 0.05$). c) Percentage of scars in which there was a difference of 25 % in the transmurality between the two experts. The bars show the statistically significant differences using a student t-test $p < 0.05$.

There was also a trend towards a better agreement in scar size assessment with the dual-IR sequence with $T1_{min}$ values of 100 ms, 200s and 300 ms as shown in the Bland Altman plots (Figure 5.12). The Pearson's correlation coefficient also demonstrated improved inter-observer variability for the dual-IR sequence. The R^2 value was 0.56 for the IR sequence ($p = 0.002$), 0.88 for the dual-IR sequence with $T1_{min}$ = 50 ms ($p<0.001$), 0.93 for the dual-IR sequence with $T1_{min}$ = 100 ms ($p<0.001$), 0.89 for the dual-IR sequence with $T1_{min}$ = 200 ms ($p<0.001$) and 0.94 for the dual-IR sequence with $T1_{min}$ = 300 ms ($p<0.001$).

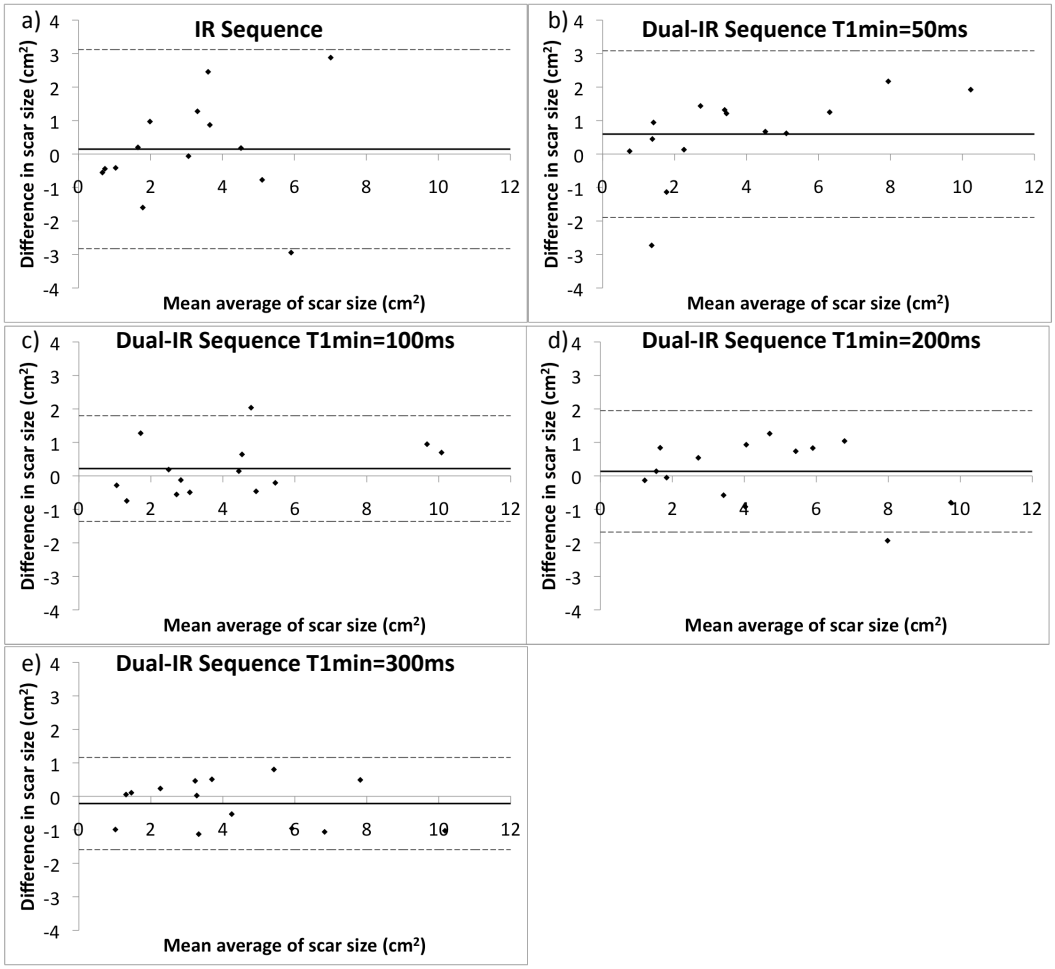

Figure 5-12: Bland Altman plots examining the difference in the scar size assessment between the two experts for a) IR images, b) dual IR images with $T1_{min}$ = 50 ms, c) dual IR images with $T1_{min}$ = 100 ms, d) dual IR images with $T1_{min}$ = 200 ms and dual IR images with $T1_{min}$ = 300 ms. Solid line indicates the mean of the differences and the dashed lines indicate 1.96 standard deviations above and below the mean of the differences.

5.3.6 SNR and CNR Measurements

When all time points were considered together, the blood SNR was found to be significantly higher for the IR sequence compared to the dual-IR sequence for all $T1_{min}$ values ($p < 0.05$) (Figure 5.13a). There was no significant difference in the myocardium SNR between the IR and the dual-IR sequence for any of the $T1_{min}$ values. A significant reduction in scar SNR was only found between the IR and the dual-IR scans with a $T1_{min}$ of 50 ms ($p < 0.05$) and 100 ms ($p < 0.05$) .

The scar-to-blood CNR was found to be significantly higher in the dual-IR sequence with all $T1_{min}$ values compared to the IR sequence ($p = 0.013$, 0.009, 0.007 and 0.003 for $T1_{min}$ of 50, 100, 200 and 300 ms respectively) (Figure 5.13b) . The scar-to-myocardium CNR was however found to be significantly higher for the IR sequence compared to the dual-IR sequence for all $T1_{min}$ values ($p = 0.013$, 0.01, 0.033 and 0.02 for $T1_{min}$ of 50, 100, 200 and 300 ms respectively) (Figure 5.13c). Although reduced compared to the IR sequence, the scar-to-myocardium CNR in the dual-IR sequence is still probably adequate to differentiate the scar from normal myocardium. The blood-to-myocardium CNR was also found to be significantly higher in the IR sequence compared to the dual-IR sequence with all $T1_{min}$ values ($p = 0.001$).

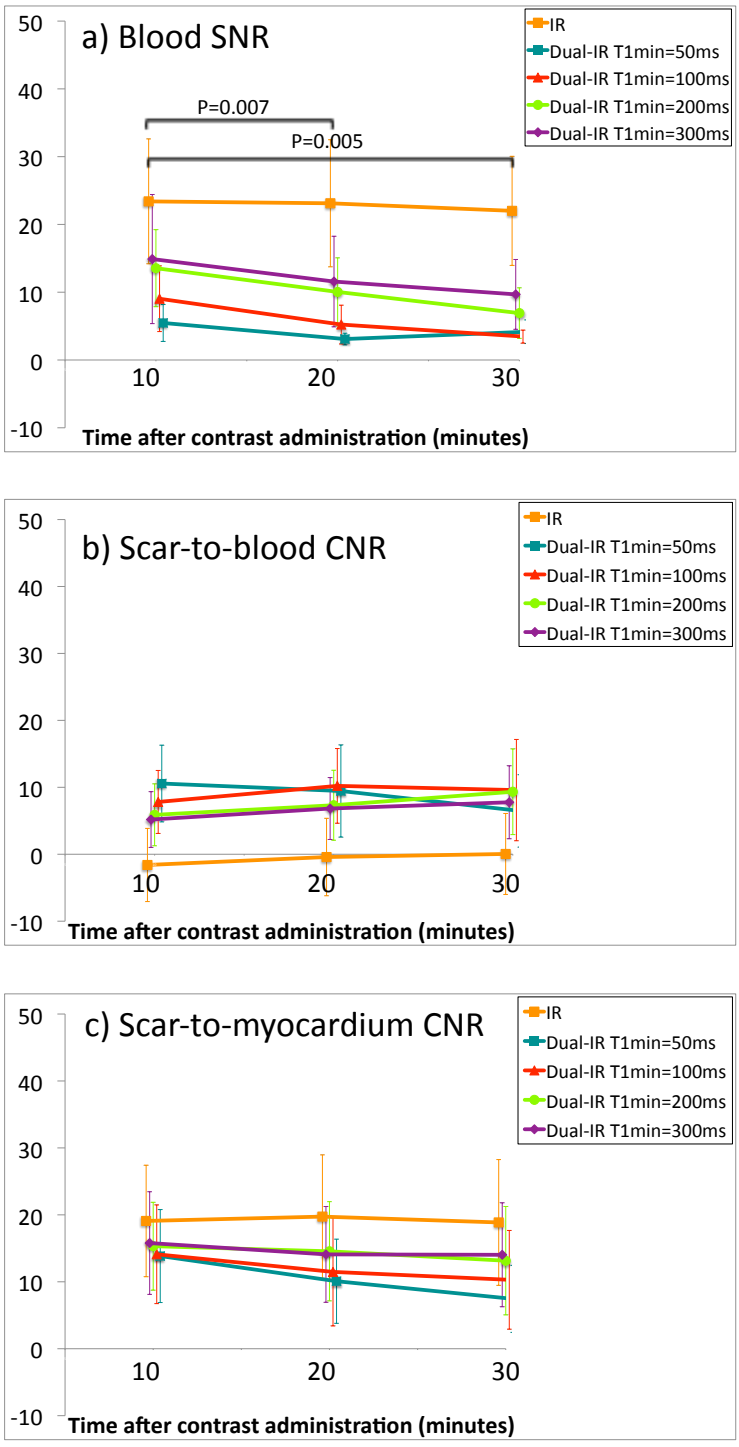

Figure 5-13: a) Blood SNR, b) scar-to-blood CNR, c) scar-to-myocardium CNR values calculated in short-axis IR and dual-IR images at the three different time points after contrast administration. Points are for each scan type at 10, 20 and 30 minutes post contrast administration but have been shifted slightly to improve visualization of the error bars. Significant differences between time points are displayed from one-way Analysis of Variance between groups (ANOVA) which considered all scan types together. A post-hoc Bonferroni test was performed to adjust for multiple comparisons.

5.4 *Discussion*

Simulation and phantom studies show that the dual-IR sequence allows signal suppression over a wide T1 range which can be adjusted by changing the $T1_{min}$ value. Preliminary patient data show improved scar-to-blood contrast, confidence scores for the presence of infarction and the extent of transmurality for the dual-IR sequence compared to the IR sequence. There was improved consistency between the two experts for assessment of scar size and extent of transmurality with the dual-IR sequence. The highest confidence scores were given to the dual-IR sequence with a $T1_{min}$ of 200 ms, which may be due to a combination of sufficient left ventricular blood reduction combined with good visualization of the myocardium. Shorter $T1_{min}$ values resulted in lower blood signal whereas longer $T1_{min}$ values provided higher blood-to-myocardium CNR which improved myocardium visualization and border definition.

The ability to differentiate irreversibly damaged from normal myocardium is a key advantage of MR over other imaging modalities. The assessment of transmurality and the detection of small sub-endocardial scar can be hindered by the poor scar-to-blood contrast in IR images. A new LGE MR sequence was recently described which employs an additional slice selective pulse to prepare the blood and myocardium magnetization differently in order to achieve black blood properties [37]. This relies on sufficient blood flow between the slice-selective and non-selective inversion pulses and it was found to work less reliably in patients with an ejection fraction of less than 40 % [37]. In addition, this approach still relies on the exact timing of inversion pulses to suppress the two individual T1 values of blood and of tissue.

The dual-IR sequence is a modification of the QIR sequence, which was developed to achieve T_1-independent blood suppression in carotid plaque imaging [29]. Whereas in the QIR sequence, the aim was to null only the blood signal, I have shown that the dual-IR sequence achieves blood and tissue signal suppression within the defined T1-range. It is not dependent on out-flow of blood from the imaging slice and should therefore be applicable to patients with low ejection fractions which is important for imaging patients with myocardial scar.

Papillary muscle enhancement has been linked to ventricular arrhythmias [101] and mitral regurgitation [102]. The depiction of papillary muscle scar such as in Figure 5.8d also seems to benefit from the reduced blood signal of the dual-IR sequence. I hypothesize that the dual-IR technique may also be useful in the imaging of diffuse fibrosis, amyloidosis or myocarditis where contrast uptake is more diffuse making the correct choice of TI often difficult. It may also aid the visualization of scar formation following radio frequency ablation procedures where differentiation of the scar from blood can be hampered by high blood signal in IR images.

This study successfully demonstrates proof-of-concept but consequently also has limitations. I only investigated 12 patients with a wide range of scar chronicity. Instead of covering the entire left ventricle, I only tested the sequence in a single slice with confirmed scar on the IR sequence. However, this approach minimized the time between the IR and dual-IR sequence in order to allow comparison of both sequences at different times points post contrast injection. I also used identical read-out parameters for the IR and dual-IR sequences to minimize the impact of the

imaging sequence on image contrast. In order to achieve an identical 12 second breath-hold for the IR and dual-IR images, the TFE factor and the acquisition time were approximately double for the IR images, which may have increased image blurring in some cases. SENSE acceleration, which could have been used to reduce the acquisition time, was not employed in order to allow an accurate calculation of the SNR and CNR values. The patients included in this study had heart-rates between 50 and 70 bpm. As the simulations showed that there is more signal suppression at higher heart-rates, I would recommend that for patients with a heart-rate >75 bpm the dual-IR pre-pulse is played out over the time period of two RR intervals. This would aim to produce signal characteristics that would be achieved at half the heart rate and should ensure the signal in the scar is maintained.

I have also only tested the dual-IR sequence using Gadovist with a dose of 0.2 mmol/kg. This is consistent with accepted international guidance for LGE imaging [85]. However, a lower dose may have produced less marked differences in blood signal between the two sequences especially at later time points after administration. The dual-IR technique also relies on the fact that the T1 of scar is below the T1 suppression range to ensure the scar itself is not suppressed. In this study, scar was never suppressed using the dual-IR sequence at any time point even with a $T1_{min}$ of 50 ms. Future work should include an investigation of different contrast agents, doses, field strengths and include a range of infarct ages. In order to make a direct comparison between the sequences, analysis of the transmurality, scar presence and scar size data was only performed on the 14 infarcts that were identified by both experts in all the images. In 4 patients, there were additional infarcts identified on either the IR or dual-IR images by one or both of the experts. In future work, the

sequence should be validated in a large animal study to allow testing of the accuracy of this technique. This would be useful to determine whether scars that were identified on IR images but excluded on the dual-IR images and vice-versa were present on histology.

Although there are a number of automated methods for scar size assessment, I decided to use manual segmentation to assess scar size. In an extension of this study, I could evaluate automated techniques like the FWHM or standard deviation models to quantify scar size in the dual-IR images.

In conclusion, I have developed a dual-IR sequence that achieves adjustable tissue suppression over a wide T1 range. Preliminary patient data show the dual-IR sequence results in an improvement in scar-to-blood CNR, higher expert confidence with regard to the presence of scar and the assessment of scar transmurality and more consistent assessment of scar size and transmurality between experts compared to the IR technique.

Chapter 6

6. Review of LGE MRI Techniques for Scar Visualization after RF Ablation for PVI

6.1 *Introduction*

LGE is a well validated technique for visualizing ventricular scar. Lardo et al (2000) first described the LGE effect in the right ventricle of a canine model following RF ablation [103]. Dickfeld et al (2006) then studied the formation of lesions in the epicardium of dogs up to 12 hours after RF ablation [104]. There was also a case of ventricular scarring reported in a patient who had undergone previous RF ablation for idiopathic LV tachycardia [105]. This led to studies investigating whether the LGE may be useful for visualizing areas of atrial scar in patients who have undergone RF ablation for arrhythmia.

There are several additional challenges when applying the LGE technique to atrial scar. Firstly, the atria are up to five times thinner than the myocardium. This means that improved spatial resolution and excellent respiratory and cardiac motion compensation are required. Secondly, the ultimate clinical aim is to overlay the LGE scar distribution onto a 3D anatomical model of the atria and PVs created from MR angiography images and to compare this with 3D maps of EP data. A 3D acquisition is therefore preferred with improved through plane spatial resolution so thin contiguous slices can be reconstructed and a 3D map of the scar can be reformatted. Thirdly, as the pulmonary anatomy is complex and varies between individuals, it can be difficult to use the expected anatomy to differentiate scar from blood and normal atrial wall. There must therefore be high image contrast between scar and atrial wall and between scar and blood. Fourthly, the patients are being treated for arrhythmias which present challenges for all ECG-triggered MR sequences. This chapter will describe the main studies using MR-LGE imaging in the atria following RF ablation.

6.2 *3D IR Sequence*

Peters et al (2007) performed LGE MR imaging on patients before and after pulmonary vein isolation (PVI) procedure using RF ablation [25]. The sequence used in this study has become the standard approach for LGE atrial scar imaging. It was adapted from 3D LGE sequences used for the myocardium and coronary arteries [106, 107]. Whereas a 2D acquisition only excites a single slice, a 3D acquisition excites an entire volume. The 3D volume is spatially encoded with phase encoding along two orthogonal directions and frequency encoding along the third. The raw data is collected in a 3D k-space, which is then reconstructed using a 3D Fourier transform. The 3D acquisition thus allows thin contiguous slices to be reconstructed, which are ideal for visualizing LGE in the atrial wall and PVs. However, because phase encoding is performed along two axes, the scan time is prolonged with 3D acquisitions. On the other hand, the SNR is improved for a 3D acquisition compared to a 2D acquisition with the same spatial resolution.

A TR_{eff} of 1 heartbeat is used which allows less time for T1 recovery between heartbeats but reduces the overall scan time. A flip angle of 15 - 25 ° is used to minimize the effect of the read out on the image contrast. In order to visualize the thin atrial wall, the acquired voxel size is 1.3 x 1.3 x 5 mm, which is then reconstructed to 0.6 x 0.6 x 2.5 mm. Fat suppression is used to suppress the signal from epicardial fat.

6.3 *Cardiac and Respiratory Motion Compensation*

In order to reduce the artifacts caused by cardiac motion, a balanced steady state free precession (b-SSFP) cine image is usually used to ascertain the period in the cardiac cycle when the atria are most still. As this varies with the patient's heart-rate, it is performed on an individual basis. The trigger delay and acquisition window are set to perform image acquisition during this quiescent period.

As the 3D LGE scan time is far too long for a breath-hold, a respiratory navigator is required. A navigator is performed by exciting a cylindrical beam of tissue perpendicular to the liver-lung interface. The k-space data acquired from this beam are then reconstructed using a 1D Fourier transform [108]. The data are normally

acquired just before image acquisition and provides a measurement of the diaphragm position in the superior-inferior direction (Figure 6.1). In order to reduce the artifacts caused by respiratory motion, an acceptance window around end-expiration is defined and only the image data acquired at this respiratory phase are reconstructed. A wider acceptance window will result in more data being accepted and a shorter scan time however it could also increase motion artifacts. In general, an acceptance window of 5-7 mm is employed, which results in a scan of 5-10 minutes.

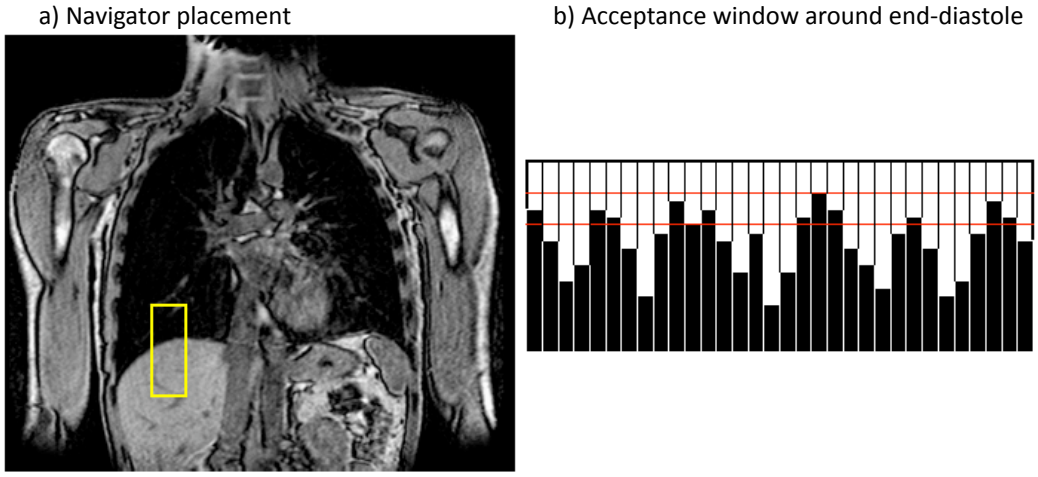

Figure 6-1: Respiratory navigator placement over the liver-lung interface (left) and the definition of an acceptance window to only reconstruct data at end expiration (right).

In order to detect the position of the liver-lung interface, there must be sufficient signal in the liver at the time when the navigator data is acquired. If an inversion pre-pulse has been employed, this can suppress the liver signal which can hamper navigator detection. Therefore when the IR-TFE is combined with a navigator, a restore pulse is applied immediately after the inversion pulse, which restores the signal in an area slightly larger than the area of the cylindrical beam navigator (Figure 6.2) [109]. This restores the magnetization within that region and means there will be sufficient signal for navigator detection.

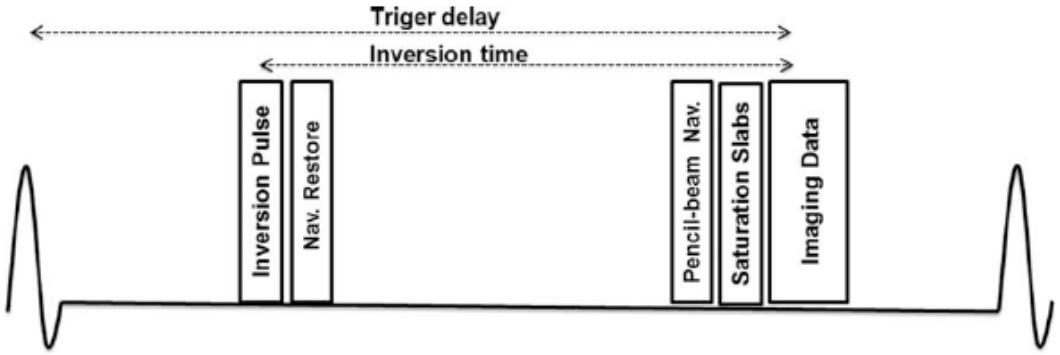

Figure 6-2: The navigator restore pulse is applied to ensure sufficient navigator signal when IR-TFE imaging is combined with a respiratory navigator [38].

Although the restore pulse improves navigator detection, it also has an undesired effect. The restore pulse can re-invert the signal of blood in the PVs. By the time of image acquisition, this blood may have flowed into the PV ostia and atria. This can cause bright signal in the PVs and atria and can hamper the detection of scar (Figure 6.3). In addition, there is often a circle of bright signal where the navigator restore pulse was applied, which affects the dynamic range of the image. This means the brightest signal will be in the area of the navigator restore and any LGE areas in the atria will not be as bright and therefore be harder to distinguish from normal atria and blood.

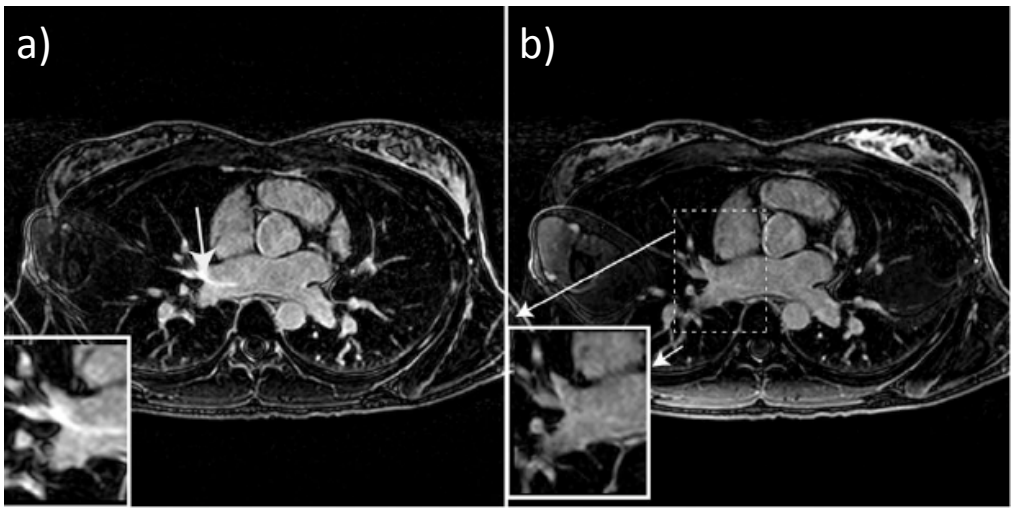

Figure 6-3: The PV in-flow artifact caused by the navigator restore pulse [38].

There have been several approaches aimed at reducing the PV in-flow artifact. Firstly, respiratory bellows can be used as alternative method of respiratory gating. Peters et al (2011) compared respiratory navigation with bellows and found that the bellows removed the PV in-flow artifact and there was no significant difference in image sharpness or ghosting [110]. However, this was a pilot study on only nine subjects and not all centers have bellows available for clinical use.

Hedjazi-Moghari, et al (2010) implemented an alternative approach where the restore pulse after the inversion pre-pulse is taken out, which removes the high signal in the liver and the PV in-flow artifact [38]. They also replaced the pencil beam navigator with a projection navigator, which is less sensitive to off-resonance effects. In order to achieve sufficient signal in the liver, a delay must be inserted between the navigator acquisition and image acquisition (Figure 6.4). The delay between the projection navigator and image acquisition should be long enough in order to obtain sufficient signal in the liver. They performed a pilot study on five subjects where they performed a Look Locker scan to measure the liver signal with variable inversion times. They found that a delay of 100 ms provided sufficient liver signal for navigator detection. The disadvantage of this approach is that the diaphragm position is measured 100 ms before the image acquisition, which precludes the use of motion tracking and thus has the potential to induce residual motion artifacts. In this study on 18 subjects however they found no statistically significant difference between subjective motion scores artifacts between the "restore" and "no restore" approaches.

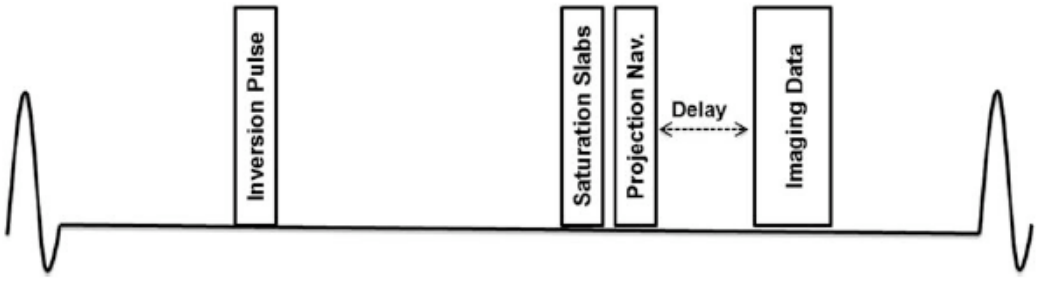

Figure 6-4: The sequence design for with navigator restore a projection navigator and a delay before imaging [38].

Badger et al (2010) used an alternative approach to reduce the effect of the PV in-flow artifact. They performed a 'trailing navigator', which is performed directly after

image acquisition by which time the magnetization in the liver has achieved sufficient recovery to allow navigator detection [27].

6.4 *Contrast Agents and Timing of Image Acquisition*

In order to visualize areas of scar, the signal from normal atrial wall and blood should be suppressed. In the IR-TFE sequence, the inversion time, TI, is usually set to null the signal from normal myocardium using a preceding Look Locker scan. This makes the assumption that the normal atrial wall has the same T1 value as normal myocardium [25]. An alternative approach would be to choose the TI to null the blood signal but this may result in suboptimal nulling of the unscarred atrial wall.

There have been several studies which perform LGE imaging with the 3D IR-TFE technique using different contrast agents and timing. Some have used a single dose of Multihance and performed LGE imaging at 15 minutes post-contrast administration [26, 27, 111, 112]. One study used a dose of 0.15 mmol/kg of Magnevist and imaged at 15 minutes post contrast administration [113]. Those studies that used a double dose of Magnevist imaged at 15 to 25 minutes after administration [25, 114-116].

When designing the best protocol for 3D-IR-LGE imaging, it is desirable to wait until the T1 of the blood is sufficiently longer than that of scar so that the IR-LGE technique will result in good scar-to-blood contrast. Goldfarb et al (2009) and Klein et al (2004) suggested that for a double dose of Magnevist, a time delay of more than 15 minutes is required to ensure sufficient scar to blood differentiation [86, 87]. The drawback of imaging after 20 - 25 minutes is a longer total scan time and decreased patient throughput.

6.5 *Data Analysis*

In order to relate the scar seen on LGE images to patient outcome, it is useful to quantify the total amount of scar and scar thickness and to assess the circumferential extent of scar around a PV. This section will outline some of the approaches to scar quantification and assessment, which are based either on manual contouring or computerized scar detection or a mixture of the two.

6.5.1 Quantification of Scar Extent

The methods used for the quantification of scar extent are based on studies performed on ventricular scar after MI (described in section 4). McGann et al (2008) and Badger et al (2010) measured the extent of injury using a threshold based algorithm. Firstly, the contours of the epicardial and endocardial borders were manually defined to confine the analysis to the LA wall. Injured tissue is then defined as three standard deviations above the mean pixel signal intensity in normal atrial wall.

Peters et al (2009), did not use contouring to exclude the blood pool but instead employed a user defined threshold, which was optimized on a patient by patient basis. The minimum threshold that eliminated most blood pool was chosen. After thresholding, isolated high signal pixels were removed. The authors accept that his user dependent approach adds subjectivity to the analysis but report good inter and intraobserver agreement in a previous study [116].

6.5.2 Circumferential Extent

As the RF ablation procedure aims to isolate the PVs, the circumferential extent of scar is a potential measure of how well the PV has been isolated. In Peters et al (2009), an expert was asked to estimate the circumferential extent to the nearest 5 % in maximum intensity projected (MIP) images [114]. This allowed them to visualize scar in an image of the cross-sectional of the ostia of the PV.

6.5.3 Scar Thickness

The thickness of scar is thought to be linked with the efficacy of the ablation. It is however a difficult parameter to accurately measure as the atrial walls are very thin. In Peters et al (2009), scar thickness was measured using line profiles perpendicular to the septum [114]. A significant inverse relationship was found between thickness of enhancement and the number of days after ablation procedure.

Although the technique described in McGann is automated, it still requires the user to define the scar-blood border to exclude the blood signal. Although the technique used by Peters et al (2009) does not exclude the blood pool analysis; it means that the blood must have a lower signal than scar for the borders to delineated by hand or

by threshold technique. Equally when measuring the thickness of scar and the circumferential extent, the inclusion of blood pixels as scar will lead to a misleading result.

6.6 *Correlation of Atrial LGE with Arrhythmia Recurrence*

McGann et al (2008) performed LGE imaging before and three months after RF ablation for PVI in 46 patients with AF [26]. Arrhythmia recurrence correlated with the degree of wall enhancement. LGE was not seen in any of the pre-ablation scans whereas it was seen in all post-ablation scans. Patients with minimal scar were found to have lower success of the procedure than those with moderate scar (Figure 6.5).

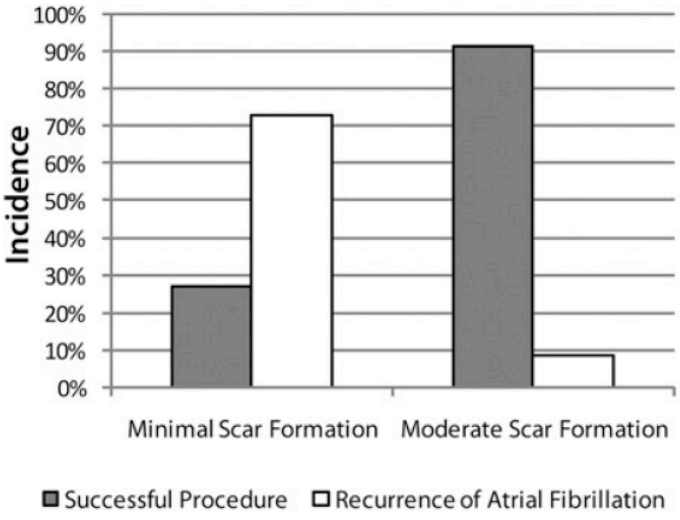

Figure 6-5: Association between post procedure AF recurrences and the extent of atrial wall scar [26].

Peters et al (2009) performed a similar study investigating the relationship between the recurrence of (AF) and the extent of LGE after the PVI procedure [114]. They performed LGE imaging 46 ± 28 days after RF ablation around each PV ostium in 35 patients with AF. They found that patients without recurrence had more completely circumferentially scarred veins based on a qualitative measurement of scar extent. Patients without recurrence also more frequently had scar in the inferior region of the right PV. The quantitative measure of the volume of scar was greater in patients without recurrence. Badger et al (2010) performed a more extensive study on 144 patients who underwent RF ablation for AF and LGE imaging after 3 months

[27]. They found that the number of PVs with complete circumferential scarring and the total left atrial scar was significantly higher in patients with a better clinical outcome.

6.7 *Correlation of LGE Atrial Scar with EP Data*

Taclas et al (2010) performed a study to compare the post procedural LGE scar in 19 AF patients with the intended sites of RF ablation [115]. They performed a rigid registration of the LGE scar data with the Carto data which is an EP mapping technique which shows the locations of intended ablation points in relation to the PV and atrial anatomy. They then measured the distance between the Carto points with the nearest scar. They found that although there was a correspondence between the Carto points and the scar, for 20 % of the Carto ablation sites there was no visible corresponding scar. They found that those with recurrent AF had significantly more gaps in the left inferior PV. As it is difficult to determine the efficacy of each ablation point during the procedure, they speculated that LGE scar imaging may help to evaluate which ablation points have been ineffective.

6.8 *Use of LGE Atrial Scar to Plan Repeat RF Ablations*

Reddy et al (2008) reported on a case of a patient who had multiple unsuccessful ablations for AF/AFL [117]. They found that the regions devoid of scar on LGE images corresponded to the sites with early electrical activation. After these areas were ablated, electrical PV reconnection did not occur and the patient remained free of AF and AFL. Badger et al (2010) performed a more extensive study on 144 patients, 18 of which underwent a re-ablation procedure [27]. They found that the LGE shown at 3 months after the initial RF ablation correlated with the EP data during the 2nd procedure (Figure 6.6). In those patients who had a second re-ablation procedure, the gaps in the LGE pattern were identified and used to target the second ablation procedure. In one patient, all four PVAs had incomplete isolation. After the second ablation procedure, there were circumferential lesions around all four PVAs (Figure 6.7).

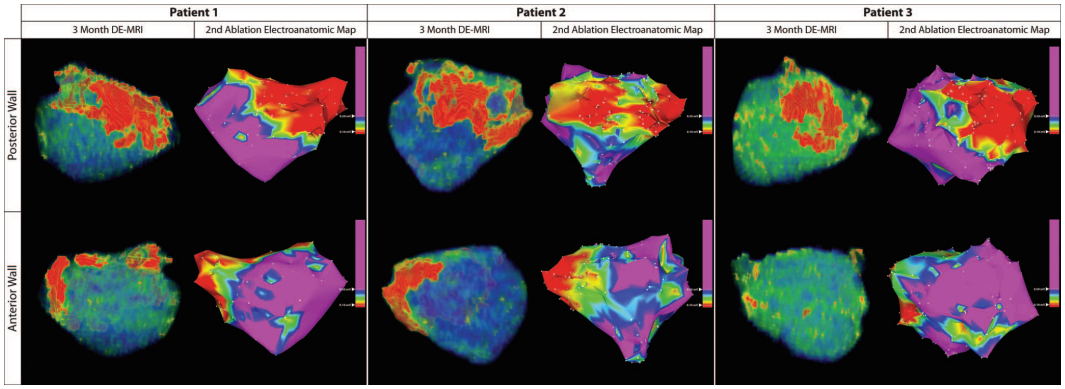

Figure 6-6: Correlation between LGE-MRI after a failed ablation procedure with the EA map obtained during the repeat procedure for 3 patients. The images on the left demonstrate PA (top) and AP (bottom) views of the DE-MRI color model scar patterns. The images on the right are the EA map obtained during repeat procedure. There is a strong correlation in the size and distribution of MRI scar (red tissue) with low-voltage regions (0.1 mV; red) of the EA map [27].

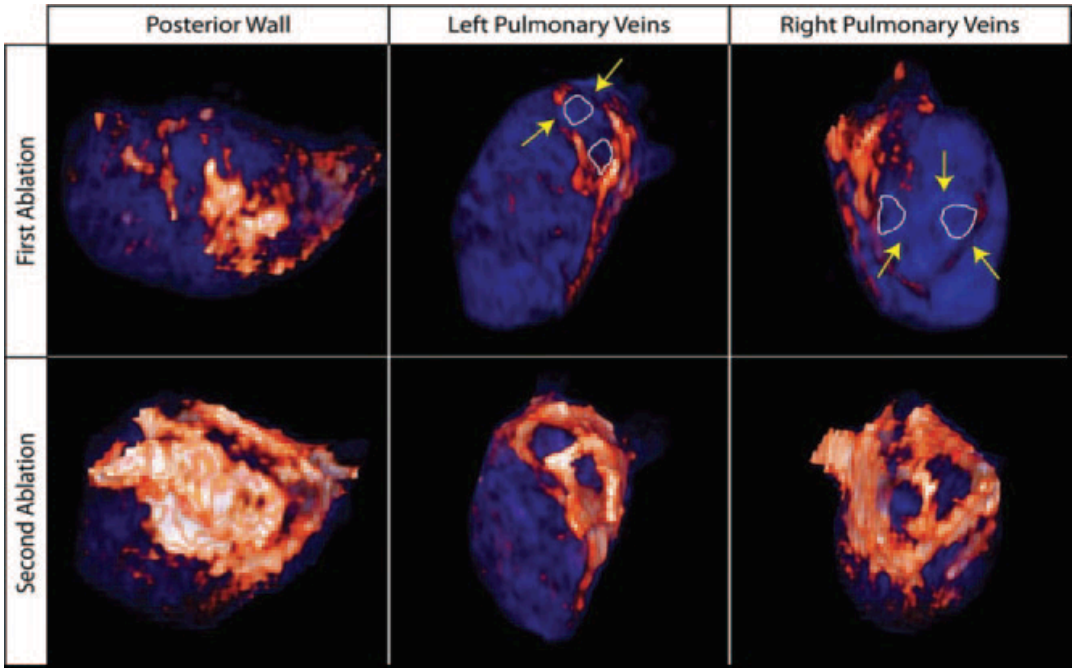

Figure 6-7: 3D MRI model of the LA after failed PVA isolation (First) and repeat successful PVA isolation (Second). After the initial failed ablation, all 4 PVs showed incomplete PVA scar as evident by lack of continuous scar (orange/white) around each PV ostia (white outline). Gap lesions of healthy myocardium (blue) were identified and targeted (yellow arrows) before repeat ablation. After the successful repeat procedure, all 4 PVA had continuous scar lesions.

6.9 *Summary*

In summary, the 3D IR-TFE sequence has been used to image LGE in the PVs and atrial wall after RF ablation for AF. It has been shown to correlate to likelihood of procedural success and been used to guide repeat procedures. However, as with ventricular scar imaging, there can be high blood signal in the IR images which can hamper the detection of these very small lesions. This means that imaging is often performed later after contrast administration which extends the overall scan time. This motivates the work in the next chapter to evaluate whether the dual-IR sequence can improve blood suppression and scar detection and allow imaging earlier after contrast administration.

Chapter 7

7. Dual-IR Pre-pulse for LGE imaging of RF Ablation Lesions after PVI for AF

7.1 *Introduction*

7.1.1 Scar Imaging

A good correlation has been found between the extent of LGE in atrial scar using the IR technique and the outcome in patients who have undergone PVI using RF ablation for AF [114]. However, scar visualization can be hampered by strong residual blood signal. Therefore imaging is often performed at least 25 minutes after contrast administration to ensure the contrast agent has cleared from blood [86]. Chapter 5 described how the dual-IR pre-pulse was shown to improve blood suppression in LGE images of myocardial scar. In this chapter I describe a study to assess whether the dual-IR pre-pulse improves blood suppression in LGE atrial scar imaging and whether it allows imaging earlier after contrast administration.

7.2 *Methods*

7.2.1 Pulse Sequence

The standard 3D free breathing, respiratory-navigated, ECG-triggered GE sequence was employed on a 1.5 T Achieva MRI scanner (Philips Healthcare, Best, The Netherlands) [114]. Image acquisition was timed with the minimal atrial motion using a preceding balanced steady state free precession (bSSFP) cine image. Imaging parameters included: TE / TR = 2.6 / 5.4 ms, navigator window = 5 - 7 mm, flip angle = 25 °, voxel size = 1.2 x 1.2 x 4 mm (reconstructed = 0.6 x 0.6 x 2 mm). The

sequence was combined with the traditional IR pre-pulse with the TI set to null normal myocardium using a preceding Look Locker scan.

The sequence was also combined with the dual-IR pre-pulse. As for the myocardial scar imaging described in chapter 5, it consisted of two non-selective inversion pre-pulses separated by two time delays TI1 and TI2. The optimal suppression range was found to be 200 - 1400 ms or 300 - 1400 ms in the infarct study. Therefore in the atrial scar patients, the TI1 and TI2 delays were optimized to achieve signal suppression in a T1 range of 250 - 1400 ms according to the heart-rate. In the infarct study, all the patients had heart-rates in the range of 50 to 70 bpm. The atrial scar patients had a wider range of heart-rates. From the results of simulations and phantom studies in chapter 5, it was clear that for heart-rates ≥ 80 bpm, the dual-IR sequence results in greater suppression of shorter T1 species (Figure 7.1). It is therefore possible that the scar signal will be suppressed in the dual-IR sequence at high heart-rates.

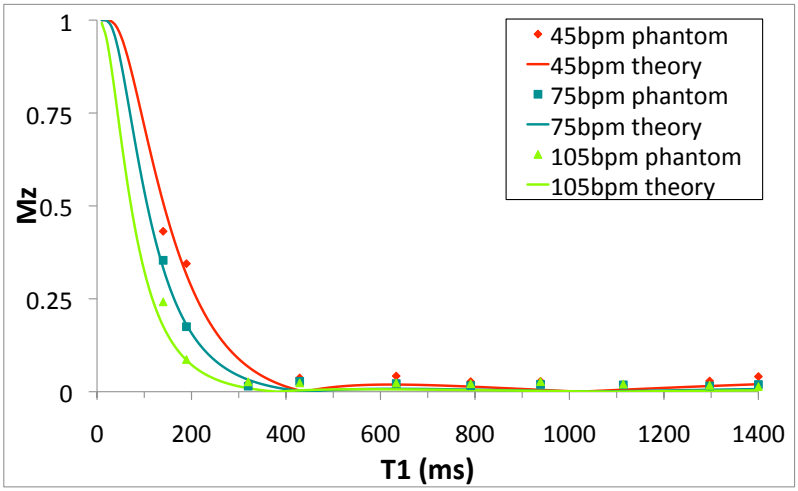

Figure 7-1: Simulations and phantom measurements of M_zb versus T1 value for $T1_{min}$ = 250 ms for different heart-rates showing greater signal suppression of short T1 species at higher heart-rates.

In the dual-IR sequence, it was decided therefore to apply the GE read-out every two heartbeats in patients with heart- rates ≥ 80 bpm. For example, in a patient with a heart-rate of 90 bpm, the TI1 and TI2 delays were optimized for a heart-rate of 45 bpm and the two inversion pulses are played out during the time of two RR intervals (Figure 7.2). The IR-TFE sequence on the other hand was applied every heartbeat in all patients according to the clinical protocol.

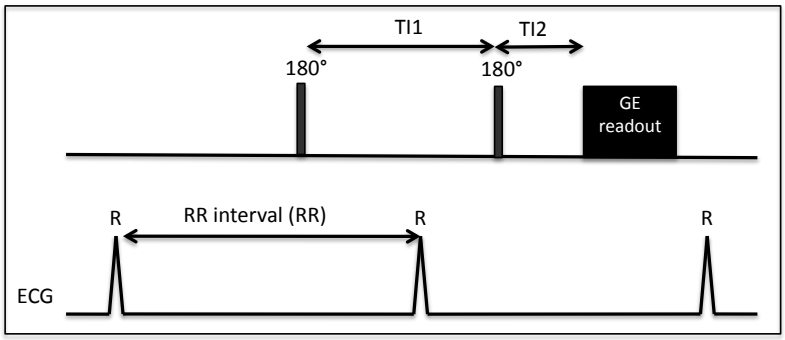

Figure 7-2: The dual-IR pulse sequence applied with the two inversion pulses distributed over two heartbeats for high heart-rates.

7.2.2 Implementation of an Alternative Navigator Sequence

As described in chapter 6, Moghari et al described an alternative navigator strategy to remove the PV in-flow artifact [38]. I implemented this strategy using a pencil beam navigator and combined this with the IR and dual-IR pre-pulses. It was tested in one patient 25 - 30 minutes after contrast administration using the IR-TFE sequence described above by scanning with and without the navigator restore to compare the presence of the PV in-flow artifact. It was then applied in all of the following patient studies.

7.2.3 Patient Studies

Thirteen patients (10 male, age 57 +/- 10yrs) underwent MR imaging using a 1.5 T clinical MR scanner (Philips Healthcare, Best, the Netherlands) approximately 3 months following RF ablation for AF. This study was performed at 1.5 T as it was

part of an existing study at this field strength. Imaging was performed after 0.2 mmol/kg of gadopentate dimeglumine (Magnevist, Bayer Schering AG, Berlin) was administered. Dual-IR-TFE imaging was performed at 15, 20 and 30 minutes and compared to standard IR-TFE imaging at 25 minutes. To perform a direct comparison of the IR and dual-IR pre-pulses, in one patient imaging was performed with the IR sequence at 15, 20, 30 and 40 minutes after contrast administration and then repeated in the same patient in a second scanning session using the dual-IR sequence at the same time points.

7.2.4 SNR and CNR Measurements

Regions of interest were manually defined in 5 slices in the blood and right superior PV scar in all images. Blood and scar SNR and scar-to-blood CNR values were measured using Osirix software.

7.2.5 Scar Quantification

For each 3D image set, two readers both with at least 2 years experience in cardiac MRI (James Harrison and Zhong Chen) manually segmented areas of late enhancement around the PVs and left atrium. The total scar size was measured using ITK-SNAP Medical Image Segmentation software (http://www.itksnap.org) [118].

7.2.6 Statistical Analysis

The SNR and CNR values were compared using a paired t-test between the IR sequence at 25 minutes and the dual-IR images at 15, 20, and 30 minutes post contrast administration.

7.3 *Results*

7.3.1 Implementation of a New Navigator Sequence

LGE images using the IR sequence combined with standard navigator was found to generate the pulmonary in-flow artifact (small arrow in Figure 7.3a). It also

displayed high signal in the liver (large arrow in Figure 7.3c) which affects the dynamic range of the images and can make it more difficult to visualize scar in the atrial wall Images in the same patient with the navigator restore removed and a delay inserted between the navigator and imaging were found to remove the pulmonary in-flow artifact (7.3b) and the bright signal in the liver due to the navigator restore (7.3d)

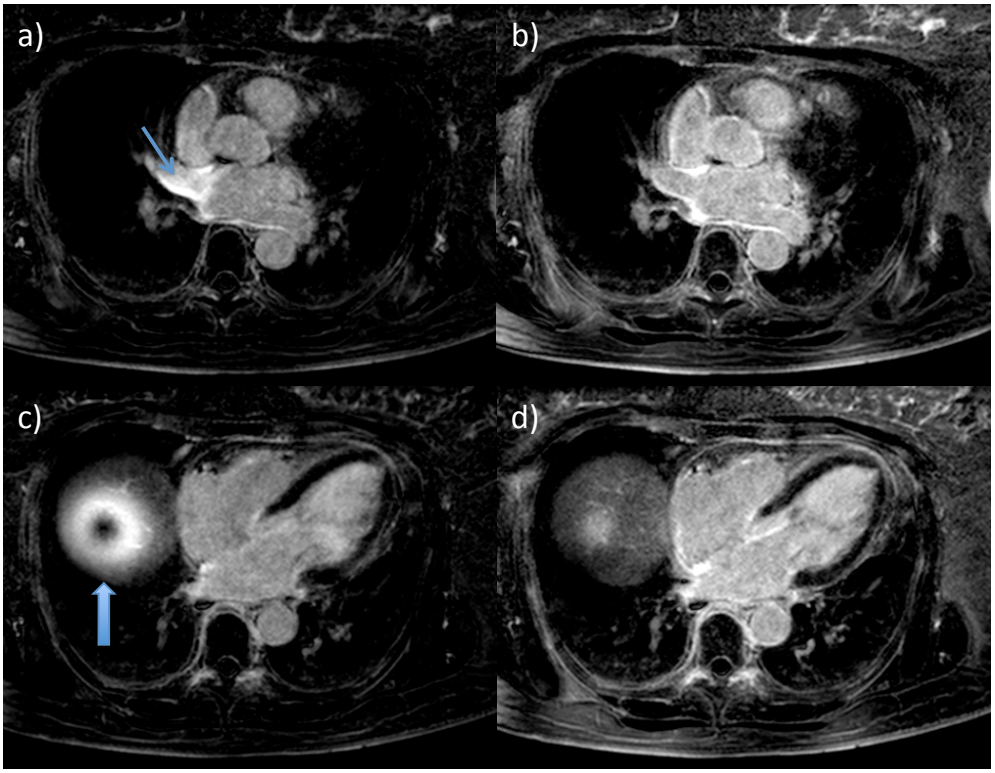

Figure 7-3: LGEimages using the IR sequence combined with standard navigator (a and c) and images in the same patient with the navigator restore removed and a delay inserted between the navigator and the imaging read-out (b and d).

7.3.2 Patient Studies

Dual-IR-TFE images achieved superior blood suppression at an earlier time point compared to IR-TFE images (Figure 7.4). Images in the same patient taken in two separate scanning sessions show that the dual-IR pre-pulse achieves improved blood suppression compared to the IR pre-pulse at identical time point (Figure 7.5).

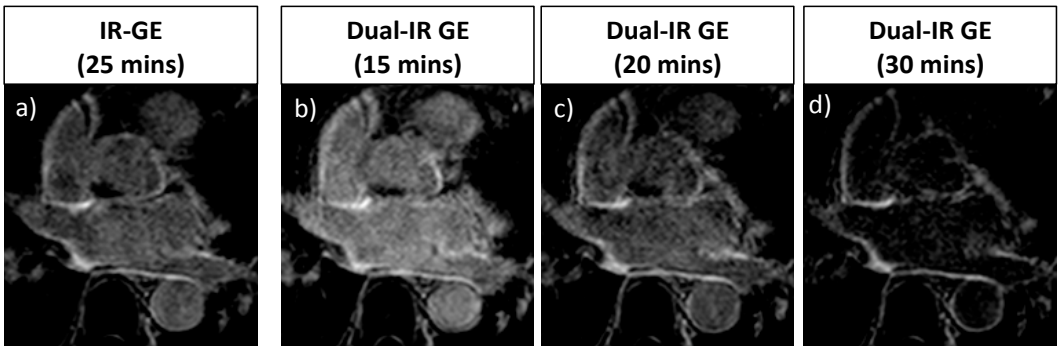

Figure 7-4: LGE images of atrial scar in a 66-year-old female patient: IR imaging at a) 25 minutes and dual-IR imaging at b) 15 minutes, c) 20 minutes and d) 30 minutes after contrast administration. All images have identical windowing.

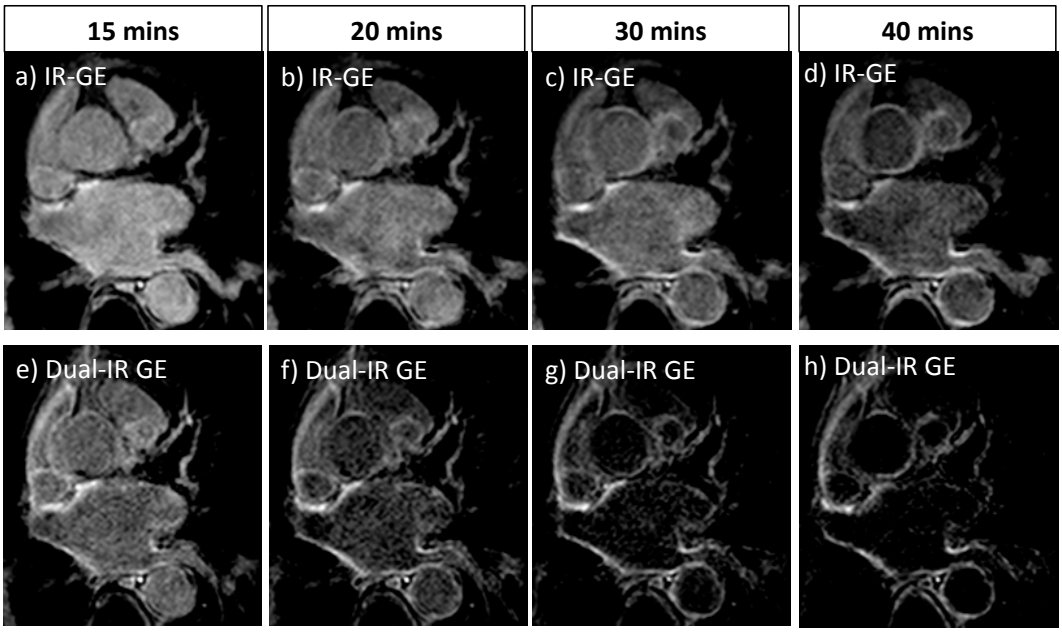

Figure 7-5: LGE images of atrial scar in a 68-year-old male patient taken during two separate scanning sessions. Images from the first scanning session using the IR-TFE sequence at a) 15 minutes, b) 20 minutes, c) 30 minutes and d) 40 minutes after contrast administration Images from second scanning session using the dual-IR GE sequence at e) 15 minutes, f) 20 minutes, g) 30 minutes and h) 40 minutes after contrast administration. All images have identical windowing.

7.3.2 SNR and CNR Measurements

Blood SNR values were significantly reduced at all time points in the dual-IR images compared to IR images at 25 minutes (Figure 7.6a.) whereas there was no significant

difference in scar SNR (Figure 7.6b.). Scar-to-blood CNR values were significantly improved with dual-IR after 30 minutes compared to IR at 25 minutes (Figure 7.6c).

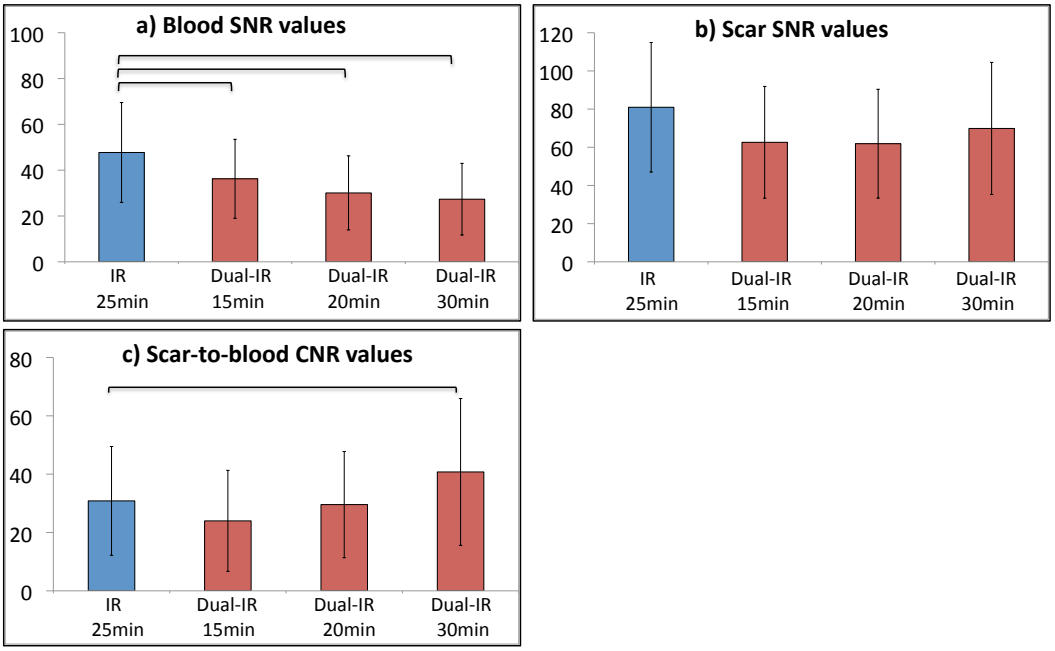

Figure 7-6: Blood SNR, b) scar SNR and c) scar-to-blood CNR measurements for IR and dual-IR images. Horizontal bars indicate statistical significance in a paired t-test $p<0.05$.

7.3.3 Scar Quantification

There was no statistically significant difference between the scar size between the IR at 25 minutes and dual-IR images at 20 minutes for either observer. Bland Altman plots and correlation plots show an improved interobserver variability for total scar measurements for the dual-IR sequence at 20 minutes compared to the IR sequence at 25 minutes (Figure 7.7).

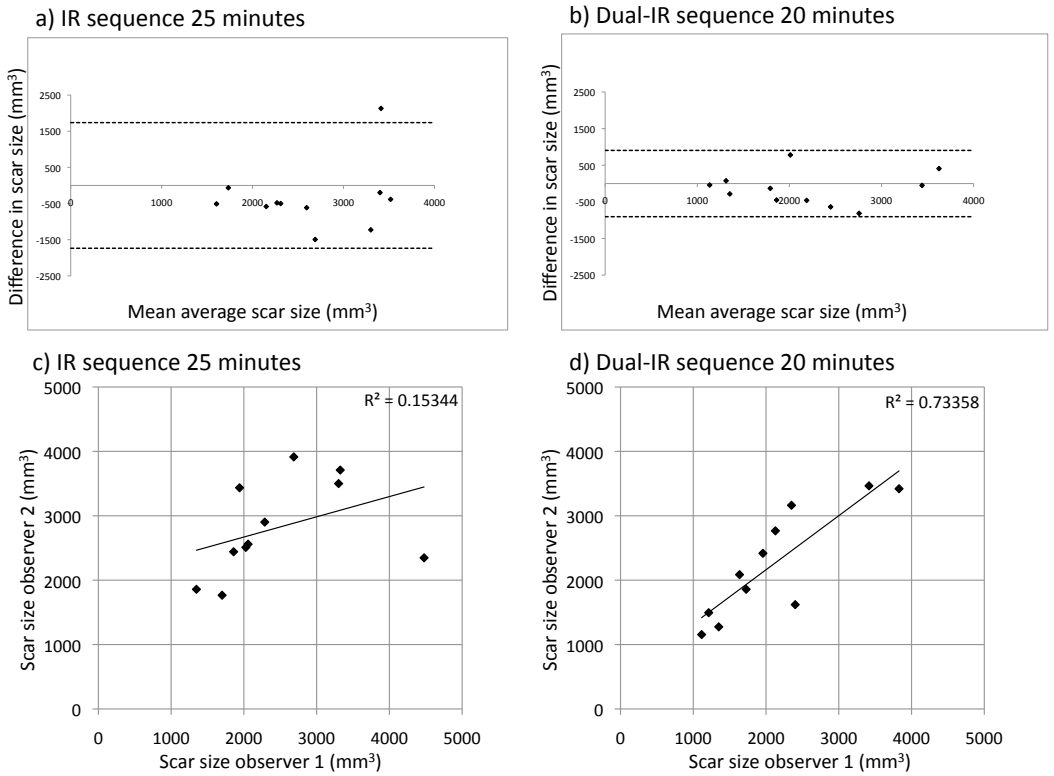

Figure 7-7: Bland Altman plots for total scar measurements (mm³) for a) the IR sequence at 25 minutes and b) dual-IR sequence at 20 minutes. Correlation plots for c) the IR sequence at 25 minutes and d) dual-IR sequence at 20 minutes.

7.4 *Discussion*

RF ablation strategies have evolved from ablating anywhere within the PV to wide encircling lesions around the PV antrum and additional RF energy applications targeting anatomic areas and EP parameters.[119] Despite this, single procedure success rates are modest, suggesting that the factors which contribute to acute electrical isolation are not well understood.[120] LGE imaging using the IR sequence has been used to visualize and quantify post-procedural RF lesions in vivo. It has also recently been used to guide repeat procedures and identify gaps between areas of previous ablation.[27] The dual-IR technique improves visualization of left atrial LGE areas with improved atrial blood pool suppression and better definition of the edges and boundaries of DE areas.

The dual-IR technique achieves improved blood suppression and an improvement in the inter-observer variability in scar size quantification. As imaging can be performed earlier, it also has the potential to reduce the overall scan time which may improve patient compliance and optimize resources. The traditional IR method requires a Look Locker sequence to calculate the optimum inversion delay to ensure optimum nulling to visualize areas of LGE. The dual-IR sequence mitigates this step as the inversion delays are automatically calculated according to the patient's heart-rate. The combination of the dual-IR sequence with the new respiratory navigator implementation, removed the PV artifact which can hamper the visualization of scar.

The patient sample size was small so it can only be considered a proof-of-concept study. In addition, all the patients were in sinus rhythm so it would be useful to also examine the image quality in patients in AF. As future work, the extent of scar measured in the dual-IR and IR images could also be correlated with the recurrences in these patients to determine which sequence is better at predicting procedural success. An animal model could also be used to see if the dual-IR sequence produces a more accurate map of the scar by comparing to histology.

In conclusion, dual-IR improves blood suppression in LGE imaging and improves the visualization of scar contour definition and has potential to reducing image acquisition time.

Chapter 8

8. Conclusions

Cardiovascular MRI employs many different pulse sequences to provide morphological and anatomical information and to characterize disease. Although it has a variety of endogenous contrast mechanisms, gadolinium based contrast agents are often used to improve the conspicuity of disease. LGE imaging can be performed to visualize some components of atherosclerotic plaques. It is hoped that eventually this will be used as a screening tool to help differentiate vulnerable from stable plaques. Arguably, the most important application of LGE imaging is for the visualization of myocardial scar after MI. It is a well established technique which can determine the presence, extent and transmurality of scar. This was shown to help predict the likelihood of functional recovery after revascularization therapy. More recently, LGE imaging has been used to visualize atrial wall scar in patients who have undergone RF ablation therapy for AF. It was found that the extent of scar in the atrial wall correlated with procedure success and that the LGE pattern could be used to plan re-do ablation procedures. The aims of this work were to develop, optimize and test novel MRI pulse sequences for LGE imaging of the aortic vessel wall and myocardial and atrial wall scar.

Traditionally the DIR sequence has been used to achieve black blood images of the vessel wall. In the DIR sequence, blood only experiences one non-selective inversion pulse which means that there is one inversion time which can be optimized to suppress blood signal resulting in the nulling of only one specific T1 value. When imaging is performed after contrast administration, the TI delay must be shortened to

achieve blood suppression. The correct determination of TI is therefore user-dependent and requires a Look Locker scan. The QIR sequence works on the principal that two inversion pulses with two delay times can be optimized to achieve blood suppression both before and after contrast administration using identical imaging parameters. The original implementation of the QIR sequence was applied to the carotid arteries and did not employ ECG-triggering [29]. To use the QIR sequence to image the aorta, I hypothesized that as there is variable flow during the cardiac cycle, the QIR sequence should be combined with ECG-triggering. I therefore had to optimize the TI1 and TI2 delays according to the patient's heart-rate. I also tested two types of ECG triggering in 10 volunteers which showed that the TI2 delay must be timed to coincide with systolic flow in the aorta to achieve sufficient out-flow and blood suppression. I also found that the QIR sequence could be combined with zoom imaging to accelerate the image acquisition. The modification of the QIR pre-pulse means that the sequence can now be successfully employed in vessels which have variable flow or motion during the cardiac cycle.

LGE imaging using the IR sequence is routinely used to visualize myocardial scar. Because the IR sequence only nulls the signal from one T1 species (the normal myocardium), there is often remaining signal in the blood pool. If the blood signal is sufficiently high, it can sometimes be difficult to distinguish scar from the adjacent blood pool particularly for subo-endocardial or small areas of scar. As was shown in my work to optimize the QIR sequence, two inversion pulses separated by two delays can be optimized to achieve signal suppression in a wide T1 range. I thus decided to apply this principle to LGE imaging of myocardial scar. I developed the dual-IR sequence and optimized the TI1 and TI2 delays to achieve signal

suppression in different T1 ranges: 50-1400 ms, 100-1400 ms, 200-1400 ms and 300-1400 ms. I tested this sequence in 12 patients with myocardial scar and found improved blood suppression and scar-to-blood CNR using the dual-IR sequence compared the traditional IR sequence. I also found that there was improved inter-observer variability for the manual assessment of transmurality and scar size.

In the third study, I evaluated the dual-IR sequence for the visualization of atrial scar in 13 patients who had undergone RF ablation for AF. I found that the dual-IR sequence with a $T1_{min}$ value of 250 ms improved blood suppression compared to the IR sequence with TI optimized to null normal myocardium. I also found that the dual-IR sequence improved the inter-observer variability of scar size measurements and enabled imaging earlier after contrast administration.

I aimed to develop novel MRI sequences for LGE imaging which involved theoretical simulations, phantom experiments, volunteer and patient studies to optimize and test the new sequences. I have demonstrated that the novel QIR implementation and dual-IR sequence are robust and applicable to several different cardiovascular diseases. The initial results in volunteers and patients show that the new sequences improve blood suppression and the conspicuity of contrast uptake. Future work will be focused on performing large animal studies to validate the images against histology.

9. Acknowledgments

I have learned so much over the last three years. Most importantly to persevere and then to accept that it doesn't have to be perfect. Firstly I'd like to thank René who has been a very calm and encouraging supervisor. I have enjoyed how he has trusted me and allowed me to pursue my own ideas. Thank you also to Tobias for all his advice and enthusiasm. It takes so much hard work and self-belief to do a Ph.D. and I couldn't have done it without your consistent support.

Thank you to the British Heart Foundation and the Welcome Trust for funding my work. Thank you to Tarique, Geraint, Simon, Abeera, Marina, Amedeo, Andreas, Gerald, Aruna, James and Zhong for recruiting patients, scanning and drawing all those circles! Thank you to Jouke for helping me to decode the code. Thank you to all my volunteers and patients for keeping still and holding their breath. Thank you to John, Lorna, Rebecca, Stephen and Annette for letting me to do 'one last scan'.

I have met people from all over the world, who have really changed me; Isra, Maria Jose, Andrea, Ulrike, Katie, Tanja, Suzanne, Nick, Markus, Devis, Lenka, Rado, Jen, Caroline and many others. I am sorry about the rain, the tube, the not smiling in the lift, the pubs closing at 11pm and all the saying sorry. I have made a note of it, I promise!

It was a leap of faith to give up my job and my home town to come to King's but I don't regret it. Thank you to Grazyna for helping me to become a Londoner and for all her patience and kindness. Thank you to Susi for being so proud of my achievements. Thank you to Mike for being my brother and a great friend.

10. Curriculum Vitae

Personal Information:
Date of birth: 31st March 1980
Nationality: English

Current work:
Since Feb 2009: Research on cardiovascular MRI imaging in the research group of Prof. Rene Botnar, Division of Imaging Sciences and Biomedical Engineering, King's College London.

- Pulse sequence programming
- Experimental work on 1.5 T and 3.0 T whole body scanners
- Evaluation of new methods in clinical applications

Education and Professional Qualifications:

Apr 2008:	HPC Clinical Scientist Registration (MRI Physics) Southampton University Hospitals Trust
Oct 2005:	IPEM Part I Training Diploma Southampton/Portsmouth Consortium (MERIT)
Oct 2004:	MSc Medical Physics University of Surrey (DISTINCTION)
June 2002:	MSci Physics University of Birmingham (2i)
June 1998:	A-Levels: Physics (A) French (A) Pure Mathematics (B)
June 1996:	GCSEs: English Language (A*) Double Science (A*A*) Maths (A*) PE (A*) History (A*) French (A) English Literature (A) Drama (A) Statistics (A)

Previous work:

Oct 05 – Jan 09:	MRI Physicist at Southampton University NHS Trust
Sept 03 – Sept 05:	IPEM Part I Training Southampton University Trust Major attachments in Medical Imaging, Nuclear Medicine & Radiotherapy.
Summers 00 & 01:	Two three-month placements with Defense Science & Technology Laboratory (DSTL)

11. Publications and Presentations

Journal Papers:

Sarah A. Peel, Tarique Hussain, Marina Cecelja, Abeera Abbas, Gerald F. Greil, Philip Chowienczyk, Tim Spector, Alberto Smith, Matthew Waltham, René M. Botnar
'Accelerated aortic imaging using small field-of-view imaging and electrocardiogram-triggered quadruple inversion recovery magnetization preparation'
Journal of magnetic resonance imaging 2011;34(5):1176-83

Sarah A. Peel, Tarique Hussain, Tobias Schaeffter, Gerald F. Greil, Miriam W. Lagemaat and René M. Botnar
Cross-sectional and in-plane coronary vessel wall imaging using a local inversion pre-pulse and spiral read-out: a comparison between 1.5 T and 3.0 T
Journal of magnetic resonance imaging 2012;35(4):969-975

Sarah A. Peel, Geraint Morton, Amedeo Chiribiri, Andreas Schuster, Eike Nagel and René M. Botnar
'A dual inversion recovery MRI sequence for reduced blood signal in late gadolinium enhancement images of myocardial scar'
Radiology (accepted – in press)

Tarique Hussain, Rachel E Clough, Marina Cecelja, Marcus Makowski, **Sarah A Peel**, Philip Chowienczyk, Tobias Schaeffter, Gerald Greil, René Botnar
'Zoom imaging for rapid aortic vessel wall imaging and cardiovascular risk assessment'
Journal of magnetic resonance imaging 2011;34(2):279-85

Conferences:

Sarah A. Peel, Aruna Arujuna, James Harrison, Reza Razavi, Kawal Rhode, Jaswinder Gill, Tobias Schaeffter and René Botnar
Dual inversion recovery pre-pulse improves blood suppression and allows earlier imaging in late gadolinium enhancement images of atrial scar after radiofrequency ablation. ISMRM 2012 Melbourne Poster

Sarah A. Peel, Aruna Arujuna, Reza Razavi, Kawal Rhode, Jaswinder Gill, Tobias Schaeffter and René Botnar
Dual inversion recovery pre-pulse differentiates contrast uptake from edema in late gadolinium enhancement images of atrial scar after radiofrequency ablation. ISMRM 2012 Melbourne Poster

Tarique Hussain, Khalid Hussain, **Sarah A. Peel**, Gerald F Greil, Rene Botnar, Andrea Wiethoff
Coronary magnetic resonance angiography: in vivo comparison of image quality at 1.5 Tesla versus 3.0 Tesla with Parallel Radiofrequency Transmission. SCMR Orlando 2012 Poster. Journal of Cardiovascular Magnetic Resonance. 2012; 14(1):255.

Tarique Hussain, Matthew Fenton, **Sarah A. Peel**, Andrea Wiethoff, Rene M Botnar, Michael Burch, Gerald F Greil
Diagnosis of post-transplant coronary artery disease using contrast enhanced coronary vessel wall imaging at 3.0 Tesla. SCMR Orlando 2012 Poster. Journal of cardiovascular magnetic resonance 2012; 14 Suppl 1:P13

S. A. Peel, T. Hussain, M. Cecelja, A. Abbas, G. Greil, and R. M. Botnar
ECG–triggering improves blood suppression in abdominal aortic imaging using the quadruple inversion recovery sequence. ISMRM 2011 Montreal Poster

S. A. Peel, G. Morton, E. Nagel, and R. M. Botnar
Non-selective double inversion recovery pre-pulse for flow-independent black blood myocardial scar imaging: optimization of the T1 suppression range. ISMRM 2011 Montreal Poster

Sarah A. Peel, Tarique Hussain, Marina Cecelja, Abeera Abbas, Gerald Greil, and René Botnar
Accelerated aortic plaque imaging using small field-of-view imaging and quadruple inversion recovery magnetization preparation. SCMR 2011, Nice. Poster . Journal of Cardiovascular Magnetic Resonance. 2011;13(Suppl 1): P368.

Sarah A. Peel, Tarique Hussain, Michael Burch, Matthew Fenton, Andrew Taylor, Vivek Muthurangu, Gerald Greil and René Botnar. Post-contrast non-selective double inversion recovery imaging of the coronary arteries in patients with coronary allograft vasculopathy. SCMR 2011, Nice. Poster. Journal of Cardiovascular Magnetic Resonance. 2011;13(Suppl 1):P241

Tarique Hussain, **Sarah A. Peel**, Aphrodite Tzifa, Thomas Krasemann, Gerald Greil and Rene Botnar
Coronary vessel wall assessment after Kawasaki Disease. SCMR 2011, Nice. Poster. Journal of Cardiovascular Magnetic Resonance. 2011; 13(Suppl 1): P235.

S. A. Peel, T. Hussain, G. Greil, T. Schaeffter, and R. M. Botnar
Local inversion spiral coronary vessel wall imaging: A comparison between 1.5 T and 3.0 T. ISMRM 2010, Stockholm: Poster

S. A. Peel, C. Jansen, G. Morton, S. Duckett, T. Schaeffter, and R. M. Botnar.
Non-selective double inversion recovery pre-pulse for flow-independent black blood myocardial viability imaging. ISMRM 2010, Stockholm Poster

Sarah A. Peel, Christian Jansen, Nicolas Toussaint, Tobias Schaeffter, René M. Botnar
Non-selective double inversion recovery pre-pulse for flow-independent black blood myocardial viability imaging. SCMR 2010, Pheonix Poster Journal of Cardiovascular Magnetic Resonance;2010 (Supp1), p1

References

1. Lloyd-Jones, D., et al., Heart disease and stroke statistics--2009 update: a report from the American Heart Association Statistics Committee and Stroke Statistics Subcommittee. Circulation, 2009. 119(3): p. 480-6.
2. Glagov, S., et al., Compensatory enlargement of human atherosclerotic coronary arteries. N Engl J Med, 1987. 316(22): p. 1371-5.
3. Little, W.C., et al., Can coronary angiography predict the site of a subsequent myocardial infarction in patients with mild-to-moderate coronary artery disease? Circulation, 1988. 78(5 Pt 1): p. 1157-66.
4. Falk, E., P.K. Shah, and V. Fuster, Coronary plaque disruption. Circulation, 1995. 92(3): p. 657-71.
5. Solberg, L.A. and J.P. Strong, Risk factors and atherosclerotic lesions. A review of autopsy studies. Arteriosclerosis, 1983. 3(3): p. 187-98.
6. Van Zaane, B., et al., Meta-analysis of the diagnostic accuracy of transesophageal echocardiography for assessment of atherosclerosis in the ascending aorta in patients undergoing cardiac surgery. Acta Anaesthesiol Scand, 2008. 52(9): p. 1179-87.
7. Kurra, V., et al., Extent of thoracic aortic atheroma burden and long-term mortality after cardiothoracic surgery: a computed tomography study. JACC Cardiovasc Imaging. 3(10): p. 1020-9.
8. Small, G.R. and T.D. Ruddy, PET imaging of aortic atherosclerosis: Is combined imaging of plaque anatomy and function an amaranthine quest or conceivable reality? J Nucl Cardiol. 18(4): p. 717-28.
9. Cai, J.M., et al., Classification of human carotid atherosclerotic lesions with in vivo multicontrast magnetic resonance imaging. Circulation, 2002. 106(11): p. 1368-73.
10. Fayad, Z.A. and V. Fuster, Clinical imaging of the high-risk or vulnerable atherosclerotic plaque. Circ Res, 2001. 89(4): p. 305-16.
11. Kramer, C.M., et al., Magnetic resonance imaging identifies the fibrous cap in atherosclerotic abdominal aortic aneurysm. Circulation, 2004. 109(8): p. 1016-21.
12. Toussaint, J.F., et al., Magnetic resonance images lipid, fibrous, calcified, hemorrhagic, and thrombotic components of human atherosclerosis in vivo. Circulation, 1996. 94(5): p. 932-8.
13. Yuan, C., et al., Measurement of atherosclerotic carotid plaque size in vivo using high resolution magnetic resonance imaging. Circulation, 1998. 98(24): p. 2666-71.
14. Yuan, C., et al., In vivo accuracy of multispectral magnetic resonance imaging for identifying lipid-rich necrotic cores and intraplaque hemorrhage in advanced human carotid plaques. Circulation, 2001. 104(17): p. 2051-6.
15. Maintz, D., et al., Selective coronary artery plaque visualization and differentiation by contrast-enhanced inversion prepared MRI. Eur Heart J, 2006. 27(14): p. 1732-6.

16. Botnar, R.M., et al., In vivo molecular imaging of acute and subacute thrombosis using a fibrin-binding magnetic resonance imaging contrast agent. Circulation, 2004. 109(16): p. 2023-9.
17. Spuentrup, E., et al., Molecular magnetic resonance imaging of coronary thrombosis and pulmonary emboli with a novel fibrin-targeted contrast agent. Circulation, 2005. 111(11): p. 1377-82.
18. Wagner, A., et al., Contrast-enhanced MRI and routine single photon emission computed tomography (SPECT) perfusion imaging for detection of subendocardial myocardial infarcts: an imaging study. Lancet, 2003. 361(9355): p. 374-9.
19. Kim, R.J., et al., The use of contrast-enhanced magnetic resonance imaging to identify reversible myocardial dysfunction. N Engl J Med, 2000. 343(20): p. 1445-53.
20. Selvanayagam, J.B., et al., Value of delayed-enhancement cardiovascular magnetic resonance imaging in predicting myocardial viability after surgical revascularization. Circulation, 2004. 110(12): p. 1535-41.
21. Kwong, R.Y., et al., Impact of unrecognized myocardial scar detected by cardiac magnetic resonance imaging on event-free survival in patients presenting with signs or symptoms of coronary artery disease. Circulation, 2006. 113(23): p. 2733-43.
22. Huang, S.K., et al., Closed chest catheter desiccation of the atrioventricular junction using radiofrequency energy--a new method of catheter ablation. J Am Coll Cardiol, 1987. 9(2): p. 349-58.
23. Pappone, C., et al., Circumferential radiofrequency ablation of pulmonary vein ostia: A new anatomic approach for curing atrial fibrillation. Circulation, 2000. 102(21): p. 2619-28.
24. Willems, S., et al., Catheter ablation of atrial flutter guided by electroanatomic mapping (CARTO): a randomized comparison to the conventional approach. J Cardiovasc Electrophysiol, 2000. 11(11): p. 1223-30.
25. Peters, D.C., et al., Detection of pulmonary vein and left atrial scar after catheter ablation with three-dimensional navigator-gated delayed enhancement MR imaging: initial experience. Radiology, 2007. 243(3): p. 690-5.
26. McGann, C.J., et al., New magnetic resonance imaging-based method for defining the extent of left atrial wall injury after the ablation of atrial fibrillation. J Am Coll Cardiol, 2008. 52(15): p. 1263-71.
27. Badger, T.J., et al., Evaluation of left atrial lesions after initial and repeat atrial fibrillation ablation: lessons learned from delayed-enhancement MRI in repeat ablation procedures. Circ Arrhythm Electrophysiol. 3(3): p. 249-59.
28. Look, D. and D. Locker, Time saving in measurement of NMR and EPR relaxation times. Review Scientific Instruments 1970R. 41: p. 250–251.
29. Yarnykh, V.L. and C. Yuan, T1-insensitive flow suppression using quadruple inversion-recovery. Magn Reson Med, 2002. 48(5): p. 899-905.
30. Yarnykh, V.L. and C. Yuan, Simultaneous outer volume and blood suppression by quadruple inversion-recovery. Magn Reson Med, 2006. 55(5): p. 1083-92.
31. Feinberg, D.A., et al., Inner volume MR imaging: technical concepts and their application. Radiology, 1985. 156(3): p. 743-7.

32. Simonetti, O.P., et al., An improved MR imaging technique for the visualization of myocardial infarction. Radiology, 2001. 218(1): p. 215-23.
33. Kellman, P., et al., Phase-sensitive inversion recovery for detecting myocardial infarction using gadolinium-delayed hyperenhancement. Magn Reson Med, 2002. 47(2): p. 372-83.
34. Messroghli, D.R., et al., Optimization and validation of a fully-integrated pulse sequence for modified look-locker inversion-recovery (MOLLI) T1 mapping of the heart. J Magn Reson Imaging, 2007. 26(4): p. 1081-6.
35. Kellman, P., et al., Multi-contrast delayed enhancement provides improved contrast between myocardial infarction and blood pool. J Magn Reson Imaging, 2005. 22(5): p. 605-13.
36. Salerno, M. Diffusion-prepared dark blood delayed enhancement imaging for improved detection of subendocardial infarcts. in SCMR. 2009.
37. Farrelly, C., et al., Improved detection of subendocardial hyperenhancement in myocardial infarction using dark blood-pool delayed enhancement MRI. AJR Am J Roentgenol. 196(2): p. 339-48.
38. Moghari, M.H., et al., Pulmonary vein inflow artifact reduction for free-breathing left atrium late gadolinium enhancement. Magn Reson Med. 66(1): p. 180-6.
39. Ross, R., Atherosclerosis--an inflammatory disease. N Engl J Med, 1999. 340(2): p. 115-26.
40. Falk, E., Why do plaques rupture? Circulation, 1992. 86(6 Suppl): p. III30-42.
41. Shinnar, M., et al., The diagnostic accuracy of ex vivo MRI for human atherosclerotic plaque characterization. Arterioscler Thromb Vasc Biol, 1999. 19(11): p. 2756-61.
42. Skinner, M.P., et al., Serial magnetic resonance imaging of experimental atherosclerosis detects lesion fine structure, progression and complications in vivo. Nat Med, 1995. 1(1): p. 69-73.
43. Steinman, D.A. and B.K. Rutt, On the nature and reduction of plaque-mimicking flow artifacts in black blood MRI of the carotid bifurcation. Magn Reson Med, 1998. 39(4): p. 635-41.
44. Felmlee, J.P. and R.L. Ehman, Spatial presaturation: a method for suppressing flow artifacts and improving depiction of vascular anatomy in MR imaging. Radiology, 1987. 164(2): p. 559-64.
45. Edelman, R.R., D. Chien, and D. Kim, Fast selective black blood MR imaging. Radiology, 1991. 181(3): p. 655-60.
46. Simonetti, O.P., et al., "Black blood" T2-weighted inversion-recovery MR imaging of the heart. Radiology, 1996. 199(1): p. 49-57.
47. Sharma, P., et al., Effect of Gd-DTPA-BMA on blood and myocardial T1 at 1.5T and 3T in humans. J Magn Reson Imaging, 2006. 23(3): p. 323-30.
48. Flacke, S.J., S.E. Fischer, and C.H. Lorenz, Measurement of the gadopentetate dimeglumine partition coefficient in human myocardium in vivo: normal distribution and elevation in acute and chronic infarction. Radiology, 2001. 218(3): p. 703-10.
49. Fleckenstein, J.L., et al., Fast short-tau inversion-recovery MR imaging. Radiology, 1991. 179(2): p. 499-504.
50. Mai, V.M., J. Knight-Scott, and S.S. Berr, Improved visualization of the human lung in 1H MRI using multiple inversion recovery for simultaneous

suppression of signal contributions from fat and muscle. Magn Reson Med, 1999. 41(5): p. 866-70.
51. Redpath, T.W. and F.W. Smith, Technical note: use of a double inversion recovery pulse sequence to image selectively grey or white brain matter. Br J Radiol, 1994. 67(804): p. 1258-63.
52. Dixon, W.T., et al., Multiple inversion recovery reduces static tissue signal in angiograms. Magn Reson Med, 1991. 18(2): p. 257-68.
53. Mani, S., et al., Background suppression with multiple inversion recovery nulling: applications to projective angiography. Magn Reson Med, 1997. 37(6): p. 898-905.
54. Koktzoglou, I. and D. Li, Diffusion-prepared segmented steady-state free precession: Application to 3D black-blood cardiovascular magnetic resonance of the thoracic aorta and carotid artery walls. J Cardiovasc Magn Reson, 2007. 9(1): p. 33-42.
55. Wang, J., et al., Improved suppression of plaque-mimicking artifacts in black-blood carotid atherosclerosis imaging using a multislice motion-sensitized driven-equilibrium (MSDE) turbo spin-echo (TSE) sequence. Magn Reson Med, 2007. 58(5): p. 973-81.
56. Makhijani, M.K., et al., Improved blood suppression in three-dimensional (3D) fast spin-echo (FSE) vessel wall imaging using a combination of double inversion-recovery (DIR) and diffusion sensitizing gradient (DSG) preparations. J Magn Reson Imaging. 31(2): p. 398-405.
57. Oyama, N., et al., Differential impact of age, sex, and hypertension on aortic atherosclerosis: the Framingham Heart Study. Arterioscler Thromb Vasc Biol, 2008. 28(1): p. 155-9.
58. Hussain, T., et al., Zoom imaging for rapid aortic vessel wall imaging and cardiovascular risk assessment. J Magn Reson Imaging. 34(2): p. 279-85.
59. O'Donnell, M., NMR blood flow imaging using multiecho, phase contrast sequences. Med Phys, 1985. 12(1): p. 59-64.
60. Moran, P.R., A flow velocity zeugmatographic interlace for NMR imaging in humans. Magn Reson Imaging, 1982. 1(4): p. 197-203.
61. Maier, S.E., et al., Human abdominal aorta: comparative measurements of blood flow with MR imaging and multigated Doppler US. Radiology, 1989. 171(2): p. 487-92.
62. Lotz, J., et al., Cardiovascular flow measurement with phase-contrast MR imaging: basic facts and implementation. Radiographics, 2002. 22(3): p. 651-71.
63. Cheng, C.P., R.J. Herfkens, and C.A. Taylor, Abdominal aortic hemodynamic conditions in healthy subjects aged 50-70 at rest and during lower limb exercise: in vivo quantification using MRI. Atherosclerosis, 2003. 168(2): p. 323-31.
64. Harloff, A., et al., 3D blood flow characteristics in the carotid artery bifurcation assessed by flow-sensitive 4D MRI at 3T. Magn Reson Med, 2009. 61(1): p. 65-74.
65. Bloch, F., Nuclear Induction. Physical Review, 1946. 70(7-8): p. 460-474.
66. Constantinides, C.D., E. Atalar, and E.R. McVeigh, Signal-to-noise measurements in magnitude images from NMR phased arrays. Magn Reson Med, 1997. 38(5): p. 852-7.

67. Etienne, A., et al., "Soap-Bubble" visualization and quantitative analysis of 3D coronary magnetic resonance angiograms. Magn Reson Med, 2002. 48(4): p. 658-66.
68. Gupta, A., et al., Myocardial infarction: optimization of inversion times at delayed contrast-enhanced MR imaging. Radiology, 2004. 233(3): p. 921-6.
69. Penfield, J.G. and R.F. Reilly, Jr., What nephrologists need to know about gadolinium. Nat Clin Pract Nephrol, 2007. 3(12): p. 654-68.
70. Kei, P.L. and L.P. Chan, Gadolinium chelate-associated nephrogenic systemic fibrosis. Singapore Med J, 2008. 49(3): p. 181-5.
71. Caravan, P., Strategies for increasing the sensitivity of gadolinium based MRI contrast agents. Chem Soc Rev, 2006. 35(6): p. 512-23.
72. Pintaske, J., et al., Relaxivity of Gadopentetate Dimeglumine (Magnevist), Gadobutrol (Gadovist), and Gadobenate Dimeglumine (MultiHance) in human blood plasma at 0.2, 1.5, and 3 Tesla. Invest Radiol, 2006. 41(3): p. 213-21.
73. Grobner, T., Gadolinium--a specific trigger for the development of nephrogenic fibrosing dermopathy and nephrogenic systemic fibrosis? Nephrol Dial Transplant, 2006. 21(4): p. 1104-8.
74. ProHance/ProHance Multipack. Advisory Committee Briefing Document Cardiovascular and Renal Drugs Advisory Committee and the Drug Safety and Risk Management Advisory Committee Gadolinium Based Contrast Agents. NDAs 200-131/21-489. Submitted by Bracco October 30, 2009.
75. U.S. Food and Drug Administration Alert: Information for healthcare professionals: Gadolinium-based contrast agents for magnetic resonance imaging, 5/23/2007. Available at: http://www.fda.gov/Drugs/DrugSafety/PostmarketDrugSafetyInformationforPatientsandProviders/ucm142884.htm. Accessed October 30, 2008. .
76. Elmholdt TR, Jorgensen B, Ramsing M, Pedersen M, Olesen AB. Two cases of nephrogenic systemic fibrosis after exposure to the macrocyclic compound gabobutrol. NDT Plus Advance Access. Published online on March 19, 2010. Available at: http://ndtplus.oxfordjournals.org/cgi/content/abstract/sfq028. Accessed April 12, 2010.
77. American College of Radiology. Manual on Contrast Media. Version 6. 2008. Available at: http://www.acr.org/SecondaryMainMenuCategories/quality_safety/contrast_manual.aspx. Accessed October 30, 2008.
78. MRHA Drug Safety Update: Gadolinium-containing contrast agents: new advice to minimise the risk of nephrogenic systemic fibrosis. Volume 3, Issue 6 January 2010

Website: http://www.mhra.gov.uk/home/groups/pl-p/documents/publication/con068298.pdf.

79. Perazella, M.A., How should nephrologists approach gadolinium-based contrast imaging in patients with kidney disease? Clin J Am Soc Nephrol, 2008. 3(3): p. 649-51.
80. Schlosser, T., et al., Myocardial infarct: depiction with contrast-enhanced MR imaging--comparison of gadopentetate and gadobenate. Radiology, 2005. 236(3): p. 1041-6.

81. Bauner, K.U., et al., [Late gadolinium enhancement in the diagnostics of ischemic heart disease: technical principles, contrast optimization and clinical application]. Radiologe. 50(6): p. 523-31.
82. Balci, N.C., et al., Low-dose gadobenate dimeglumine versus standard-dose gadopentate dimeglumine for delayed contrast-enhanced cardiac magnetic resonance imaging. Acad Radiol, 2006. 13(7): p. 833-9.
83. Papini, G.D., et al., Myocardial delayed enhancement using a single dose (0.1 mmol/kg) of gadobenate dimeglumine: contrast resolution versus intraventricular blood and viable myocardium. Radiol Med. 115(5): p. 693-701.
84. C. Sallemi, F.De C., A. Esposito, S. Ravelli, R. Mellone, T. Canu, M. Cava, A. Del Maschio, Intraindividual comparison between single-dose 1M Gadobutrol and double-dose 0.5M Gadolinium-DTPA for the detection of myocardial late enhancement (MLE) in cardiac magnetic resonance (CMR), in European Society of Radiology Annual Meeting. 2011.
85. Kramer, C.M., et al., Standardized cardiovascular magnetic resonance imaging (CMR) protocols, society for cardiovascular magnetic resonance: board of trustees task force on standardized protocols. J Cardiovasc Magn Reson, 2008. 10: p. 35.
86. Klein, C., et al., The influence of myocardial blood flow and volume of distribution on late Gd-DTPA kinetics in ischemic heart failure. J Magn Reson Imaging, 2004. 20(4): p. 588-93.
87. Goldfarb, J.W., S. Arnold, and M. Roth, Gadolinium pharmacokinetics of chronic myocardial infarcts: Implications for late gadolinium-enhanced infarct imaging. J Magn Reson Imaging, 2009. 30(4): p. 763-70.
88. Kim, R.J., et al., Relationship of MRI delayed contrast enhancement to irreversible injury, infarct age, and contractile function. Circulation, 1999. 100(19): p. 1992-2002.
89. Gerber, B.L., et al., Accuracy of contrast-enhanced magnetic resonance imaging in predicting improvement of regional myocardial function in patients after acute myocardial infarction. Circulation, 2002. 106(9): p. 1083-9.
90. Ibrahim, T., et al., Quantitative measurement of infarct size by contrast-enhanced magnetic resonance imaging early after acute myocardial infarction: comparison with single-photon emission tomography using Tc99m-sestamibi. J Am Coll Cardiol, 2005. 45(4): p. 544-52.
91. Simor, T., et al., Percent infarct mapping for delayed contrast enhancement magnetic resonance imaging to quantify myocardial viability by Gd(DTPA). J Magn Reson Imaging. 32(4): p. 859-68.
92. Amado, L.C., et al., Accurate and objective infarct sizing by contrast-enhanced magnetic resonance imaging in a canine myocardial infarction model. J Am Coll Cardiol, 2004. 44(12): p. 2383-9.
93. Flett, A.S., et al., Evaluation of techniques for the quantification of myocardial scar of differing etiology using cardiac magnetic resonance. JACC Cardiovasc Imaging. 4(2): p. 150-6.
94. Hsu, L.Y., et al., Quantitative myocardial infarction on delayed enhancement MRI. Part II: Clinical application of an automated feature analysis and combined thresholding infarct sizing algorithm. J Magn Reson Imaging, 2006. 23(3): p. 309-14.

95. Hsu, L.Y., et al., Quantitative myocardial infarction on delayed enhancement MRI. Part I: Animal validation of an automated feature analysis and combined thresholding infarct sizing algorithm. J Magn Reson Imaging, 2006. 23(3): p. 298-308.
96. Messroghli, D.R., et al., Modified Look-Locker inversion recovery (MOLLI) for high-resolution T1 mapping of the heart. Magn Reson Med, 2004. 52(1): p. 141-6.
97. Kim, R.J., D.J. Shah, and R.M. Judd, How we perform delayed enhancement imaging. J Cardiovasc Magn Reson, 2003. 5(3): p. 505-14.
98. Blume, U., et al., Interleaved T(1) and T(2) relaxation time mapping for cardiac applications. J Magn Reson Imaging, 2009. 29(2): p. 480-7.
99. Nguyen, T.D., et al., Effective motion-sensitizing magnetization preparation for black blood magnetic resonance imaging of the heart. J Magn Reson Imaging, 2008. 28(5): p. 1092-100.
100. Salerno, M. Diffusion-prepared dark blood delayed enhancement imgaing for improved detection of subendocaridal infarcts. in SCMR. 2009.
101. Bogun, F., et al., Post-infarction ventricular arrhythmias originating in papillary muscles. J Am Coll Cardiol, 2008. 51(18): p. 1794-802.
102. Flynn, M., et al., Regional wall motion abnormalities and scarring in severe functional ischemic mitral regurgitation: A pilot cardiovascular magnetic resonance imaging study. J Thorac Cardiovasc Surg, 2009. 137(5): p. 1063-70 e2.
103. Lardo, A.C., et al., Visualization and temporal/spatial characterization of cardiac radiofrequency ablation lesions using magnetic resonance imaging. Circulation, 2000. 102(6): p. 698-705.
104. Dickfeld, T., et al., Characterization of radiofrequency ablation lesions with gadolinium-enhanced cardiovascular magnetic resonance imaging. J Am Coll Cardiol, 2006. 47(2): p. 370-8.
105. Sievers, B., et al., Cardiovascular magnetic resonance of iatrogenic ventricular scarring due to catheter ablation for left ventricular tachycardia. Int J Cardiol, 2003. 91(2-3): p. 249-50.
106. Saranathan, M., C.E. Rochitte, and T.K. Foo, Fast, three-dimensional free-breathing MR imaging of myocardial infarction: a feasibility study. Magn Reson Med, 2004. 51(5): p. 1055-60.
107. Stuber, M., et al., Contrast agent-enhanced, free-breathing, three-dimensional coronary magnetic resonance angiography. J Magn Reson Imaging, 1999. 10(5): p. 790-9.
108. Ehman, R.L. and J.P. Felmlee, Adaptive technique for high-definition MR imaging of moving structures. Radiology, 1989. 173(1): p. 255-63.
109. Spuentrup, E., et al., Navigator-gated and real-time motion corrected free-breathing MR Imaging of myocardial late enhancement. Rofo, 2002. 174(5): p. 562-7.
110. Peters, D., et al., Respiratory bellows-gated left atrial late godolinium enhancement. Journal of Cardiovascular Magnetic Resonance, 2011. 13(Supp 1): p. P262.
111. Oakes, R.S., et al., Detection and quantification of left atrial structural remodeling with delayed-enhancement magnetic resonance imaging in patients with atrial fibrillation. Circulation, 2009. 119(13): p. 1758-67.

112. Vergara, G.R. and N.F. Marrouche, Tailored management of atrial fibrillation using a LGE-MRI based model: from the clinic to the electrophysiology laboratory. J Cardiovasc Electrophysiol. 22(4): p. 481-7.
113. Yokokawa, M., et al., The change in the tissue characterization detected by magnetic resonance imaging after radiofrequency ablation of isthmus-dependent atrial flutter. Int J Cardiol. 148(1): p. 30-5.
114. Peters, D.C., et al., Recurrence of atrial fibrillation correlates with the extent of post-procedural late gadolinium enhancement: a pilot study. JACC Cardiovasc Imaging, 2009. 2(3): p. 308-16.
115. Taclas, J.E., et al., Relationship between intended sites of RF ablation and post-procedural scar in AF patients, using late gadolinium enhancement cardiovascular magnetic resonance. Heart Rhythm. 7(4): p. 489-96.
116. Wylie, J.V., Jr., et al., Left atrial function and scar after catheter ablation of atrial fibrillation. Heart Rhythm, 2008. 5(5): p. 656-62.
117. Reddy, V.Y., et al., Arrhythmia recurrence after atrial fibrillation ablation: can magnetic resonance imaging identify gaps in atrial ablation lines? J Cardiovasc Electrophysiol, 2008. 19(4): p. 434-7.
118. Yushkevich, P.A., et al., User-guided 3D active contour segmentation of anatomical structures: significantly improved efficiency and reliability. Neuroimage, 2006. 31(3): p. 1116-28.
119. Wright, M., et al., State of the art: catheter ablation of atrial fibrillation. J Cardiovasc Electrophysiol, 2008. 19(6): p. 583-92.
120. Weerasooriya, R., et al., Catheter ablation for atrial fibrillation: are results maintained at 5 years of follow-up? J Am Coll Cardiol. 57(2): p. 160-6.